Doctoral Dissertation

Easily Disassemblable Joining of Dissimilar Materials of SPCC and CFRP Based on Metal Surface Structuring Technology

Tai WANG

July 2024

Graduate School of Engineering
Osaka University

Supervisor

Professor Hiroshi Nishikawa, Ph.D.
Joining and Welding Research Institute
Osaka University

Doctoral Committee

Professor Hiroshi Nishikawa, Ph.D.
Joining and Welding Research Institute
Osaka University

Professor Katsuyoshi Kondoh, Ph.D.
Joining and Welding Research Institute
Osaka University

Professor Kiyokazu Yasuda, Ph.D.
Division of Materials and Manufacturing Science
Osaka University

Contents

Chapter 1: Introduction

1.1 Research Background

1.1.1 Automobile Lightweight Requirement

With the growing societal emphasis on sustainable development and environmental responsibility, all over the world are increasingly confronted with challenges and pressures related to energy conservation and emissions reduction [1, 2]. Currently, 198 countries globally have established dual-carbon targets, peak carbon emissions, and carbon neutrality timelines tailored to their respective national conditions [3]. Major developed nations such as the United States, the European Union, and Japan have already achieved peak carbon emissions and plan to attain carbon neutrality by 2050 [4-6]. Some developing economies, such as China, have set the goal of reaching peak carbon emissions by 2030 and achieving ultimate carbon neutrality by 2060, as illustrated in Fig. 1-1 [7]. It is evident that to realize the ultimate dual-carbon objectives, all nations have to continue to exercise control over carbon emissions.

Industry enterprises are required to actively adopt innovative technologies and processes aimed at reducing energy consumption and mitigating carbon dioxide emissions to achieve more environmentally friendly and sustainable production methods [8, 9]. For automobile enterprises, vehicle lightweight has grown into a significant trend all over the world, which is considered an effective measure to reduce energy consumption and mitigate carbon dioxide emissions [10-12]. The lightweight of automobiles entails, under the precondition of ensuring the strength and safety performance of vehicles, systematically minimizing the curb weight of automobiles to enhance their dynamic capabilities, diminish fuel consumption, and mitigate exhaust emissions [8, 13].

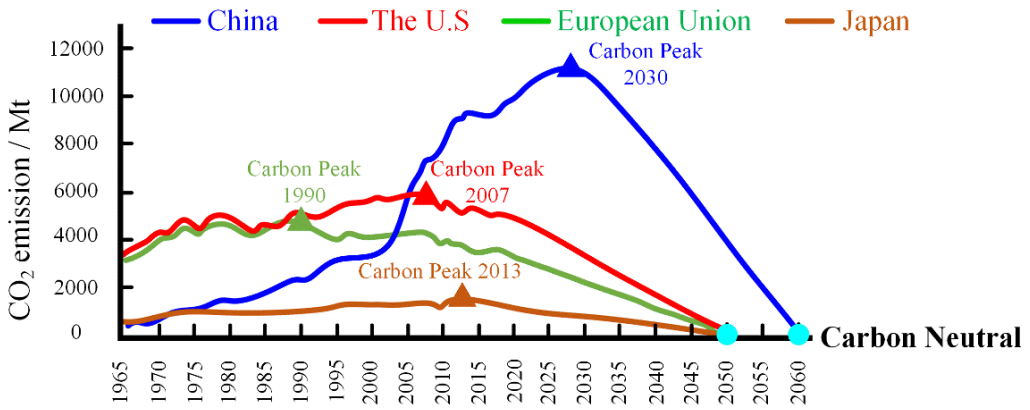

Fig. 1-1 The carbon peak and carbon neutral trajectories of major economies [1].

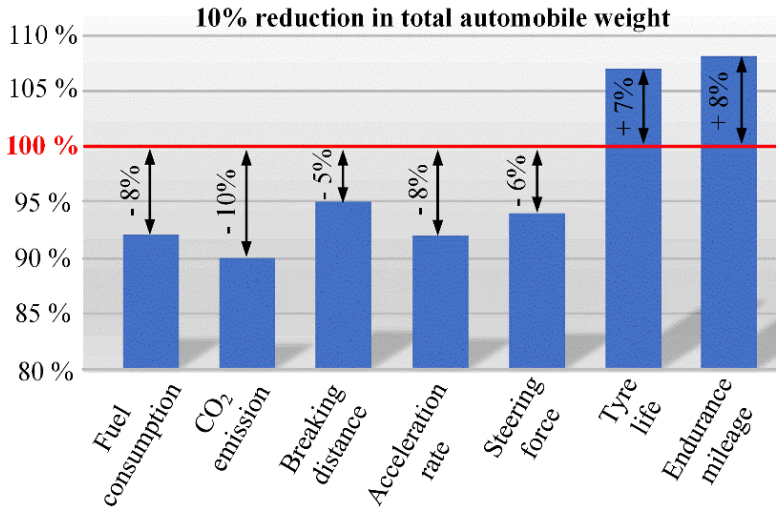

Fig.1-2 Benefits taken from vehicle's lightweight.

Data from organizations such as the U.S. Department of Energy show that for every 10% reduction in overall vehicle weight, fuel consumption can be reduced by 6% to 8%, and carbon emissions can be lowered by 5% to 6% [14]. Other benefits taken from vehicle lightweight can be seen in Fig. 1-2 [15]. Governments worldwide have recognized the importance of vehicle lightweight and have implemented policies and standards to promote its adoption. For example, the European Union has set CO_2 emission performance standards, while the United States has established Corporate Average Fuel Economy (CAFE) standards [16-18]. Similarly, countries like China, Japan, India, and Canada have introduced fuel efficiency regulations and weight reduction targets [19, 20].

The above highlights the effectiveness of lightweight vehicles in reducing fuel consumption and protecting the environment. However, vehicle lightweight is a complex process that requires careful consideration of multiple factors, including performance, cost, safety, and regulatory compliance [21]. As the industry continues to evolve, ongoing research and innovation in lightweight materials and related technologies will play a vital role in shaping the future of automotive manufacturing and sustainable mobility.

1.1.2 Recycling Requirement of Scrap Vehicles

Meanwhile, the escalating accumulation of scrap automobiles has posed a grave threat to the environment, resources, and human health [22-24]. Chemical substances present in abandoned vehicles may infiltrate soil and water sources, resulting in ecosystem degradation [25]. Furthermore, the energy consumption and waste emissions generated during the production and

scrapping of automobiles exacerbate the depletion of natural resources, exerting irreversible pressure on the environment [25, 26]. Simultaneously, the accumulation of scrap vehicles occupies vast amounts of precious land resources, further impacting the ecological balance. A more significant concern is the presence of toxic substances in discarded automobiles, such as heavy metals and chemical pollutants, which may permeate soil and water sources, posing a long-term threat to human health [26].

Elevating the recycling rate of scrap automobiles can yield a series of advantages. Firstly, by enhancing recycling systems, it is possible to efficiently recover renewable resources such as metals, plastics, and rubber from automobiles, reducing overreliance on natural resources and promoting the development of a circular economy. Secondly, the recycling of scrapped vehicles can mitigate pollution to land and water sources, aiding in the reduction of energy consumption during automobile production and disposal, maintaining ecological balance, and achieving environmental conservation goals [27]. In addition, establishing a robust recycling system will create numerous employment opportunities involving workers in recycling, technical personnel, and management staff across various fields, injecting new impetus into economic development [26]. Lastly, to effectively recover various materials from scrap vehicles, continuous improvement and development of relevant technologies and processes are necessary, driving technological innovation and progress [28]. The defects and benefits of scrap vehicles and recycling can be summarized in Fig. 1-3.

Many countries have implemented policies to manage scrap vehicles better to tackle these issues, encompassing proper disposal, recycling requirements, and establishing ambitious reuse and recycling targets [29]. Some nations have also introduced financial incentives to promote responsible scrap vehicle management [30]. In Europe, directives mandate the segregation of vehicle components for reuse and recycling, setting challenging targets at 95% and 85%, respectively [31]. Effectively managing the disassembly process requires collaborative efforts from government, industry, and consumers. For automobile manufacturers, adopting a disassembly-friendly design philosophy, including new recycling methods and alternative materials, can enhance recyclability, contributing to a more sustainable automotive industry. By implementing impactful policies and fostering ongoing innovation, the environmental impact of scrap vehicles can be minimized, facilitating a more sustainable approach to vehicle production and disposal.

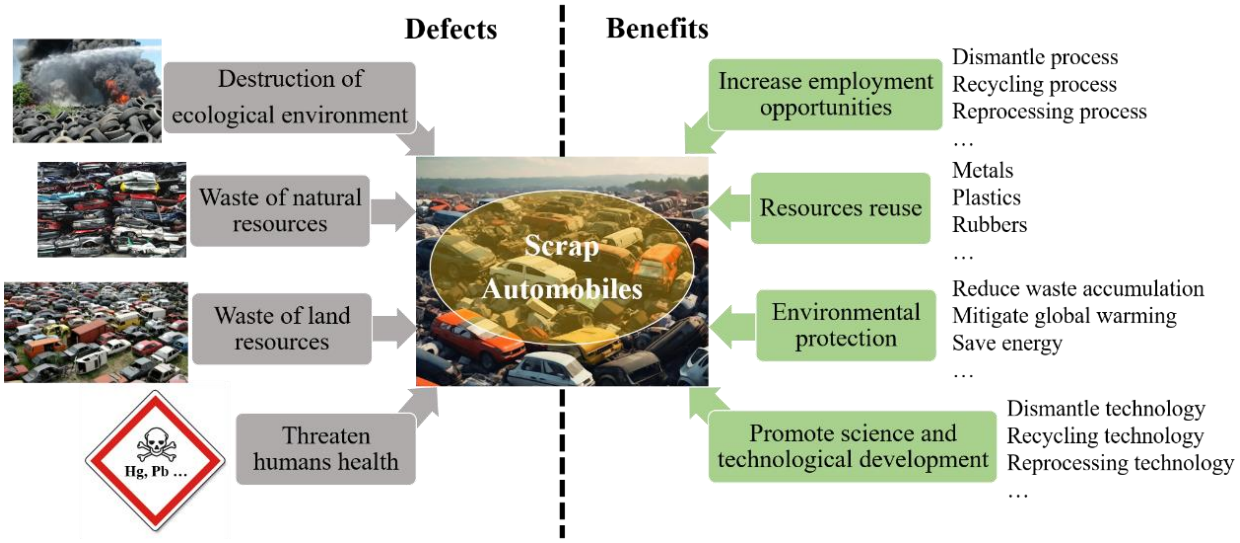

Fig. 1-3 Potential hazards of scrap vehicles and benefits of recycling.

1.2 Strategies for Vehicles Lightweight - Carbon Fiber Reinforced Plastic (CFRP)

Vehicle lightweight, a pivotal strategy in advancing automotive technology, involves the implementation of sophisticated design schemes and innovative materials [32, 33]. This strategy aims to significantly reduce the overall weight of vehicles, thereby playing a crucial role in enhancing their performance, mitigating fuel consumption, and lowering emissions [34]. The critical methodologies employed in achieving lightweight encompass material optimization, structural optimization, and manufacturing process optimization, as illustrated in Fig. 1-4 [35, 36]. These approaches collectively contribute to developing more fuel-efficient and environmentally friendly vehicles, aligning with the ongoing efforts to address sustainability challenges in the automotive industry.

Material optimization constitutes the core of lightweight. Utilizing lightweight, high-strength materials is a significant strategy. New materials such as non-ferrous alloys, aluminum alloys, magnesium alloys, and titanium alloys find extensive applications in automotive manufacturing [37]. These materials, compared to traditional steel, exhibit higher specific strength, allowing for the reduction of vehicle mass while maintaining sufficient strength and safety [38]. Additionally, novel composite materials like aluminum-based composites also play a significant role in providing lightweight solutions [39]. Structural optimization is another critical aspect of achieving automobile lightweight. Advanced structural design and engineering technologies make it possible to reduce curb weight without compromising vehicle strength and safety [40].

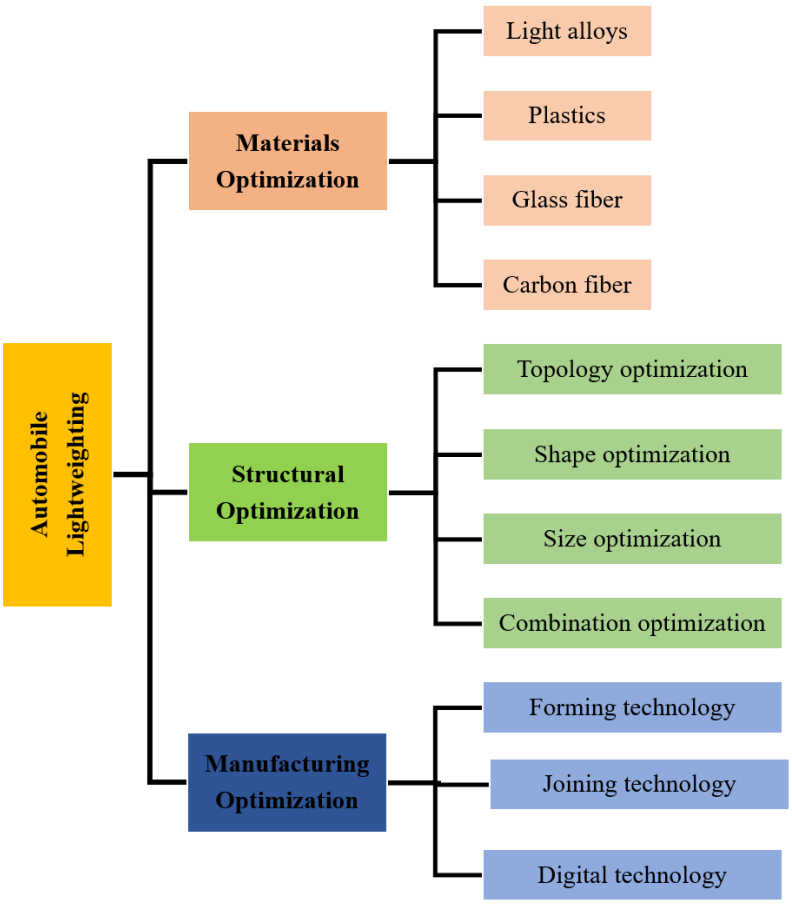

Fig. 1-4 Strategies for vehicles' lightweight. [33]

Methods such as load-bearing body structures and localized reinforcement designs effectively enhance the strength of the overall vehicle structure, reducing material consumption [41]. Furthermore, modular design and advanced computer-aided design technologies contribute to achieving optimal structural configurations [42, 43]. Lastly, the optimization of manufacturing processes is crucial for lightweight. The adoption of advanced manufacturing processes, such as powder metallurgy, laser cutting, and modular assembly, enhances component manufacturing precision, reduces material waste, and lowers overall manufacturing costs [44]. Additionally, new manufacturing technologies contribute to the precise processing of complex structures, thereby improving the performance and durability of automotive components [45].

Among the above strategies of automotive lightweight, material optimization is paramount. To meet environmental and energy efficiency requirements, the selection and application of lightweight, high-strength materials become critical [46]. By continuously optimizing material choices, the automotive manufacturing sector enhances fuel efficiency, meets environmental requirements, and achieves sustainable development goals [47]. Carbon fiber reinforced plastic

(CFRP), a high-strength, high-modulus fiber material with a carbon content exceeding 95%, possesses characteristics such as resistance to creep, high-temperature resistance, and a low coefficient of thermal expansion, which is considered a promising material for lightweight vehicles [37, 48]. Fig. 1-5 illustrates a performance comparison between CFRP and other lightweight materials in the automotive sector [49-51]. Its unique properties in density, specific strength, and tensile strength establish it as a superior candidate among lightweight materials. By adopting lightweight and high-strength CFRP, vehicles' total weight can be significantly reduced, consequently improving fuel efficiency and reducing carbon emissions.

In addition to the promising properties and advantages of CFRP, it offers numerous benefits in automotive applications [52, 53]. Follows conclude CFRP advantages on vehicle manufacturing:

a) Design flexibility

CFRP enables high design freedom, allowing for complex and customized shapes in automotive components. Its modular integration capability facilitates the integration of multiple functions into a single part, reducing assembly complexity and enhancing overall vehicle design.

b) Durability

CFRP exhibits exceptional durability due to its stability of carbon fibers and excellent weathering and aging resistance. Its lifespan is typically 2-3 times longer than that of steel. Components made from CFRP also demonstrate higher fatigue strength than steel, ensuring long-term performance and reliability.

c) Safety enhancements

CFRP’s high strength, typically exceeding 3500 MPa, offers enhanced crashworthiness and occupant protection. CFRP components minimize deformation during collisions, preserving the survival space for occupants. Specially designed CFRP structures can absorb a significant amount of impact energy, surpassing the energy absorption capacity of conventional steel, thus improving vehicle passive safety.

d) Aesthetic appeal

The unique surface of carbon fiber, often coated with a clear varnish, exhibits a dense and orderly arrangement of carbon fiber bundles. Applying CFRP in visible components such as the rear wing, front splitter, instrument panels, door panels, and steering wheels enhances the visual appeal of vehicles, creating a sporty and technologically advanced look.

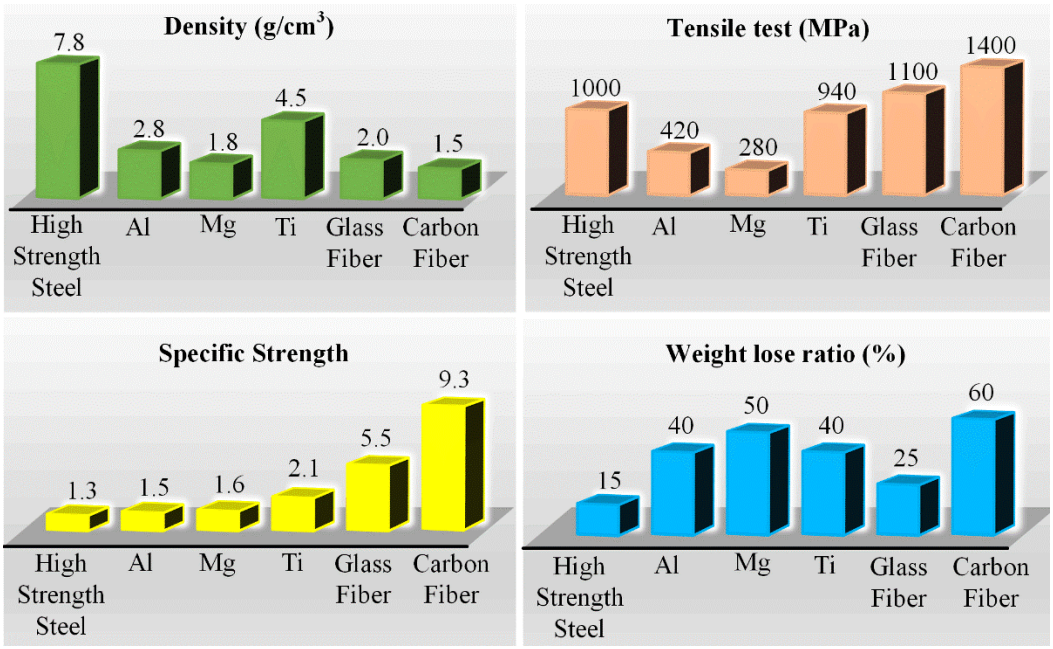

Fig. 1-5 Comparison of light materials' properties.

Electric vehicles have provided a breakthrough for the application of CFRP, offering expansive prospects for its future development in the automotive industry [54]. The application of CFRP in automotive manufacturing is a field with tremendous research and development potential. It is poised to revolutionize the industry by providing lightweight, durable, and cost-effective material [52, 55]. Below are some examples of CFRP applications in automotive manufacturing, which can be summarized through Fig. 1-6, emphasizing the advantages of CFRP and the areas in which it can be utilized in vehicles. Nevertheless, due to its higher cost, the application of CFRP in vehicle manufacturing remains relatively new and limited, primarily restricted to high-performance and luxury vehicle models [56]. However, with technological advancements and the reduction of production costs, CFRP is expected to find broader applications in mainstream vehicle production [57].

In conclusion, among numerous options, adopting CFRP is a promising approach to achieve automotive lightweight and enhance overall fuel efficiency. In this paper, CFRP is chosen as one of the research subjects, aiming to reduce automobile light and explore new joining technologies. Successful integration of metal and CFRP holds immense potential to enhance structural performance, achieve weight reduction, and establish multifunctional material systems [58]. This hybrid structure can combine the strength and rigidity of metals with the high specific strength and rigidity of CFRP, thereby attaining superior mechanical performance and improving overall functionality [59].

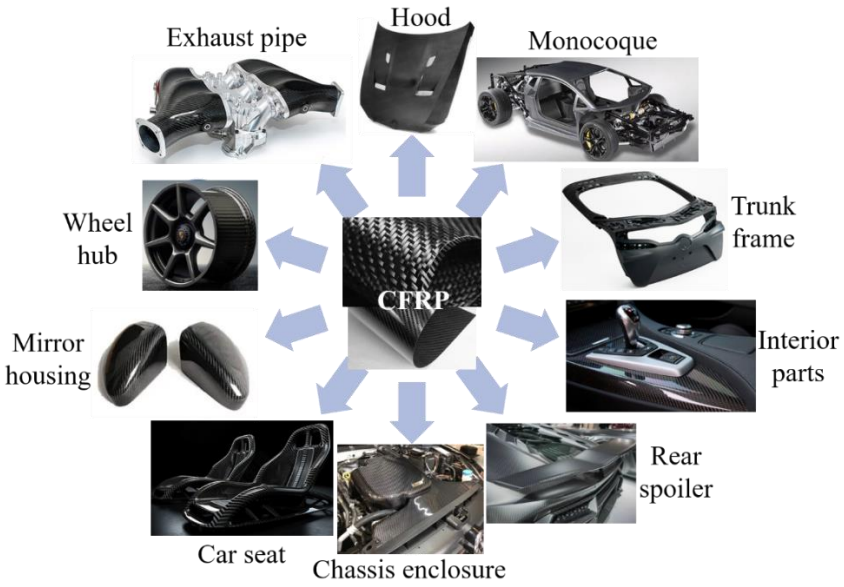

Fig. 1-6 Auto parts made by CFRP.

1.3 Strategy for Scrap Vehicles Recycling – Easy Disassembly Joining

End-of-life vehicles pose significant challenges in recycling due to material complexity, contamination, and advanced welding and adhesive technologies applied among different components joining [60, 61]. This intricate mix complicates disassembly, leading to substantial waste [62, 63]. Recognizing this, the design concept for disassembly for components joining has emerged as a critical discipline in product design for the twenty-first century [64]. Design for disassembly involves considering disassembly and recyclability at the initial design stage to promote efficient product recovery [65]. By streamlining the disassembling and recycling process, the design for disassembly contributes to a circular economy and addresses challenges related to material complexity, contamination, damage, cost, and infrastructure. Improving end-of-life vehicle recycling vehicles should be designed with easy disassembly, ensuring automotive components can be easily separated during disassembly, reducing overall difficulty.

In this study, the investigated joining technology ensures the integrity of dissimilar materials and significantly enhances the disassembly and recycling efficiency at the end-of-life vehicle cycle. This research contributes to improving the efficiency of end-of-life vehicle recycling, reducing waste generation, and promoting sustainable development within the automotive industry. Furthermore, the easily disassembled joining technique increases the value of automotive components for secondary use, fostering a shift towards more sustainable production models that align with environmental protection and sustainable development principles. Through these

advancements, this study provides innovative dissimilar materials joining solutions for the automotive industry, contributing to a more environmentally friendly and sustainable society.

1.4 Review of CFRP-Metals Joining Technologies

Due to substantial differences in the physical and chemical properties at the interface between metal materials and CFRP, such as stiffness, melting point, and thermal expansion coefficient, joining CFRP with metal remains a significant challenge [66, 67]. To fully exploit the advantages of CFRP-metal hybrid structures, it is crucial to select appropriate joining methods to achieve the desired outcomes. This section comprehensively summarizes existing research on joining metals and CFRP, considering joining methods, joining mechanisms, and joint performance. It also analyzes their advantages, disadvantages, and application scenarios. It is important to note that no single joining technology is universally applicable to all situations, as each possesses specific advantages and disadvantages suitable for application.

1.4.1 Mechanical Fastening

Mechanical fastening, as a standard joining method, is crucial in applying metals and carbon fiber composite materials [68, 69]. The schematic diagram of this joining method is illustrated in Fig. 1-7. However, they are confronted with a series of issues [70]. Firstly, traditional mechanical fastening methods, such as rivets and bolts, increase manufacturing complexity, leading to prolonged joining times and stress concentration in the drilling areas [71]. Additionally, hole machines for fastener accommodation induce micro and macro damage to composite materials, inevitably reducing overall structural strength [72]. Despite the various drawbacks of mechanical fastening, they remain irreplaceable in specific fields, particularly in aerospace [73, 74]. Mechanical fastening methods offer advantages such as ease of inspection, maintenance, and recycling, making them the only viable choice for high-load composite material components [71]. However, research focused on reducing the number of fasteners for weight-sensitive structures like aircraft becomes a crucial task [75].

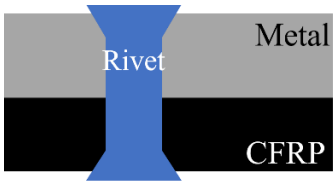

Fig. 1-7 Schematic diagram of mechanical fastening of metal-CFRP.

In the realm of multi-material design, especially the combination of fiber-reinforced plastics and metals, there is a need to identify joining technologies that do not interrupt force transmission, thus harnessing the full advantages of these composite materials. Future research trends should aim to address the shortcomings of traditional mechanical fastening and explore optimized joining technologies to enhance overall structural performance. Overall, mechanical fastening between metals and CFRP remains a continually evolving area, requiring ongoing research and innovation to address existing challenges and propel further advancements in its application [76].

1.4.2 Adhesive Bonding

Adhesive bonding is a commonly employed joining technology, particularly prevalent in metal and CFRP structures, as shown in Fig. 1-8. [77, 78]. However, in comparison to mechanical fastening, it is not without drawbacks. One of these is its low durability, necessitating additional adhesives, stringent surface pre-treatment processes, and extended curing times [79-81]. Furthermore, adhesive bonding may result in detrimental environmental emissions, posing potential risks to human health [82, 83]. At elevated working temperatures, bond quality is susceptible to temperature influences, imposing limitations on the operational temperature range of components [84]. Stringent surface treatment and bonding processes demand specialized heating or pressure treatment equipment [85]. Meanwhile, adhesive bonding offers numerous advantages, including weight reduction, smooth appearance, improved fatigue strength, adaptability, suitability for thin-walled components, simplicity of bonding processes, and potential decrease in production cycles [86, 87]. These advantages position adhesive bonding as a widely adopted joining technology in the automotive manufacturing sector. However, despite the array of benefits that adhesive bonding brings to automotive manufacturing, one unoverlooked challenge persists: maintenance and recycling [88, 89].

In summary, while adhesive bonding has introduced numerous advantages to automotive manufacturing, maintenance, repair, and recycling challenges restrict its scope of application. Therefore, future research should focus on enhancing the maintainability, reparability, and recyclability of adhesive bonding to propel its further utilization in automotive manufacturing.

Fig. 1-8 Schematic diagram of adhesive bonding of metal-CFRP.

1.4.3 Welding (Fusion Bonding)

In the realm of joining metal and carbon fiber composite materials, laser welding is a widely researched method, as explained in Fig. 1-9 [90, 91]. However, laser welding faces multifaceted challenges in practical applications, including material disparities, thermal effects, interface issues, process control difficulties, as well as environmental and equipment cost [92, 93]. Research indicates that when selecting laser welding as a method for joining metal and carbon fiber composite materials, careful consideration of the issues must be undertaken, and necessary process optimizations and control measures must be implemented [94, 95].

Relative to traditional welding methods such as induction welding/fusion and resistance welding/fusion, they present unique advantages and challenges when joining metal and carbon fiber composite materials [96]. Researchers like Mitschang have studied induction welding of metal-composite hybrid joints and found that adding a polymer film intermediate layer can increase shear strength by approximately 15% [97]. Moreover, due to the significant difference in melting points between metal and carbon fiber composite materials, conventional welding methods cannot generate mixed metal-plastic compounds [98]. The temperature differential in melting points leads to thermal degradation of the plastic before the metal component melts. This demands adopting other welding technologies, with induction welding/fusion and resistance welding/fusion becoming primary choices [99]. However, these methods have certain limitations, such as difficulty in disassembly, dependence on conductive filler materials, and restrictions on the use of metal mesh or carbon fiber content [100].

In summary, different welding methods exhibit their respective advantages and limitations in joining metal and carbon fiber composite materials [101]. Laser welding excels in enhancing shear strength, while other methods have unique advantages in terms of ease of monitoring, short processing time, and so forth [102]. Future research directions may include further optimizing existing methods, developing new joining technologies, and addressing environmental and cost issues during welding to promote the broader application of metal and carbon fiber composite materials.

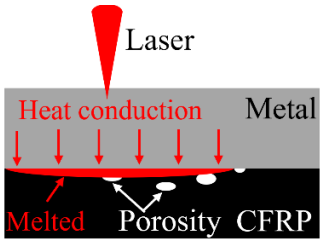

Fig. 1-9 Schematic diagram of laser welding of metal-CFRP.

1.4.4 Ultrasonic Welding

Ultrasonic welding has emerged as a promising method for joining metals and CFRP, garnering significant attention in current research, as shown in Fig. 1-10 [58]. This technique is primarily used in the assembly of thermoplastic automotive composite components, offering notable advantages such as superior mechanical performance, durable joints, short processing times, easy online monitoring, and reduced component surface treatment requirements [103, 104]. One of the key advantages of ultrasonic welding lies in its non-thermal nature, making it particularly suitable for joining temperature-sensitive polymer materials. [105]. By utilizing frictional heat generated through ultrasonic vibration, this method avoids the detrimental effects of high temperatures on carbon fibers, thereby preserving their strength and performance post-joining [106, 107]. Despite these benefits, ultrasonic welding does present limitations [108]. Firstly, it often necessitates the addition of conductive fillers at the joint to facilitate the welding process, which may impact the overall structure [59]. Secondly, the feasibility of ultrasonic welding can be limited by the carbon fiber content, with excessively high levels potentially leading to suboptimal welding effects [109].

Meanwhile, Ultrasonic Plastic Welding (UPW) stands as a standard technology for joining thermoplastic materials [58, 103, 110]. The mechanical oscillation of UPW, perpendicular to the workpieces, promotes the flow and spreading of molten thermoplastics [104]. The mechanical oscillation of UPW, perpendicular to the workpieces, promotes the flow and spreading of molten thermoplastics. UPW offers several significant advantages compared to other joining methods, including fast, flexible, and effective joining processes, minimal surface damage, high structural reliability, low contamination risk, and environmental friendliness [105-107]. Moreover, it presents cost-saving opportunities and greater feasibility for industrial applications [108].

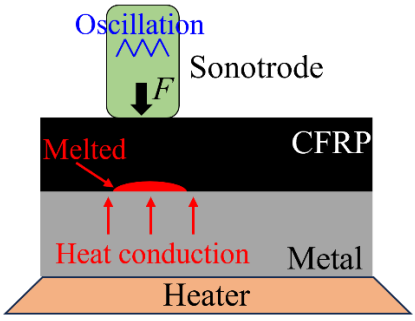

Fig. 1-10 Schematic diagram of ultrasonic welding of metal-CFRP.

In conclusion, while ultrasonic welding demonstrates considerable promise for joining metals and carbon fibers in thermoplastic automotive composite materials, its practical application requires careful consideration of limitations, particularly concerning high carbon fiber content [111, 112]. Future research efforts should optimize ultrasonic welding processes to expand their applicability and facilitate widespread adoption across various fields [113, 114]. Future research endeavors should optimize ultrasonic welding processes to broaden their applicability and achieve widespread utilization in various fields.

1.4.5 Friction Stir and Spot Welding

In the domain of metal and carbon fiber materials joining, friction stir welding and friction spot welding methods have attracted widespread research interest [115]. These two advanced joining techniques offer new avenues to overcome the limitations of traditional joining methods [116]. Nakata et al.'s study focuses on the friction stir welding method, aiming to achieve the connection between CFRP and metal materials by adding interlayer [117]. They note that functional interfacial forces are generated between metal and thermoplastic at the interface. Esteves et al. [118] employed the friction spot welding method with an additional interlayer, investigating the feasibility of joining aluminum-carbon fiber composite materials and optimizing the joining process. The results of these studies demonstrate the feasibility of a viable joining between metal and CFRP by adding an intermediate layer. Furthermore, using thermoplastic films eliminates the curing time associated with adhesives currently used in the industry. These achievements expand the scope of joining technology and offer viable solutions for the composite applications of metal and carbon fiber in various fields.

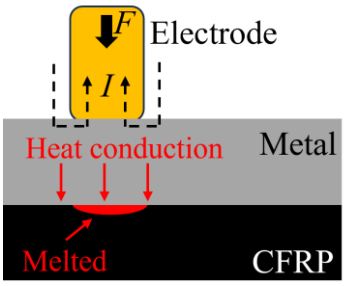

Fig. 1-11 Schematic diagram of spot welding of metal-CFRP.

However, it is worth noting that, despite achieving some success, these studies still face challenges. For example, issues such as material thermodynamics, compatibility during joining, and post-joining structural strength and stability require further in-depth research. Future research directions may include enhancing the efficiency and performance of joining through more advanced intermediate layer materials and joining processes. In conclusion, research on friction stir welding and friction spot welding methods in metal, as well as CFRP joining, is still in a continuous development stage, ushering in broader research prospects.

1.4.6 Based on Metal Surface Texturing Technologies

Structured metal surface joining is a technique focused on improving the strength of connections by introducing minute structures on metal surfaces. The processes are illustrated in Fig. 1-12. These structures create additional interlocking areas, enlarging the effective contact area and enhancing joining strength and shear resistance. The structured metal surface also helps disperse stress, reduce local stress concentrations, and improve overall joining area durability. This method is extensively used for connecting metals with other materials like carbon fiber composites and rubber, especially in applications requiring high strength, durability, shear resistance, or adaptation to thermal expansion differences.

This method incorporates artificial protruding structures onto the metal surface during manufacturing, mechanically interlocking with polymer materials through external force to achieve robust mechanical strength between components. The key lies in controlling the form and arrangement pattern of these protrusions. Different manufacturing methods categorize these structures, including Capacitor Discharge Screw Welding (CDSW), Cold Metal Transfer (CMT), Additive Manufacturing (AM), and laser processing. However, these technologies often produce large-sized protrusions, potentially leading to increased thermal stress on the metal substrate and damage to carbon fiber during connection, mainly when the polymer is thin.

Recent advances in additive manufacturing technologies, such as laser processing and capacitor discharge screw welding, have successfully produced microstructure connections. For instance, studies used additive manufacturing to create microstructures on aluminum alloy surfaces for joining with polymers, demonstrating significant enhancement in strength and interface effects. Laser processing was also employed to create microstructures on A5052 aluminum alloy surfaces, aiding in the impregnation and interlocking of carbon fiber-reinforced plastic. These technologies showcase notable improvements in microstructure connections' strength and interface effects.

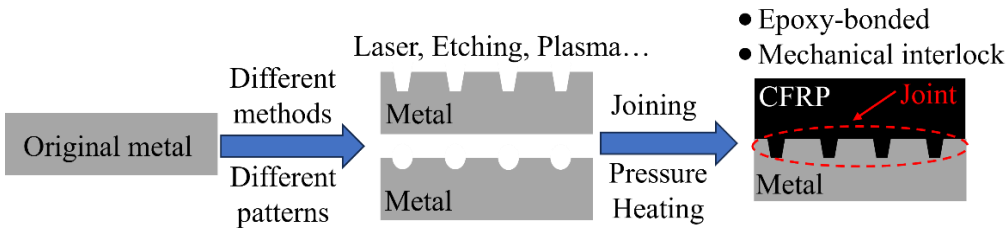

Fig. 1-12 Schematic diagram of metal surface structuring processes.

Recent research highlights the substantial impact of structured metal surface joining on enhancing connection strength. This involves creating complex surface patterns or introducing irregular microstructures on metal surfaces before joining composite materials, increasing roughness and contact area to improve strength and mechanical performance. This method reduces reliance on adhesives, optimizes load distribution, and lowers the risk of thermal damage. In conclusion, structured metal surface joining offers an innovative and advantageous approach for robust and reliable joining in various engineering applications. However, it is essential to note that while these surface patterns enhance joining strength, they may pose challenges during disassembly or dismantling processes.

1.5 Research Purposes and Outlines

1.5.1 Research Purposes – CFRP to Metals Easily Disassemblable Joining Technique

The contemporary automotive industry increasingly anticipates the adoption of CFRP to reduce vehicle weight [92]. To meet the comprehensive performance requirements in automotive design, these composite materials are joined with heterogeneous materials like steel and light alloys [119, 120]. Therefore, the first challenge arises from material differences and disparate coefficients of thermal expansion between composite materials and metals in the joining processes [90, 94]. Simultaneously, considerations for disassembly and recycling at the end-of-life stage of automobiles must be integrated into the initial design phase [121]. This paper aims to investigate the easily disassemblable joining processes between metals and CFRP to achieve high-strength joints and contribute to the disassembly and recycling of decommissioned vehicles. The purposes can be illustrated in Fig. 1-13.

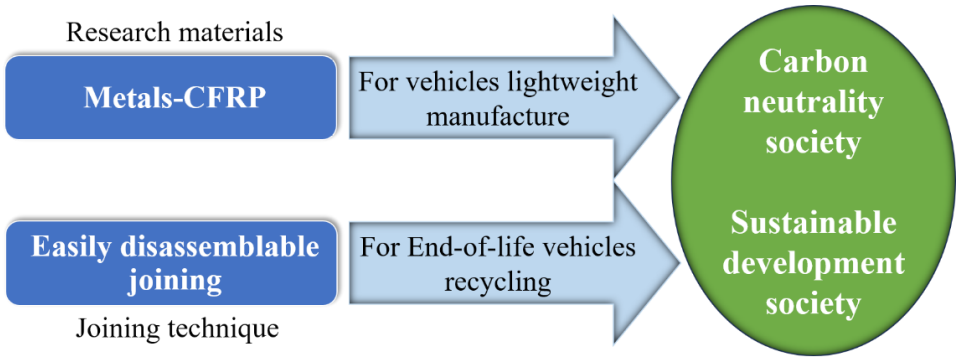

Fig. 1-13 Research purposes and significances of this paper.

1.5.2 Research Outlines

This article primarily addresses two aspects of manufacturing lightweight automobiles: joining dissimilar materials and disassembling components post-end-of-life. A composite structure involving metals and CFRP has been employed for the former. Regarding the latter, traditional joining methods have historically prioritized high mechanical strength in dissimilar materials but have often overlooked the disassembly and recycling processes at the end of a product's lifecycle. Given the shortcomings of this traditional approach and the characteristics of CFRP, an innovative approach is proposed. This approach involves manufacturing protruding structures on metal surfaces for the joining of metal and CFRP. This method is considered a sustainable approach, as it facilitates both strong joining and promotes ease of disassembly processes, addressing the limitations associated with the traditional method and harnessing the properties of CFRP.

Chapter 1 introduces the research background, the necessity of vehicle lightweight, and the requirements for end-of-life vehicle recycling. It reviews existing metal and CFRP joining technologies, including mechanical fastening, adhesive bonding, and welding. The chapter concludes with the research objectives and the importance of developing easily disassemblable joining techniques.

Chapter 2 investigates the direct joining of metals and CFRP using traditional ultrasonic welding methods, exploring factors affecting joint morphology and mechanical performance.

Chapter 3 details the specific shape design methods for the biomimetic rose thorn structures, abstracted into a mathematical geometric model. Numerical simulations analyze stress concentrations under various loads, determining the shape of the biomimetic structure for joining applications.

Chapter 4 focuses on manufacturing the biomimetic micro-protrusions identified in Chapter 3. These structures are fabricated on SPCC surfaces using FDM technology, including modeling, debinding, and sintering steps. This chapter provides insights into the thermal treatment process.

Chapter 5 characterizes and evaluates the joints of surface-structured SPCC (fabricated via FDM) and CFRP, including joint interface morphology, mechanical properties, and disassembly. It discovered that FDM is inaccurate when manufacturing millimeter-level products, particularly at the tip of the rose thorn biomimetic micro-protrusion, causing damage to CFRP. FDM-manufactured micro-protrusions exhibit deficiencies in mechanical performance, resulting in lower joint strength.

Chapter 6 explores key parameters and influencing factors in the SLM process for fabricating biomimetic rose thorn structures on metal surfaces. Given the low-power pulsed laser system (30W max) used, the interaction mechanism and influencing factors between the laser and SUS 316L particles are investigated.

Chapter 7 further analyzes joints' mechanical properties and disassembly process with SLM-fabricated biomimetic rose thorn structures. Experiments show SLM-manufactured joints exhibit excellent tensile strength, with fractures occurring in the CFRP substrate rather than at the joint interface. Disassembly tests demonstrate this structure allows complete separation of metal and CFRP with no significant defects post-disassembly.

This study proposes and validates the easily disassemblable joining method through innovative biomimetic design and advanced manufacturing techniques, providing new insights and pathways for metal-CFRP joining. The results improve joint strength and disassembly efficiency, contributing to the recycling of end-of-life vehicles and promoting environmentally friendly manufacturing. The research outline of this article is shown in Fig. 1-14.

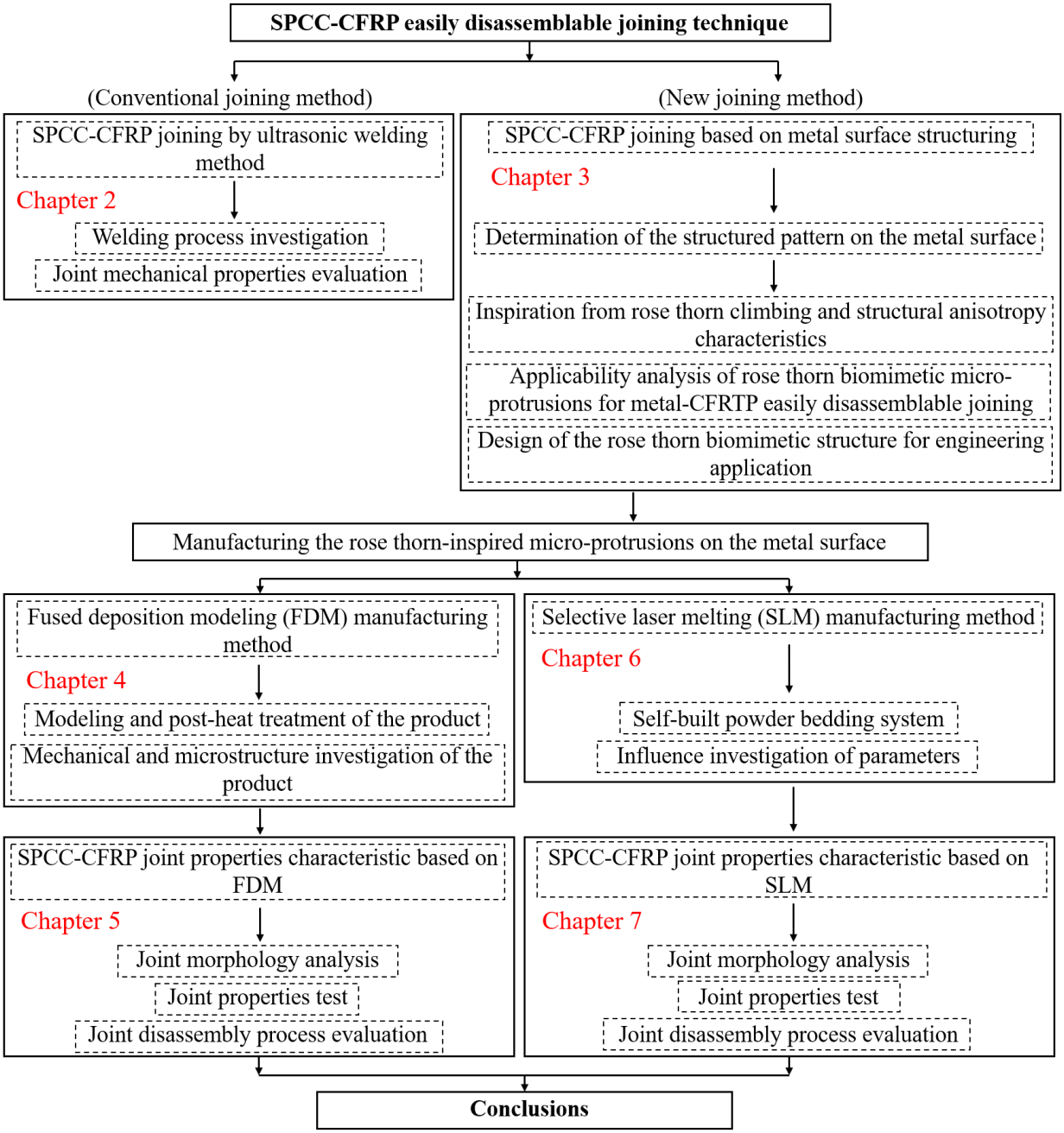

Fig. 1-14 Research outline of this paper.

Chapter 2: SPCC and CFRP Joint Performance Produced with an Additional Nylon-6 Interlayer by Ultrasonic Plastic Welding

Ultrasonic plastic welding (UPW), an efficient method widely employed in materials joining, offers a potential solution for the composite joining of metals and polymers. In this chapter, we initially attempt direct welding of SPCC and CFRP using the UPW method. The primary objective of this chapter is to systematically investigate the application of UPW in the joining of SPCC and CFRP through a series of experimental studies and to examine the role and transformation process of Nylon 6 as an intermediate layer in the joining process.

2.1 Introduction

In this study, the chopped CFRP is adopted as the composite component. These sheets feature exposed carbon fibers on their surface, posing a challenge for direct metal-CFRP hybrid joint formation due to significant physical and chemical disparities [59]. To achieve the intended purpose with this economical joining method, we introduced PA6 film as the thermoplastic intermediary layer because of its low crystalline nature and excellent compatibility with carbon fibers and metals. Additionally, a high-power digital hot plate (AS ONE Corporation, HP-1SA) as the preheating platform that complied with the UPW was applied to investigate the weldability and welding process of the metal-CFRP joint in this research.

In the UPW process, the local temperature increases quickly, leading to softening or melting of the PA6 layer, which is displaced from the welding zone underneath the pressure applied by the horn. Meanwhile, melted PA6 may fulfill the wetting on the metal surface, and the adhesion contact between metal and CFRP is realized. Nakara et.al. [122] has illustrated that the joining mechanism at the polymer and metal interface is hydrogen bonding. Therefore, this research focuses on the joining process and investigates welding energy and preheating temperature to illustrate the factors influencing hybrid joint performance and gain a feasible welding process. The role of welding energy, preheating temperature, and the synergetic effect were analyzed according to the joint's mechanical performance, microstructure morphology, and failure mechanisms.

2.2 Experimental Procedures

2.2.1 Materials

a) Chopped CFRP

The chopped CFRP with a nominal thickness of 0.5 mm, supplied by Fukui manufacturer Japan, was applied in this research. The typical properties of this chopped CFRP are listed in Table 2-1. This CFRP chopped sheet is manufactured by randomly distributing the thin layer of prepreg cut into strips on intermediate PA6 thermoplastic film. Fig. 2-1 shows the chopped CFRP. Fig. 2-1(a) is the chopped CFRP as received, and Fig. 2-1(b) is the top surface morphology of this chopped CFRP. The carbon fibers are exposed to the sheet surface and distributed regularly locally according to the chopped prepreg. Fig. 2-1(c) shows the cross-section of this chopped CFRP. It can be observed that the carbon fibers in the chopped prepreg at the upper position are distributed parallelly, while those in the lower chopped prepreg are oriented vertically. In between the two perpendiculars chopped prepreg is the PA6 intermediate thermoplastic film. Fig. 2-1(d) is the diameter of the carbon fiber that is around 7 μm. Due to the chopped prepreg being oriented in all directions, this chopped CFRP has pseudo-isotropic properties and can be laminated without worrying about the direction of carbon fibers. Therefore, this CFRP chopped sheet is excellent for three-dimensional shape manufacturing.

Table 2-1 CFRP chopped properties.

Fiber Volume Content	Resin Content	Thickness	Mass
50 (%)	39 (wt.%)	500 μm	500 g/m^2

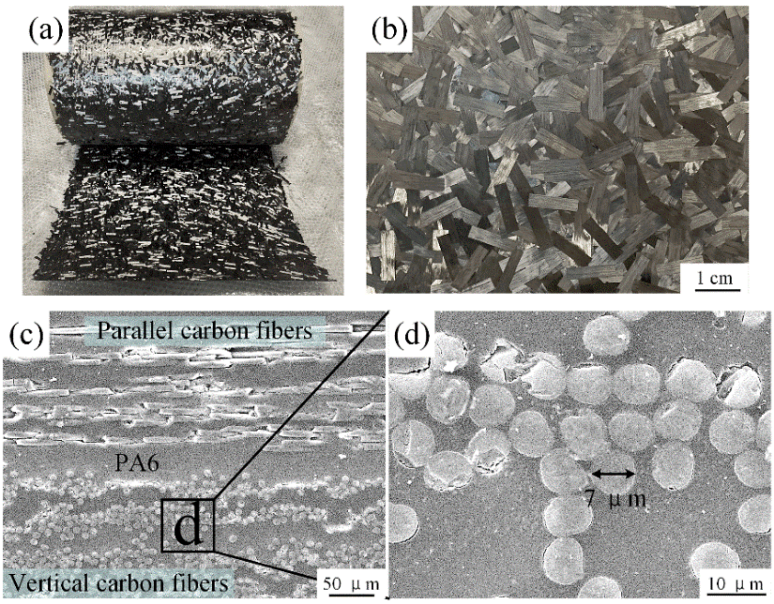

Fig. 2-1 Chopped CFRP material: (a) purchased chopped CFRP; (b) morphology of the chopped CFRP from the top view; (c) microstructure of the cross-section of the chopped CFRP; (d) carbon fiber diameter.

b) Steel Plate of Cold-Rolled Commercial (SPCC)

SPCC was used as the metal substrate in this research, which is one kind of primary metallic material applied to vehicle manufacture. Before fabricating the micro-protrusions, the SPCC surface was polished with 220 mesh sandpaper to remove the stain and other impurities and then degreased in acetone by an ultrasonic cleaner for 5 minutes to clean the organic containments and dust. Fig. 2-2 is the SPCC surface morphology after treatment. The surface roughness was calculated through a laser scanning microscope (KEYENCE VK-X Series), and the average surface roughness value in the range of R_a=2.0~4.0 μm is practical.

c) Nolyon-6 film

Moreover, PA6, a customary engineering plastic renowned for its outstanding mechanical properties and resistance to chemical agents and solvents [109] was employed in the experimental procedure. Table 2-2 enumerates the prevalent properties of PA6, according to the research findings of Natália M et al. [123, 124]. The thickness of the PA6 film directly impacts the formation of macroscopic mechanical anchoring between components, with 100 μm identified as the optimal value for achieving hybrid joints characterized by elevated single-lap shear strength. Consequently, this investigation opted for a 100 μm thick PA6 film as the intermediary layer, facilitating the direct joining process between SPCC and CFRP chopped sheet components.

Table 2-2 Physical properties of PA6.

Chemical Formula	$(C_6H_{11}NO)_n$
Melting point (℃)	225
Density ($\times 10^3$kg/m^3)	1.13
Molding temperature (℃)	226~298
Poisson ratio	0.38
Tensile strength (MPa)	75
Flexural strength (MPa)	100
Thermal expansion coefficient ($\times 10^{-5}$/K)	8.0
Thermal conductivity (W/(m・K))	0.2
Glass transition temperature (℃)	40~60
Autoignition Temperature (℃)	434

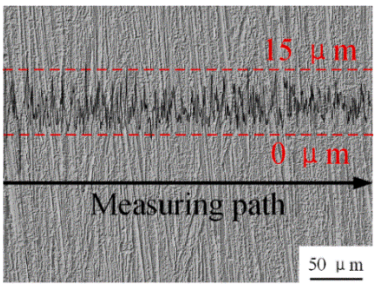

Fig. 2-2 SPCC surface morphology and roughness.

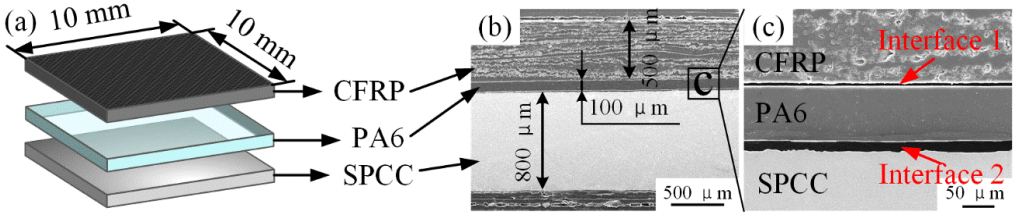

Fig. 2-3 Joint components: (a) schematic diagram of the joint composition (not in scale); (b) cross-section of the joint before joining; (c) interface 1 and 2, before joining.

2.2.2 Joint Design

The SPCC-CFRP hybrid joint designed in this research contains three components: the top layer CFRP chopped sheet, the middle layer PA6 film, and the bottom layer SPCC metal substrate, as schematically shown in Fig.2-3. Fig. 2-3(b) depicts the hybrid joint's cross-section structure and each component's thickness before joining. In the joining process of dissimilar materials, the interface situation is vital in characterizing the joining condition and the joint quality. Thus, two interfaces were defined to analyze the joining state and mechanisms: interface 1 between the CFRP chopped sheet and the PA6 film and interface 2 between the PA6 and the SPCC metal substrate, as illustrated in Fig. 2-3(c). The interspace between the two interfaces existed apparently before the joining, indicating no interaction between the joining components.

2.2.3 Ultrasonic Joining System

In the UPW process, energy weld mode was selected to produce the SPCC-CFRP hybrid joints. The four controllable joining parameters in energy weld mode are welding force, vibration amplitude, joining time, and energy, which influences the joining mechanisms and, consequently, the joints' microstructure and performance [125]. Welding force ensures the intimate contact behavior between the joining components and controls the deformation of the PA6 film and the CFRP chopped sheet [126]. Higher welding force may lead to a large amount of flowing of the

molten PA6 film and severe deformation of the CFRP chopped sheet. Thus, the joining pressure was kept at 100 N for all experiments. Welding energy is the main factor affecting hybrid joint properties [119].

In this research, welding energy and preheating temperature are determining factors for heat generation in the joining process, which affects the condition of PA6 film and is responsible for joint performance. Therefore, this research mainly investigated the effect of welding energy and preheating temperature on joint performance. The welding energy ranged from 300 J to 1500 J, and the selected preheating temperature values are 20 °C (room temperature), 50 °C, 80 °C, 120 °C, 160 °C, 200 °C (melting beginning point of PA6 film), and 240 °C (full melted temperature of PA6 film), respectively. The welding time is related to the welding energy; their relationship is shown in Fig. 2-4. The graphical representation of the system is depicted in Fig. 2-5, accompanied by a detailed table of other joining parameters.

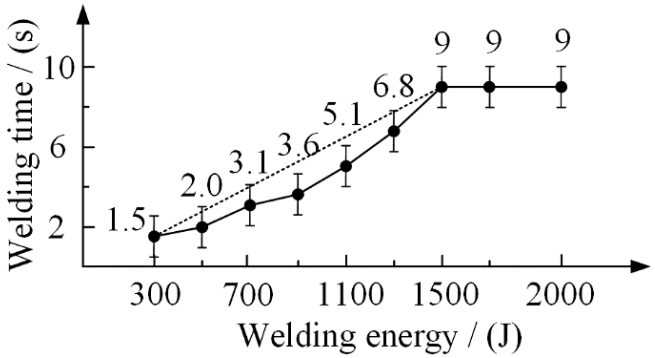

Fig. 2-4 Relationship between welding time and welding energy.

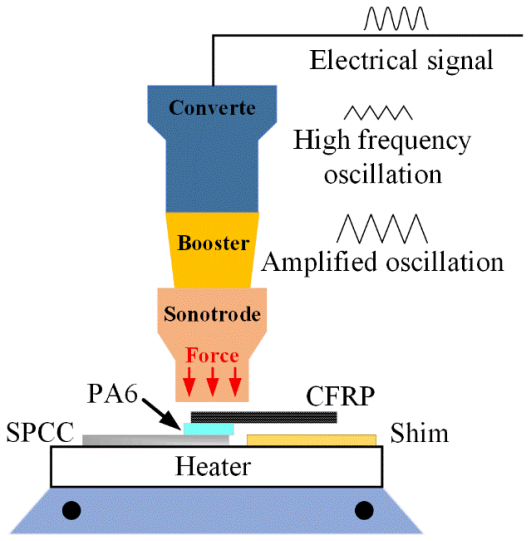

Joint area	15×15 mm^2
Max. US power	2000 W
US frequency	20 kHz
Amplitude	10 μm
US input energy	0~2000 J
Temperature	0~300 ℃
Trigger force	100 N
Welding force	150 N
Welding time	0~9 s
Hold time	1 s

Fig. 2-5 Schematic diagram of the ultrasonic plastic welding system complied with a heater.

2.2.4 Characterizations

a) Joint microstructure analysis

The joint interface joining condition obtained under different welding parameters was analyzed by SEM. The joints were previously cut from the middle by a fine-cutting machine, then embedded in cold-curing epoxy resin, followed by standard grinding and polishing procedures. Finally, the samples were sputter coated with a thin layer of gold for 1 min before the SEM observation.

b) Mechanical testing

The lap shear test evaluated the mechanical performance of the joint. The tests were conducted in a Zwick/Roell 1478 universal tensile tester based on standard ASTM D3163-01, with a 6 mm/min speed at room temperature. The dimension of the hybrid joint is shown in Fig. 2-6. Three replicates for each joining condition were tested, and the average of the three measurement results was reported as the joint strength.

2.3 Effect of UPW Energy at Room Temperature

UPW energy is the primary heat source for softening or melting the PA6 film at room temperature. The joint microstructure obtained under different welding energies was observed utilizing the SEM. Fig. 2-7 shows the joint's microstructure produced at room temperature under 500 J welding energy. In Fig. 2-7(a), the CFRP chopped sheet, PA6 film, and SPCC metal parts were easy to identify due to joint components being separated and keeping the original status. Consequently, the boundary of interfaces 1 and 2 can be observed clearly in Fig. 2-7(b), which indicates the ineffective joining between the joining components. In addition, some crevices were found at interface 2, further verifying the insufficient heat generation generated by 500 J welding energy at room temperature. With the same condition, when the welding energy was 300 J, it could not produce the hybrid joint either.

When the welding energy reached 700 J, the fusion phenomenon partly occurred at interface 1, as shown in Fig. 2-8. However, the interface 1 boundary still existed for most welding areas, and there was an interspace between the PA6 film and SPCC metal, filled by the cold-curing epoxy resin. Fig. 2-8(a) shows the edge morphology of the joint. Joining components can be identified, and they did not cause any deformation of the CFRP chopped sheet and PA6 film. This joining result led to insufficient joint strength, only 30 N around under the lap shear test.

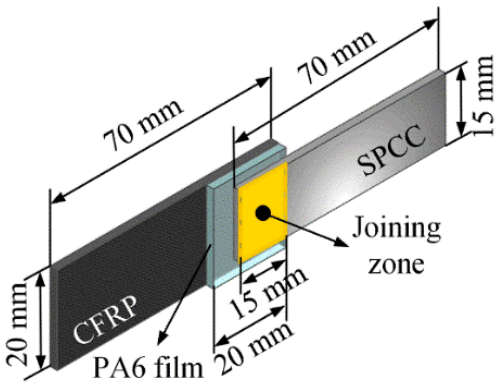

Fig. 2-6 Schematic diagram of the SPCC/CFRP hybrid joint.

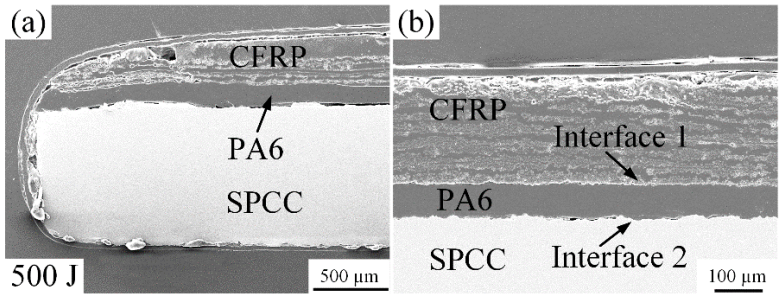

Fig. 2-7 Microstructure of the joint cross-section at the 500 J energy: (a) the corner of the joint; (b) interface morphology.

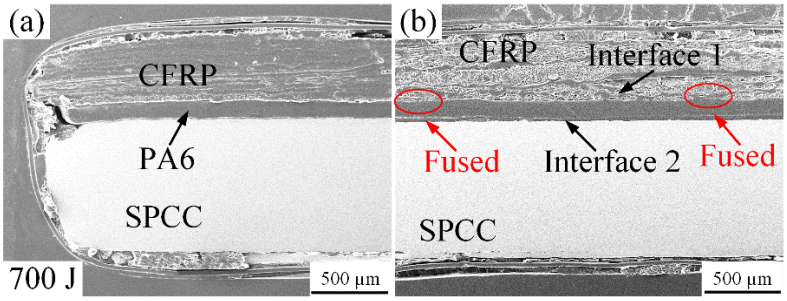

Fig. 2-8 Microstructure of the joint cross-section at the 700 J energy: (a) carbon fibers squeezed out phenomenon; (b) situation of interface 1 and 2.

When the welding energy reached 900 J, the carbon fiber bundles were squeezed to the joint edge accompanied by the PA6 film melting, as shown in Fig. 2-9(a), which is different edge morphology from Fig. 2-7(a) and Fig. 2-8(a). Meanwhile, the PA6 film fused with the chopped CFRP, and interface 1 disappeared, as shown in Fig. 2-8(b). It suggests that the high oscillation under 900 J welding energy can cause the melting and interdiffusion at the boundary of the PA6 film and the chopped CFRP. Efficient cohesion was guaranteed between the PA6 film and CFRP chopped sheet. This phenomenon can be explained by the fact that during the UPW process, PA6

film melted rapidly under the action of welding energy. Subsequently, the melted PA6 film enveloped the exposed carbon fibers on the surface of the CFRP chopped sheet, and under the welding force exerted by the horn, they were compressed from the center towards the joint edge. However, for interface 2, some crevices still occurred, indicating that the molten PA6 film did not fill the SPCC surface. It also needs to be mentioned that the carbon fibers can remain at the initial status after the welding process under 900 J welding energy.

The disappearance of interface 1 under 900 J welding energy proves that effective joining between the PA6 film and CFRP can be achieved by improving the welding energy. However, the crevices at interface 2 were not fully resolved yet, as shown in Fig. 2-10. Thus, the welding energy continued to increase in an attempt to solve this problem. When the welding energy reached 1100 J, the number of carbon fibers and molten PA6 film squeezed to the joint edge increased in Fig. 2-10(a). Interface 1 disappeared in the same way as Fig. 2-9. In addition, carbon fibers were observed to have been damaged due to the strong ultrasonic oscillation under 1100 J welding energy. Cracks appeared at the cross-section of the carbon fiber perpendicular to the ultrasonic vibration direction, which is observable in Fig. 2-10(c). Meanwhile, the crevices still existed at interface 2.

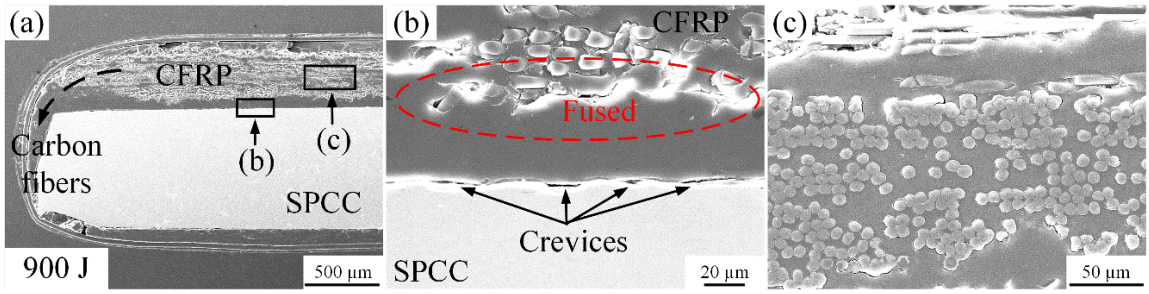

Fig. 2-9 Microstructure of the joint cross-section at the 900 J energy: (a) carbon fibers squeezed out phenomenon; (b) situation of interface 1 and 2; (c) carbon fibers.

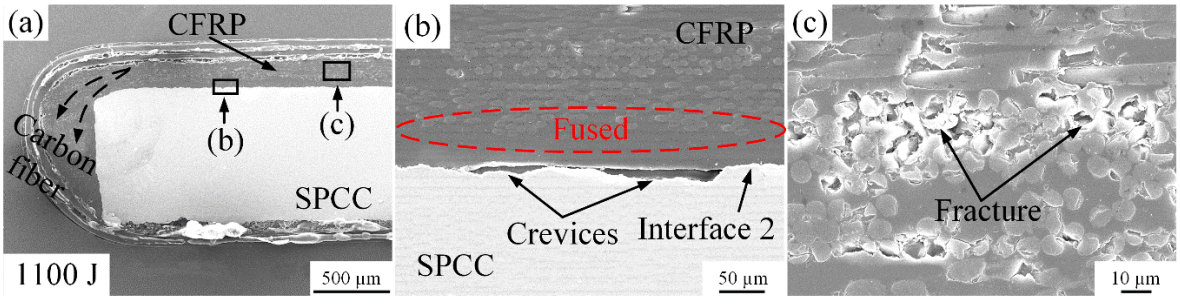

Fig. 2-10 Microstructure of the joint cross-section at the 1100 J energy: (a) carbon fibers squeezed out phenomenon; (b) situation of interface 1 and 2; (c) fractures happened on carbon fibers.

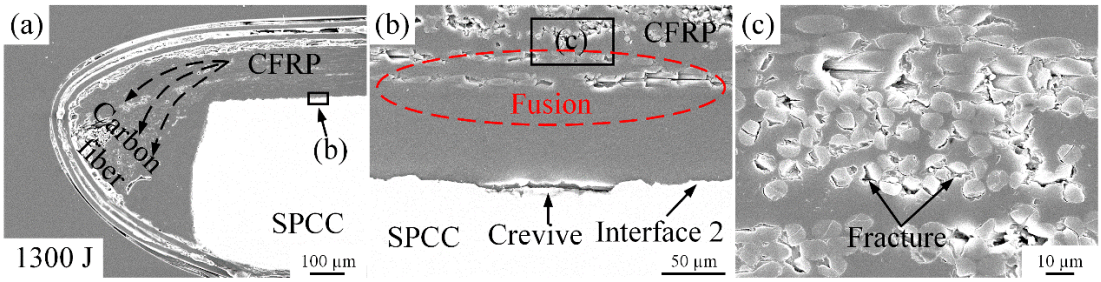

Fig. 2-11 Microstructure of the joint cross-section at the 1300 J energy: (a) carbon fibers squeezed out phenomenon; (b) situation of interface 1 and 2; (c) fractures on carbon fiber.

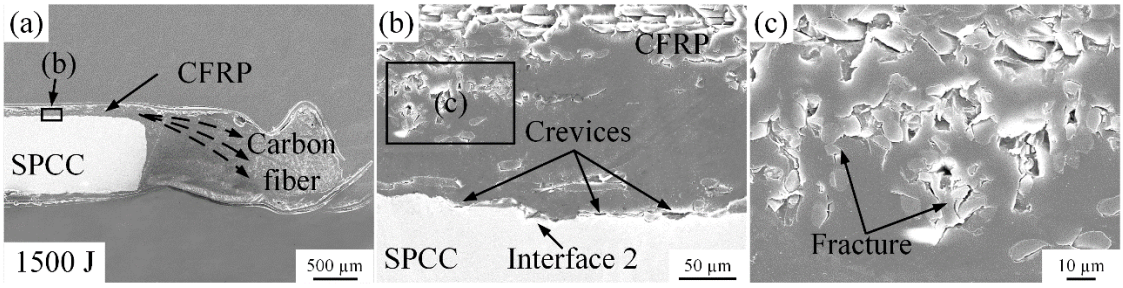

Fig. 2-12 Microstructure of the joint cross-section at the 1500 J energy: (a) carbon fibers squeezed out phenomenon; (b) situation of interface 1 and 2; (c) fractures on carbon fiber.

To further verify the high welding energy on the microstructure of the joint interface at room temperature, the welding energy was increased to 1300 J and 1500 J. Fig. 2-11 and Fig. 2-12 show the related microstructures, respectively. When the welding energy reached 1300 J, the squeezing phenomenon and the damage to the carbon fibers got more serious, as shown in Fig. 2-11(a),(c). When the welding energy reached 1500 J, more serious squeezing and damage phenomena happened in Fig. 2-12(a),(c). However, the crevices at interface 2 still cannot be eliminated even though under the high welding energy that can damage the carbon fibers and squeeze almost all melted PA6 film and carbon fibers out to the joint edge.

The crevices' occurrence was considered a joining defect that led to poor joint properties. From the above experiments, it was found that this joining defect cannot be eliminated by solely increasing welding energy at room temperature. Microstructural analysis at interface 2 illustrated that the crevices always occurred at the depression area of the SPCC surface, as schematically described in Fig. 2-13. During the welding process, the bulge area of the SPCC surface was more feasible to bond with the PA6 layer due to the direct connection. In contrast, the depression areas of the SPCC surface cannot be filled in a dramatic welding process. The main reason is that UPW technology is a high-speed joining technology. Therefore, PA6 film dramatically reached a high-temperature degree and then solidified in a short period. Thus, the short welding time and high

cooling rate cannot enable a sufficient spreading of the molten PA6 film at the depression area of the metal surface, which leads to the generation of crevices at interface 2.

In addition, to investigate the effect of welding energy on joint properties at room temperature, the thickness variation of the PA6 film and CFRP chopped sheet during the welding process was also measured under different welding energy, shown in Fig. 2-14, which can be seen as a characterization to evaluate the effect of the welding energy at room temperature. It appears that the PA6 film thickness was kept at 100 μm before 500 J welding energy, proving that the generated oscillation heat was insufficient to melt the PA6 film and produce the hybrid joint. However, for the CFRP, the thickness showed a gradual decrease trend with the energy increasing at the beginning. This is mainly due to the interspace among the CFRP chopped sheet. Under the ultrasonic oscillation action, the CFRP chopped sheet got more compressed, and the interspace between the prepreg layer was excluded. When the welding energy arrived at 700 J, the PA6 film thickness decreased to 93 μm. This indicates that the PA6 film softened under 700 J, and with the compression action applied by the horn pressure, the thickness of the PA6 film decreased. In addition to the softening phenomenon of the PA6 film, the partial region started to melt under the 700 J welding energy. As the microstructure analyzed in Fig. 2-8 indicates, the 700 J is the starting energy point of the effective joining. With the increase of the welding energy, effective joining can be achieved around interface 1, but due to the squeezing phenomenon, the PA6 film and CFRP chopped sheet thickness significantly decreased.

From the above analysis, the effect of the welding energy on the joint at room temperature can be divided into three modes: compaction mode, joining mode, and damage mode. When the welding energy was less than 500 J, it belonged to the compaction mode. In this mode, the energy heat is insufficient to generate effective joining, the PA6 film was kept at the initial status, and the chopped CFRP was compressed only. During the 700 J to 900 J welding energy, the PA6, and the CFRP chopped sheet can somewhat generate effective joining. In the damage mode, welding energy higher than 1100 J, carbon fiber fractures occurred on the surface following the serious squeezing phenomenon of the PA6 interlayer and carbon fibers. This indicates that the UPW energy should be limited to 900 J when applied to bare carbon fibers.

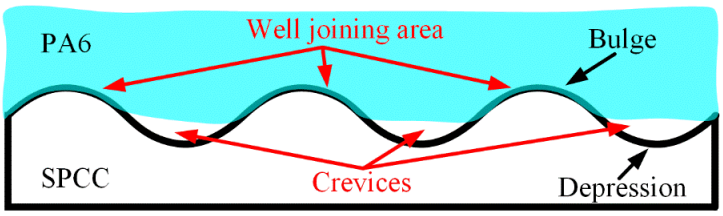

Fig. 2-13 Schematic diagram of the joining result by the sole role of UPW energy.

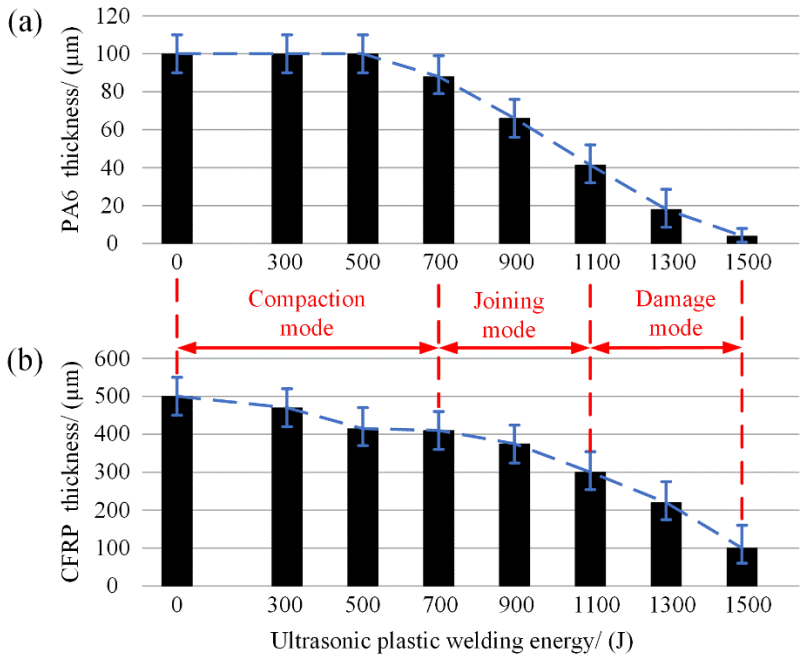

Fig. 2-14 The trend of the thickness variation: (a) PA6 film; (b) CFRP chopped.

2.4 Effect of the co-action of Preheating Temperature and Welding Energy

From the above experiments carried out at room temperature, it can be seen that solely welding energy cannot generate the effective joining of the SPCC-CFRP hybrid joint with the addition of PA6 intermediate layer; the crevices defects occurring at interface 2 has a severe impact on the joint properties, and it cannot be eliminated by solely increasing the welding energy. In addition, the joining process window obtained under the only action of ultrasonic joining energy is very narrow. Therefore, eliminating crevice defects and enhancing micro-mechanical interlocking is essential to improve joint mechanical properties.

An external heater instrument was applied with the UPW system to solve these shortcomings to generate the SPCC-CFRP hybrid joint. The following experiments, listed in Fig. 2-15, were carried out to investigate the effect of the preheating temperature and welding energy and the

synergistic result. The previous results showed that welding energy should be limited to 900 J in the following experiments to avoid carbon fibers damage. Under the combined action of ultrasonic welding energy and preheating temperature, the addition of the PA6 film contributed to the generation of the SPCC-CFRP hybrid joint.

The co-effect of the preheating temperature and welding energy on the hybrid joint's mechanical performance was evaluated utilizing lap shear tests. Fig. 2-16 reports the shear strength results under different joining conditions. It depicts that when the preheating temperature was lower than 80 °C, and the welding energy was less than 500 J, the joining components did not generate adhesion and separated from each other, which led to zero lap shear strength of the joint. With the increase of preheating temperature and welding energy, sectional joining began to appear among the joining components, and the lap shear strength started improving. However, the joint's most giant lap tensile strength is less than 400 N when the preheating temperature is lower than 160 °C. The joint lap shear strength sharply increased when the preheating temperature reached 200 °C. The best joint strength was obtained when the preheating temperature reached 240 °C, and the maximum value was around 1300 N. Meanwhile, the tensile test had almost the same matter under different welding energy, indicating the welding energy did not play an essential role in the joint mechanical performance under 240 °C preheating temperature.

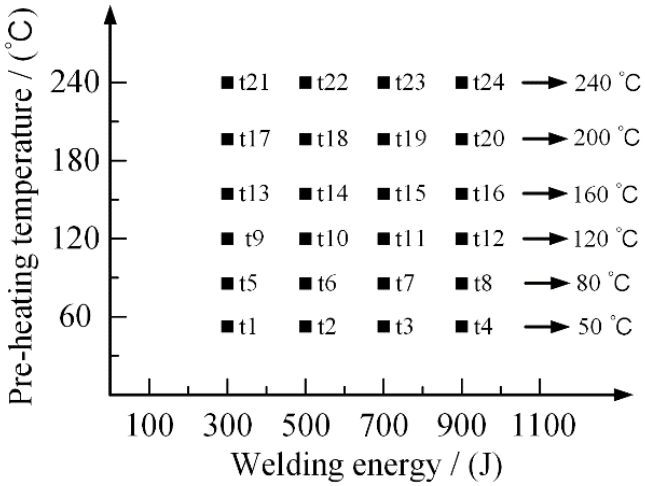

Fig. 2-15 Design of the experiments.

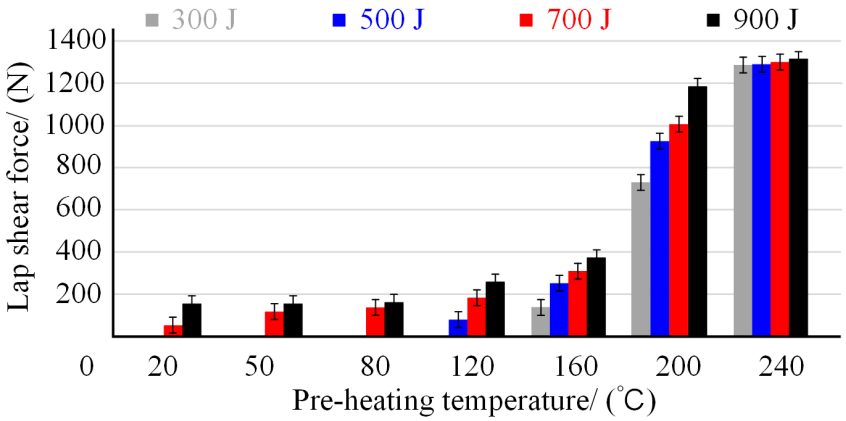

Fig. 2-16 Ultimate lap shear strength of the joints under different joining parameters.

According to the lap shear test results, the conditions of the joints obtained under different welding energy and preheating temperatures can be divided into three categories. The tests in the yellow frame in Fig. 2-17 belong to Category 1, the tests in the blue frame belong to Category 2, and the red frame is Category 3. Category 1 had the worst mechanical performance, the SPCC metal component was completely separate from the other parts, and only a tiny area of PA6 film was fused with the CFRP chopped sheet. The dashed red line in Fig. 2-18 shows the representative fracture surface morphology, which represents the joining area between the PA6 film and the CFRP chopped sheet. Only a tiny space was melted between the PA6 film and CFRP chopped sheet and got adhesive under the welding energy oscillation effect, and under the different joining energy, the joining area is different. It indicates that the lowest energy did not adequately join the hybrid adherents.

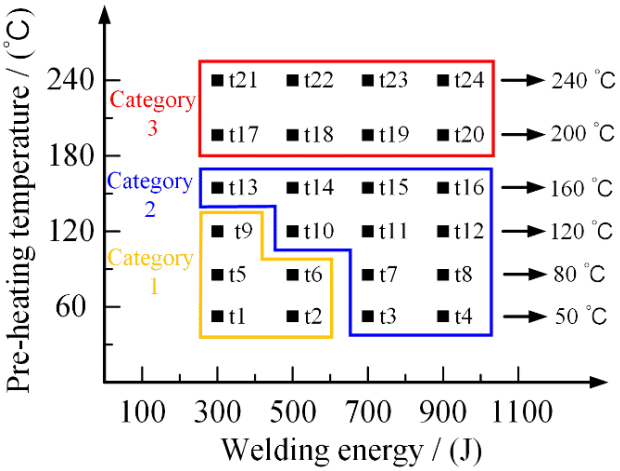

Fig. 2-17 Joining process window of the SPCC-CFRP hybrid joint by the UPW.

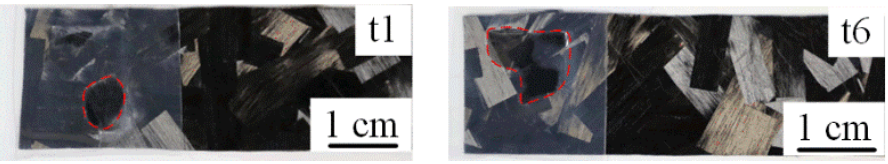

Fig. 2-18 Representative fracture surface of Category 1.

In Category 2, the lap shear strength increased with preheating temperature and welding energy improvement. Fig. 2-19 shows the representative fracture surfaces of the hybrid joints of Category 2 and finds that the welding zone increased with preheating temperature and welding energy. It indicates that the increased welding zone of direct contact between the PA6 film and the SPCC is responsible for the slightly increased mechanical performance of the SPCC-CFRP hybrid joints. In this joining category, preheating can change the mechanical properties of the CFRP plastic matrix, lowering Young's modulus and softening so that the ultrasonic deformation and melting of the matrix can easily occur with less welding energy. Approximate joint strength could be obtained under different joining conditions for some cases, such as t12 and t14, showing almost the same strength value. These cases' tendency shows that preheating temperature reduces the welding energy to a certain extent. The observation of the joint's microstructure found that the crevices still existed but presented a decreasing tendency with the growth of the total input energy. Therefore, adding the interlayer can enhance the joints' mechanical strength due to the larger welding area and fewer crevices.

A significant increase in joint strength was observed when the welding condition belonged to Category 3. When the preheating temperature reached 200 °C, the PA6 film melted before the joining process but could not completely dissolve. Therefore, the viscosity of the molten and softened PA6 film favors the metal surface's wettability. Under the co-action of welding energy, the adhesion forces were finally applied to the joint. However, due to the insufficient melting of PA6 film under 200 °C preheating temperature, welding energy still played an essential role in the joint strength. As the welding energy increased, the melting mount of the PA6 film increased and became more compressed under the oscillation effect, which in turn led to an increase in the joint strength. This joining condition produces joints with higher mechanical strength and smaller amounts of microstructural defects. Microstructural analysis proves that crevices that occurred at interface 2 have been eliminated under this joining condition, as shown in Fig. 2-20. The PA6 film co-cured with the chopped CFRP has an active role in the bonding mechanism during the ultrasonic joining, and an effective micro-interlocking was achieved due to the 200 °C preheating.

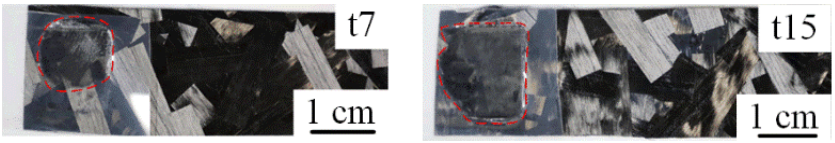

Fig. 2-19 Representative fracture surface of Category 2.

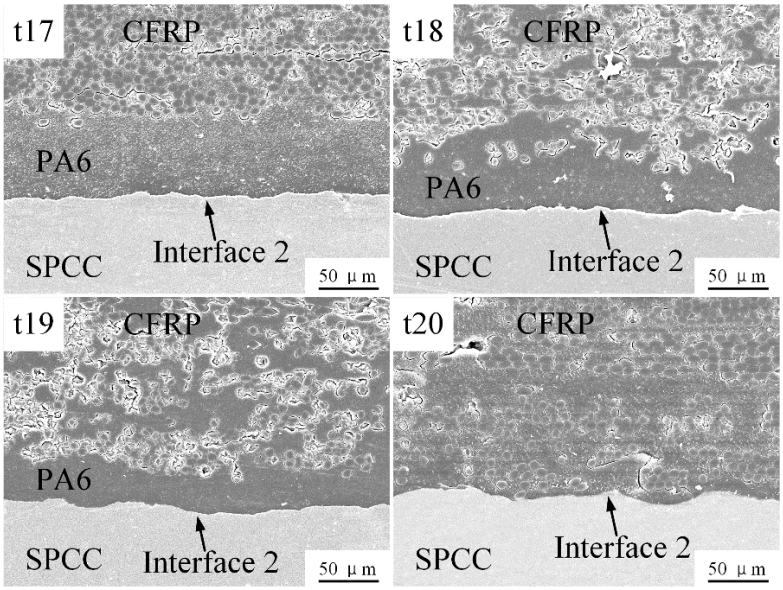

Fig. 2-20 Microstructures of interface 2 obtained under 200 °C.

Unlike the partial melting under 200 °C preheating temperature, the PA6 film can be fully melted at 240 °C before welding. Therefore, the depression area on the SPCC surface can be filled by the melted PA6 film under the action of welding energy oscillation and welding force, and an effective micro-mechanical interlocking could be established at interface 2. Fig. 2-21 shows the joints' cross-section microstructures with no crevice defects generated. However, due to the different welding energies, the compression amount of the PA6 film was different. With the increase of the welding energy, the more melted PA6 film could be squeezed to the joint edge, leading to decreased distance between carbon fibers and the SPCC. Fig. 2-22 is the representative fracture surface obtained under 240 °C. It enabled us to understand that the large welding zone allows good joint mechanical results.

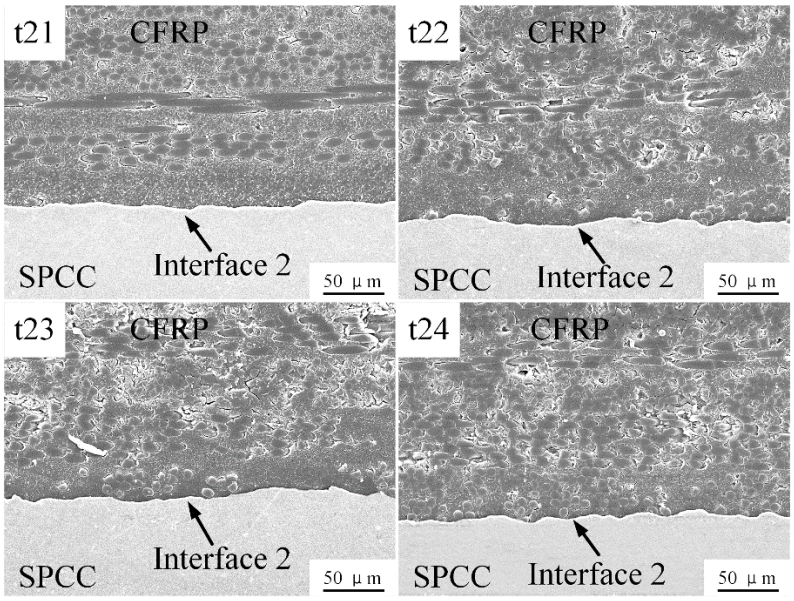

Fig. 2-21 Microstructures of interface 2 obtained under 240 °C.

Fig. 2-22 Representative fracture surface of Category 3.

From the above analysis, it can be found that the preheating temperature dramatically affects the quality of the hybrid joint interfacial zone. The crevices defects at interface 2 are responsible for the poor joint strength. The microstructural analysis demonstrated that the wide spreading of the molten PA6 film under the high preheating temperature can fill the depression area on the SPCC surface, which generates the micro-mechanical interlocking between the joining components. The joint lap shear strength is thus increased. In addition, the severe squeezing phenomenon of carbon fibers can be avoided due to the preheating temperature.

2.5 Conclusions

Ultrasonic plastic welding joints of chopped CFRP and SPCC with an additional PA6 film intermediate layer were prepared and analyzed regarding their microstructures and mechanical strength. It showed the feasibility of the ultrasonic plastic welding process and optimized the joining process. From the above analysis and discussion, the following conclusions can be drawn:

1、Nylon 6 film can be used as an intermediate layer and ultrasonically welded to obtain an

effective metal and bare carbon fibers hybrid joint through the optimized joining parameters. The melting of the PA6 film is the key to the fusion of carbon fibers and PA6 film, while the widespread spreading of the melted PA6 film on the depression area of the metal surface guarantees the final joint strength.

2、With the sole effect of ultrasonic welding energy at room temperature, the bare carbon fibers can have a good fusion with the PA6 film. Still, it cannot generate an effective joining between metal and the PA6 film. Insufficient joining, narrow welding process windows, and carbon fiber damage at high welding energy are the primary defects that cause poor joint strength.

3、The joining condition between the metal and the PA6 film is essential to ensure joint strength. The micro-mechanical interlocking generated on the rugged metal surface contributes to the mechanical performances of the ultrasonically welded hybrid joints.

4、Effective preheating can reduce crevice joining defects at the SPCC and the PA6 film boundary, guaranteeing the molten PA6 film's adequate spreading on the depression area on the metal surface and improving the welded joint's mechanical strength. Furthermore, preheating can reduce the welding energy, which is beneficial for the severe squeezing phenomenon and avoids carbon fiber damage.

Chapter 3: Design of the Rose Thorn Biomimetic Structure for Metal Surface Structuring

Based on the overall research scope, this study focuses on the easy disassembly joining technique for SPCC and CFRP. This chapter initially establishes the utilization of structured metal surfaces to achieve easy disassembly joining between metal and CFRP. This chapter will outline the methodology for determining the shapes employed for the structuring pattern on metal surfaces, provide a theoretical analysis of how this structure facilitates the facile detachment joining between metal and CFRP, and elucidate the precision design considerations for this structure.

3.1 Biomimicry Application in Engineering

Throughout billions of years of evolution, nature has served as an enduring wellspring of inspiration for researchers and engineers, offering invaluable insights that drive advancements benefiting both humanity and the environment [127, 128]. This concept of biomimicry, rooted in the observation, understanding, and imitation of biological structures and functions, has emerged as a fundamental approach to addressing engineering challenges [129]. Drawing inspiration from the intricate structures, morphologies, and functionalities found in nature, researchers seek to design innovative solutions that mimic biological entities. Examples abound, ranging from the self-cleaning properties of lotus leaves to the robust anchoring mechanisms of tree roots, the adhesive capabilities of barnacles, and the flexible strength of elephant trunks, as shown in Fig. 3-1 [130-132]. These natural marvels serve as tangible embodiments of the potential for biomimetics to revolutionize engineering practices and pave the way for transformative technological breakthroughs. The application of biomimicry in engineering has significantly expanded into the realm of material connections [133]. Nature provides an abundance of remarkable structures conducive to high-performance material connections, such as spider silk, shell structures, tree roots, dragon bone structures, and petal morphologies [133, 134].

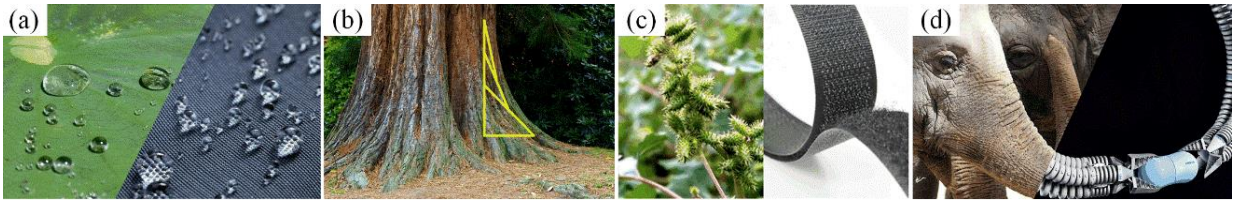

Fig. 3-1 Biomimicry application examples in engineering: (a) Lotus leaves and hydrophobic materials; (b) Root shape and stable structure; (c) Xanthium and Velcro; (d) Elephant trunk and gripper [130-132].

Each of these structures offers unique properties that enhance the strength, durability, and adhesion of material joining. By borrowing strategies from the natural world, engineers can design structures with outstanding performance characteristics, shaping the future of material joining across various applications. Simultaneously, the ongoing exploration of biomimetics and integrating these principles into engineering practices pave new pathways for innovation and sustainable development.

3.2 Analysis of Rose Thorn Functions and Morphology

Rose plants, classified as climbing plants, feature thorns as specialized structures predominantly found on their stems [135]. These thorns serve multifaceted functions within the plant's life cycle and ecological context, like defense and protection, competitive exclusions, and support and climbing. In biomimetics, the features of rose thorns have been applied to various engineering applications [136]. For example, researchers have designed a protective device called a "Thorn Tube" based on the structure and morphology of rose thorns. This device, resembling rose thorns, exhibits similar features, such as twisting, slender, and rigid characteristics. It effectively prevents intruders from entering properties and has potential applications in various security systems.

While the primary application of rose thorns in biomimetics relates to protection and defense, their unique structure and morphology also have potential applications in joining, considering their climbing property [137]. Rose plants utilize their thorns, which have sharp and curved tips, to grasp surrounding supports such as trees, fences, walls, etc., like in Fig. 3-2. This allows them to insert and hold onto supports firmly, and by growing along these supports, rose plants can gain better living space. Thus, one potential application of rose thorns in joining is the design of new fasteners or interlocking mechanisms. The twisting and hook-like shape of thorns can contribute to creating interlocking connections that are more secure and durable than traditional fasteners and facilitate disassembly at joints. This study aims to leverage the anisotropic properties of rose thorn structures for use in joining metal and carbon fiber composite materials. A protruding structure has been designed on the metal surface to achieve metal-CFRP joining that is more robust, reliable, and easily disassembled.

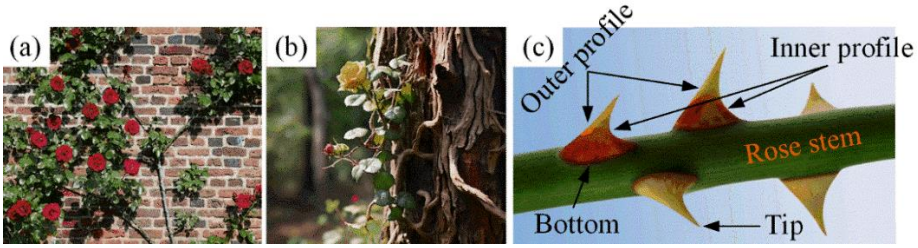

Fig. 3-2 Rose and rose thorn in nature: (a) rose climbs on a wall; (b) rose climbs on a tree; (c) rose thorn's shape.

3.3 Analysis of Rose Thorn Biomimetic Micro-Protrusion Morphology and Mechanical Performance for Metal-CFRP Easy Disassembly Joining

However, recognizing the inherent challenges within the intersection of biomimetics and the following manufacturing, it is imperative to acknowledge the impracticality of directly replicating the morphology of rose thorns in the joining process of dissimilar materials [138, 139]. This is attributed to significant disparities between natural materials and those employed in engineering applications [140, 141]. Consequently, this chapter is motivated by the pivotal objective of exploring alternative design strategies for micro-protrusion shapes inspired by the structure of rose thorns and tailored explicitly for the metals-CFRP easily disassembled joining technique.

3.3.1 Definition of the Micro-Protrusion's Geometrical Model

Rose thorns exhibit distinctive morphological features that have evolved in the natural world. These features include a pointed tip, a curved profile, and an approximately elliptical base. These evolutionary traits serve specific mechanical functions, aiding roses in climbing and survival [142]. The gradual taper of the thorn's tip enhances its ability to penetrate surfaces. The curved profile is conducive to effective adaptation during climbing, while the elliptical base ensures stability on the rose stem.

In this study, the shape of the micro-protrusions has been depicted as convex with a tapering tip, curved sides, and elliptical bottom, as shown in Fig. 3-3. These geometric features can better represent the morphological features of rose thorns for the engineering biomimetic application design. Based on these geometric features, four essential geometrical parameters were extracted to characterize the micro-protrusion geometric model:

a) Base shape (α)

The micro-protrusion base shape has been approximated as circular or elliptical to ensure uniform load distribution and strong stability with the metal substrate. In this research, we

introduced a parameter $\alpha, \alpha = a/b$, representing the ratio of the semi-major axis, a, to the semi-minor axis, b, to describe the base shape, which ranges from circular to various elliptical.

b) Length (l)

The horizontal distance from the thorn's tip to the center of the base and the symbol is *l* in this research. It represents the apex position and orientation of the rose thorn-inspired micro-protrusion, which significantly influences the subsequent joining and disassembly process.

c) Height (h)

The vertical distance from the thorn's apex to the base center. The height of the micro-protrusion can affect its sharpness and penetrating ability in the joining process. Higher micro-protrusion is generally sharper, providing more robust anchoring and penetrating power. Considering the following joining process in our research series where the CFRP thickness is less than 1 mm, the micro-protrusion's height was fixed at 1mm in this paper to minimize the unintended damage to the CFRP and reduce the overall weight.

d) Side curvature (Outer profile and Inner profile)

The curved profiles describe the curvature or bending degree of the micro-protrusion. In this study, we introduced the concepts of outer and inner profiles to delineate the micro-protrusion's side shape, as shown in Fig. 3-3. The outer profile delineates the raised edge of the area. In contrast, the inner profile illustrates the recessed region within the model. The outer and inner profiles are pivotal in enhancing joint strength and disassembly efficiency.

Furthermore, the micro-protrusion models were assumed to be symmetrical along the vertical plane perpendicular to the major axis of the base in this study. By defining these geometric parameters and assumptions, valuable insight into the morphological characteristics of rose thorns was established, which can used to finely control the shape characteristics of every part of the micro-protrusion.

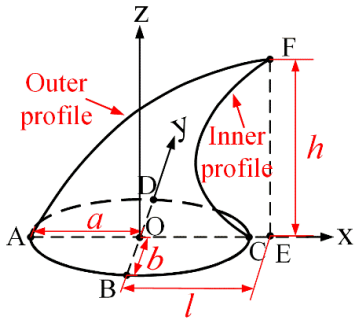

Fig. 3-3 Biomimetic shape and geometric parameters of rose thorn biomimetic micro-protrusion.

3.3.2 Analysis of Joining Strength Enhancement and Easy Disassembly Achieving

This research aims to develop the easily disassembled joining technique between metals and CFRP, and the rose thorn-shaped protrusion is promised to achieve this goal as an intermediate structure due to its unique geometric shape. Fig. 3-4 illustrates the working principle of the micro-protrusions as intermediaries in the metals-CFRP joining process. Rose thorn-shaped protrusions should be initially formed on the metal substrate surface, as shown in Fig. 3-4(a). In the following joining process, the tip of the rose thorn biomimetic structure is initially embedded into the interior of the CFRP under external force. Subsequently, following the gradual contour of the rose thorn structure, it progressively penetrates the entire CFRP step by step, Fig. 3-4(b) and Fig. 3-4(c). This approach effectively prevents damage and failure of the CFRP.

The performance of the micro-protrusions in the context of robust joining and easy disassembly of the metal-CFRP joint can be summarized as follows:

Joining strength enhancement

When the joining process is finished under external force and energy, the expected joint can be illustrated in Fig. 3-5.

a) Increased contact area:

The structured metal surface created with micro-protrusions has an increased surface roughness and contact area, which can counteract the external loads and prevent shear slip or delamination between metals and CFRP, enhancing the overall joint strength.

b) Mechanical locking and hydrogen bonding co-effect:

The tapered tip of the micro-protrusion can effectively penetrate CFRP, while the curve profiles establish a robust mechanical locking effect. This locking mechanism enhances resistance and prevents any undesired movement between the connected interfaces. Moreover, during the welding process, the external energy input caused the resin on the CFRP surface to melt, forming hydrogen bonding with the SPCC surface [112, 143]. This interaction increases shear and peel strength, resulting in a more durable and stable joint.

c) Optimized stress distribution:

The structured metal surface transforms stress distribution, evenly distributing joining stresses across the contact area. This prevents stress concentration, lowers the risk of cracks or fractures, and enhances the joint's overall strength and durability.

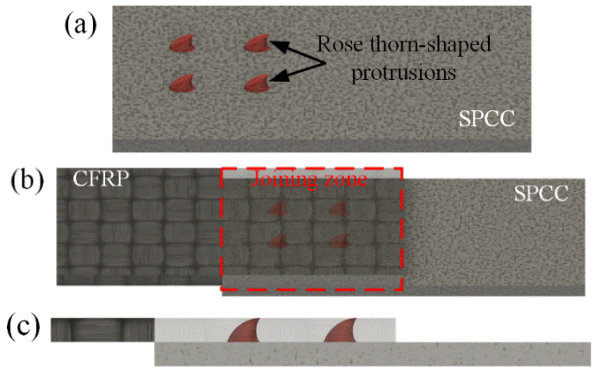

Fig. 3-4 Schematic of the rose thorn biomimetic micro-protrusions serve as intermediaries for metals-CFRP easily disassembled joining: (a) micro-protrusions formed on the SPCC surface; (b) the joint diagram of the SPCC-CFRP; (c) cross-section of the joint.

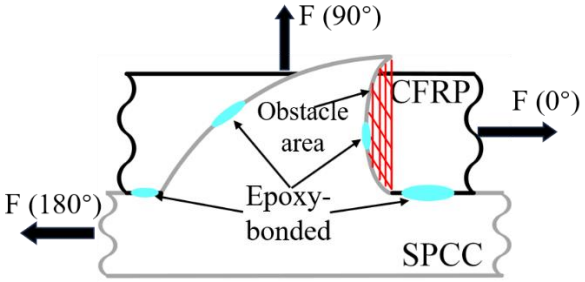

Fig. 3-5 Schematic diagram of joining strength enhancement.

Easy disassembly achieving of the metal-CFRP joint

a) Easy for separation point generation:

The connection between the CFRP and metal at the outer curved profile base is achieved through adhesive bonding, as illustrated in Fig. 3-6. Due to the relatively low viscosity of the resin on the surface of CFRP, this specific location can serve as a convenient initiation point for disassembly. This feature facilitates a smoother separation beginning when disassembling the CFRP at this junction.

b) Clear disassembly orientation:

The progressively tapering geometric design of the micro-protrusion outer profile provides distinct guidance during the disassembly process. As the tip gradually narrows, the initiation point and separation angle become more easily discernible, thereby enhancing the precision and efficiency of the disassembly procedure. The entire disassembly process diagram is illustrated in Fig. 3-6.

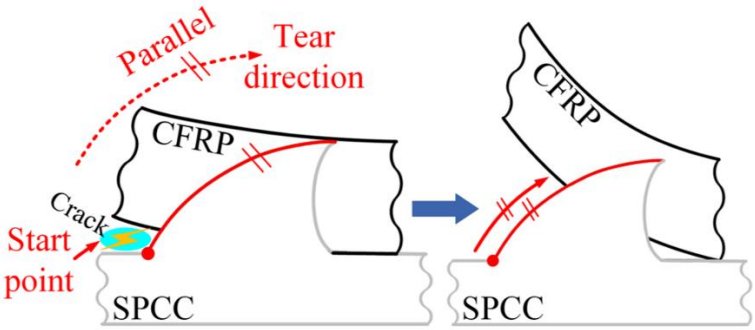

Fig. 3-6 Schematic diagram of easy disassembly achieved of the metal-CFRP joint.

3.4 Design Procedures of the Micro-Protrusion's Shape

This chapter fine-tuned the micro-protrusion features based on numerical simulations of static stress under various loads. The goal was to achieve an optimal shape that benefits the stress distribution and strength within the joint, enhancing its ability to withstand shear loads and reduce potential damage from stress concentration.

3.4.1 Numerical Simulation Methodology and Parameters Setting

In the rose thorn biomimetic micro-protrusion design, three-dimensional models with various geometric parameters were meticulously constructed utilizing Autodesk's Fusion 360 2.0 version software. These models were created to comprehensively analyze maximum stress conditions under varying loads. Fusion 360's robust modeling and simulation capabilities provided a powerful toolkit for exploring the intricate interplay between the micro-protrusion's shape and the stress concentration. Throughout the simulation conducted in Fusion 360, the analysis was based on the Von Mises stress criterion, a method utilized to assess the material's strength under complex multi-axial stress conditions.

Table 3-1 Materials properties.

Properties	**Values**
Density	7.85 E-06 kg/mm³
Young's Modulus	210 GPa
Poisson's Ratio	0.3
Yield Strength	207 MPa
Ultimate Tensile Strength	345 MPa

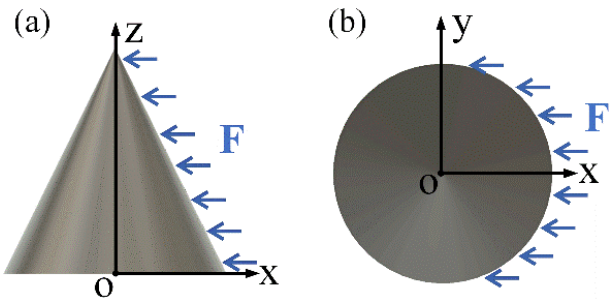

Fig. 3-7 Load condition of the micro-protrusions: (a) front view refer to Fig. 3-3; (b) top view.

Cold-rolled steel stands as a critical metallic material in the structural manufacturing of vehicles [10]. Consequently, steel was chosen as the primary material for the micro-protrusion. Material properties are shown in Table 3-1. These properties were defined strictly with Fusion 360's settings to ensure precision and accuracy.

For load conditions, the micro-protrusion experiences predominantly biaxial loading, with forces applied along the x and y axes throughout its operational lifespan, as depicted in Fig. 3-7. It is important to note that these applied loads remain unaffected by gravitational forces. This biaxial loading scenario establishes a controlled environment for evaluating the biomechanical response of the rose thorn-inspired micro-protrusions. Furthermore, constraints were imposed on the model's base to maintain immobility throughout the simulation process. These constraints preserve the micro protrusions' structural integrity, ensuring they retain their desired shape during the simulation.

This study employed Fusion 360's built-in automatic meshing functionality to construct finite element models with a model-based size of 4%, element order set to parabolic, and a minimum element size equivalent to 20% of the average size. Fusion 360's integrated meshing tools automatically transform the geometric model into a discretized mesh suitable for finite element analysis. This automated process eliminates potential errors associated with manual meshing, ensuring uniformity in mesh generation across all models. The precision and efficiency of simulations were enhanced through these computerized tools, allowing for a more focused approach to research objectives and result analysis. The model's specifications, including the size, element order, and minimum element size, were carefully configured to ensure accurate and consistent results throughout the entire process.

3.4.2 Micro-Protrusion's Base Shape Design

The unique geometric characteristics of ellipses make them advantageous in engineering applications, offering benefits such as increased structural efficiency, uniform load distribution, and enhanced stability [144]. Initially, conical models with different ellipse base shapes were created for micro-protrusion designing. Parameter α *(a/b)*, depicted in Fig. 3-3 and ranging from 1 to 6, denotes the variety of the base shapes, as detailed in Table 3-2. The larger the α value, the flattening of the base shape. The base area and height were kept constant in all models. The representative models and the other conditions, such as the load, base area value, and height, are also illustrated in Table 3-2.

Table 3-2 Geometric parameters and loads of models 1-6.

	Model 1	Model 2	Model 3	Model 4	Model 5	Model 6
Geometric models	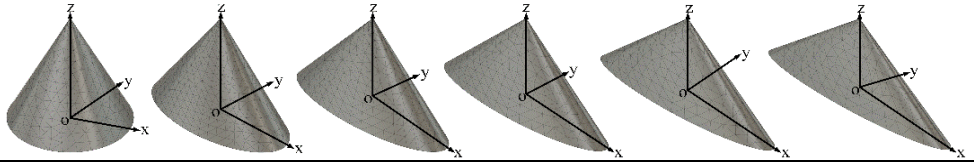					
Base area	$s = \pi ab = 0.785\ mm^2$					
Semi-major axis （a）	0.500 mm	0.708 mm	0.866 mm	1.000 mm	1.118 mm	1.225 mm
Semi-minor axis (b)	0.500 mm	0.354 mm	0.289 mm	0.250 mm	0.224 mm	0.204 mm
$\alpha = a/b$	1	2	3	4	5	6
Height / h	1 mm					
Loads	(x, y, z): (-20N, 0N, 0N); (-20N, 1N, 0N); (-20N, 2N, 0N); (-20N, 5N, 0N); (-20N, 10N, 0N); (-20N, 20N, 0N) The same coordinate orientation with models					

3.4.3 Micro-Protrusion's Apex Position Design

Evolutionarily, the rose thorn's apex was not fixed directly above the central point of the base, and evolution had emerged to enhance its survival. When integrating the rose thorn-inspired micro-protrusion into the realm of metals-CFRP easily disassembled joining, the choice of the apex position becomes pivotal. Deviating the apex away from the base central point contributes to forming an inclined geometric profile, which can modulate the joining interface's angle and the disassembly interface. Moreover, an asymmetric apex position can tailor the geometric configuration of the joining to accommodate specific stress distributions and joining performance requirements. Additionally, an apex oriented strictly vertically upwards may risk interference or entanglement during the joining process. The likelihood of such occurrences can be mitigated by deviating from the apex direction.

Consequently, this section focuses on the micro-protrusion tip position design, also called the length *(l)* design. This design parameter, illustrated in Fig. 3-3, represents the horizontal distance from the thorn's tip to the center of the base. Based on the maximum stress analysis results of the base shape, as introduced in Section 3.5.1, Model 2's base shape was selected for analyzing the apex location in this section. The applied load scenario for this analysis was (-20N, 10N, 0N). Among the models considered, models 7-12 as detailed in Table 3-3, the length *(l)* was related to the semi-major axis *(a)* and varied as $a/3$, $2a/3$, a, $4a/3$, $5a/3$, and $2a$, respectively.

Table 3-3 Models 7-12 for micro-protrusion apex position design.

	Model 7	Model 8	Model 9	Model 10	Model 11	Model 12
Geometric models	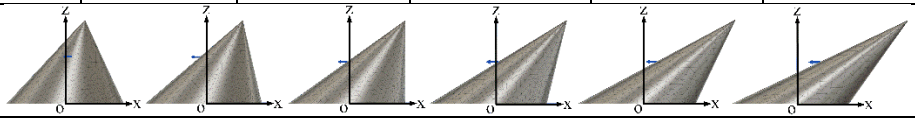					
Base shape	a = 0.708 mm; b = 0.354 mm; α = 2					
Length / l	$\frac{1}{3}$ a	$\frac{2}{3}$ a	a	$\frac{4}{3}$ a	$\frac{5}{3}$ a	2 a
Base area/ s	s = πab = π×0.708×0.354 = 0.785 mm^2					
Height / h	1 mm					
Load	(x, y, z): (-20N,10N,0N)					

3.4.4 Micro-Protrusion’s Profile Curve Design

a) Design of the outer profile curve

In contrast with the inner contour of the micro-protrusion that predominantly encountered loadings and constitutes a vital zone for achieving robust joint, the outer contour plays a critical role in conferring disassembly functionality. To ensure design rationality, particularly in optimizing the inner profile curve to mitigate the maximum stress concentration and optimize the location, the configuration of the outer profile curve needed to be established as a foundational step. Based on the analytical findings in Sections 3.5.1 and 3.5.2, Model 9’s base shape and apex position, as shown in Table 3-3, were selected as the fundamental parameters for the outer contour design in this section.

Integrating the analysis in Section 3.3.2 on easy disassembly, the strategic application of sleek curve profiles offers evident advantages for the outer profile design. Thus, the chosen approach for outer contour design involves the utilization of a refined circular arc profile. From a broader perspective, the pursuit of optimizing the micro-protrusion's compatibility with the CFRP prompted the need to ensure the tip has a horizontal orientation towards the right, as explained in section 3.3.2. Fig. 3-8 illustrates this design methodology and presents a schematic representation of the resultant biomimetic model. Beginning with the linkage of the micro-protrusion's tip and left endpoint, the intersection of the vertical bisector and the extended line originating from the model's right side served as a pivotal reference center point. Subsequently, a curvilinear arc was derived from this reference point, ensuring alignment of the left endpoint and apex along a cohesive curve. This design approach maintained continuity and smoothness and ensured the rightward orientation of the micro-protrusion's apex.

b) Design of the inner profile curve

The inner curved profile of the micro-protrusion enhances its stress dispersion, optimizes load pathways, and increases stiffness. In this section, the conical curve was employed to design the inner profile of the micro-protrusion shape. Compared with other curve shapes, the conical curve offers several advantages, making it a focus of interest in curve design. Firstly, the shape of the conical curve can be precisely defined using only a few parameters: start point, end point, vertex position, and Rho value, represents the sharpness or smoothness of the curve at the vertex, rendering it more manageable in model establishment and parameter adjustment. Secondly, the conical curve can exhibit a wide range of curvature degrees under different parameter values, ranging from straight lines to circular arcs and even parabolas, thus accommodating diverse

simulation requirements for various biological structures. Most importantly, the conical curve demonstrates continuity and smoothness in its curvature distribution, pivotal in reducing stress concentration and optimizing structural performance.

The start and end points are the two ends of the right outline of the micro-protrusion. The vertex position corresponds to the apex of the formed conical curve, essentially indicating the point on the curve that is maximally distant horizontally from both the end point and start point. The vertex position can be adjusted in both the horizontal and vertical directions on the x-z plane. When the vertex position was altered vertically, such as moving it closer to the tip of the rose thorn, the vertex of the formed conical curve also moved closer to the tip of the micro-protrusion, as shown in Fig. 3-9(d). Conversely, when the vertex position was closer to the base, the vertex of the formed conical curve also approached the base, as shown in Fig. 3-9(b). When the vertex position was shifted horizontally, it greatly influenced micro-protrusion volume. As the vertex approached the right side of the model, the vertex of the formed conical curve also moved nearer to the model's right side, which resulted in a bigger micro-protrusion volume, as depicted in Fig. 3-9(a). Conversely, when the vertex was distant from the right side, the vertex of the formed conical curve also resided farther from the right side and led to a smaller volume, as shown in Fig. 3-9(e). In summary, the movement of the conical curve vertex position in any direction can form different conical curve shapes, significantly impacting the maximum stress value and position within the micro-protrusions.

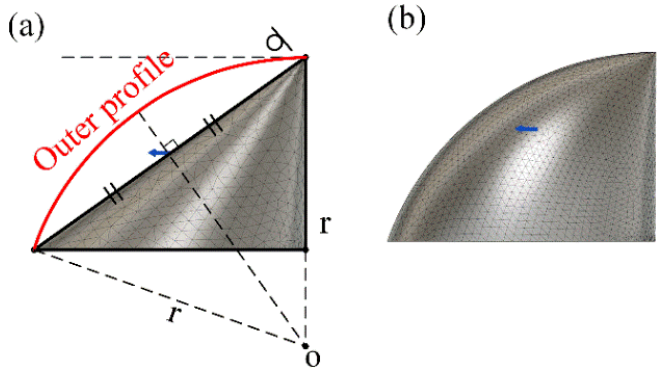

Fig. 3-8 Design of the micro-protrusion outer profile: (a) design methodology; (b) the final model.

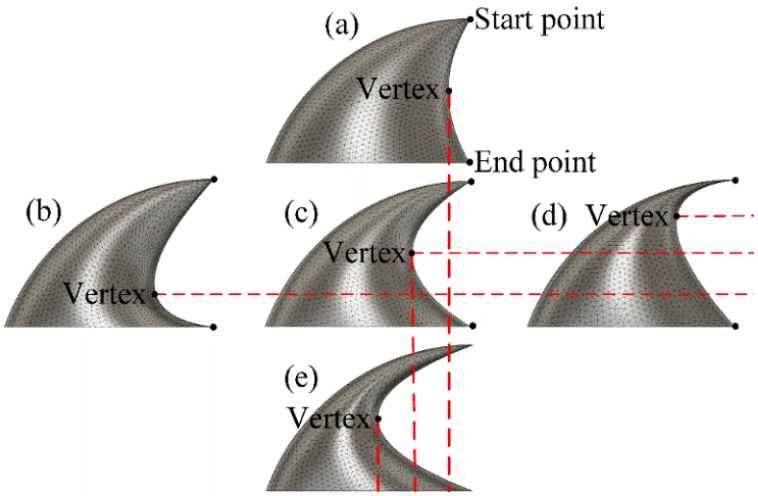

Fig. 3-9 Concial curve vertex position changes of the inner profile: (a) 3D model with the vertex at position 25 in Fig. 3-11; (b) 3D model with the vertex at position 9 in Fig. 3-11; (c) 3D model with the vertex at position 27 in Fig. 3-11; (d) 3D model with the vertex at position 38 in Fig. 3-11; (e) 3D model with the vertex at position 29 in Fig. 3-11.

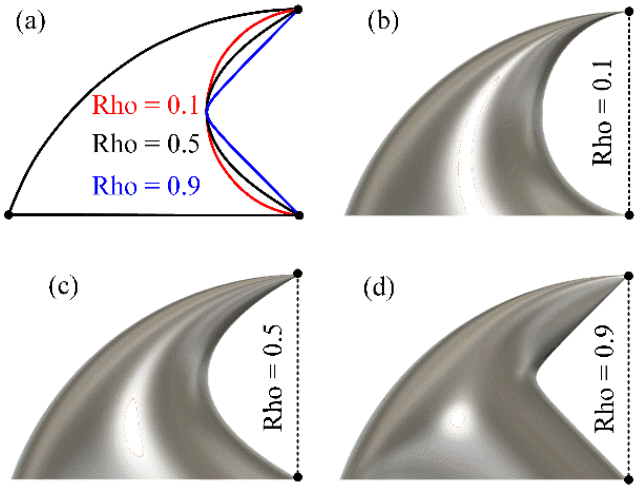

Fig. 3-10 Rho values change of the inner profile: (a) schematic diagram of the inner profile with different Rho values; (b) 3D-model with the Rho = 0.1; (c) 3D-model with the Rho = 0.5; (d) 3D-model with the Rho = 0.9.

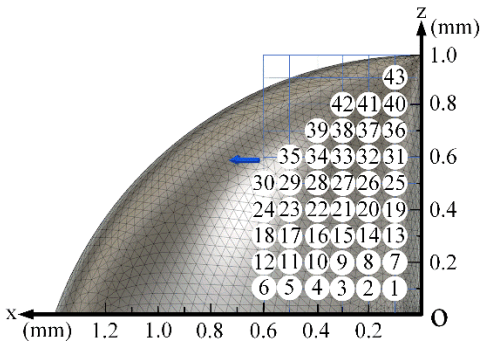

Fig. 3-11 Selected conic curve vertex positions for micro-protrusion inner profile design, 1- 43 positions.

Rho significantly impacts the sharpness of the conical curve at the vertex area of the created inner profile. The vertex positions were kept the same in Fig. 3-10(a), but the different Rho values led to different micro-protrusion shapes. A higher value of Rho resulted in a sharper conical curve at the vertex position, while a lower value generated a smoother curve, as shown in Fig. 3-10(b)-(d). During the modeling process, Rho values exceeding 0.5 were found to often result in modeling failure due to the small volume of the model. Therefore, the subsequent experiments utilized Rho values of 0.1, 0.3, and 0.5.

In the design of the inner profile, a detailed examination of the influence of conical curve vertex positions and Rho values on the maximum stress value and position of the micro-protrusion was carried out. The Rho values were selected as 0.1, 0.3, and 0.5. Additionally, the conical curve vertex positions were systematically determined, as shown in Fig. 3-11, both horizontally and vertically for comprehensive analysis.

3.5 Results and Discussion

According to the numerical simulation results of static stress, this chapter illustrates the influence of each geometrical parameter on the maximum stress location and values of the micro-protrusion. The priority objective is to engineer a rose thorn biomimetic micro-protrusion geometry shape that is resilient against stress concentration, ensuring robust bonding with metal matrix and mitigating the risk of mechanical failure at the apex. By systematically mitigating stress concentration at these critical junctions, the designed structure can be expected to meet the necessary mechanical requirements for reliable performance and longevity.

3.5.1 Influence of Base Shape

a) Maximum stress analysis under the x-uniaxial load

When subjected to the uniaxial force (-20N,0N,0N), the entire micro-protrusion experienced a negative x-axis load. Under uniaxial loading, across models 1 through 6, the maximum stress locations and values are depicted in Fig. 3-12 to Fig. 3-17. In Model 1, the maximum stress was 118.8 MPa, manifesting at the edge of the micro-protrusion base. Model 2 shows a peak stress of 73.5 MPa, the same position at the base edge. For Model 3, the highest stress reaches 65.0 MPa, localized at the midsection of the inner profile of the micro-protrusion structure. Similarly, Models 4, 5, and 6 also exhibited their highest stresses at the midsection area with corresponding values of 59.2 MPa, 56.6 MPa, and 53.6 MPa, respectively. Analyzing the maximum stress within these

models under a load of (-20N, 0N, 0N) revealed a decreasing trend in maximum stress values as the α, representing the base shape, increases. And the shift in the location of maximum stress changed from the base towards the midsection.

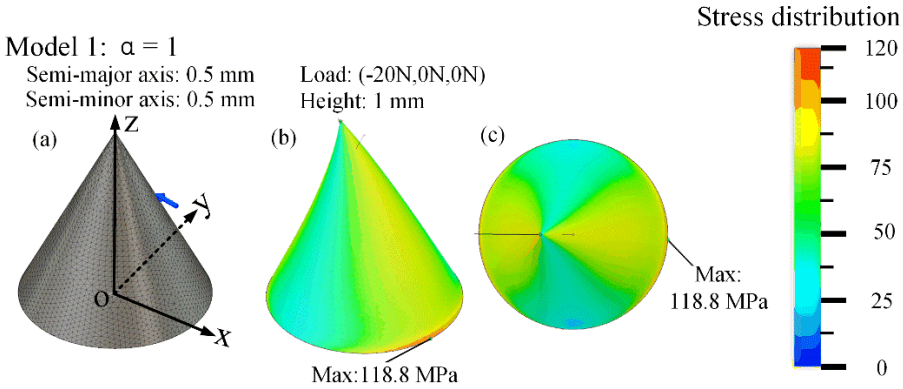

Fig. 3-12 Stress distribution of Model 1: (a) original model; (b) 3D view of the stress-strain simulation results; (c) top view of the stress-strain simulation results.

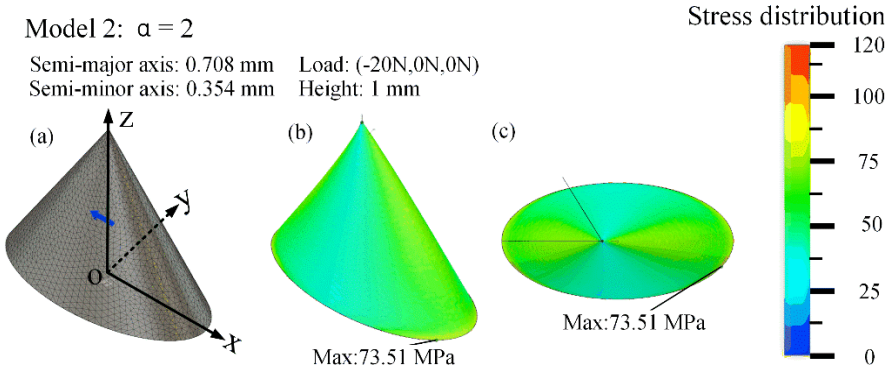

Fig. 3-13 Stress distribution of Model 2: (a) original model; (b) 3D view of the stress-strain simulation results; (c) top view of the stress-strain simulation results.

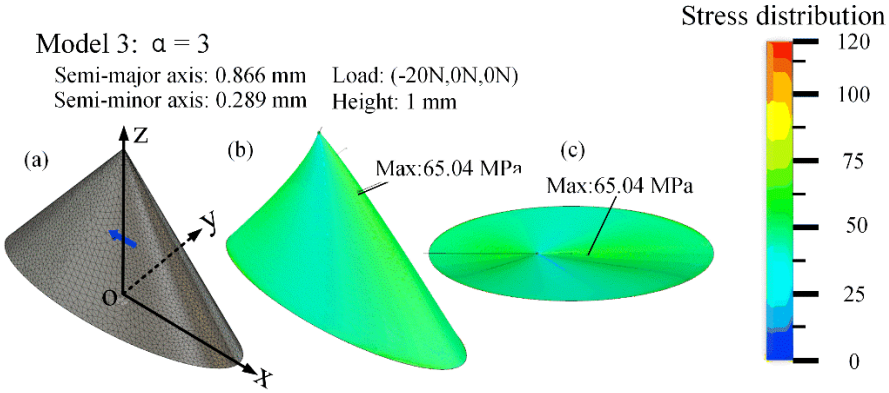

Fig. 3-14 Stress distribution of Model 3: (a) original model; (b) 3D view of the stress-strain simulation results; (c) top view of the stress-strain simulation results.

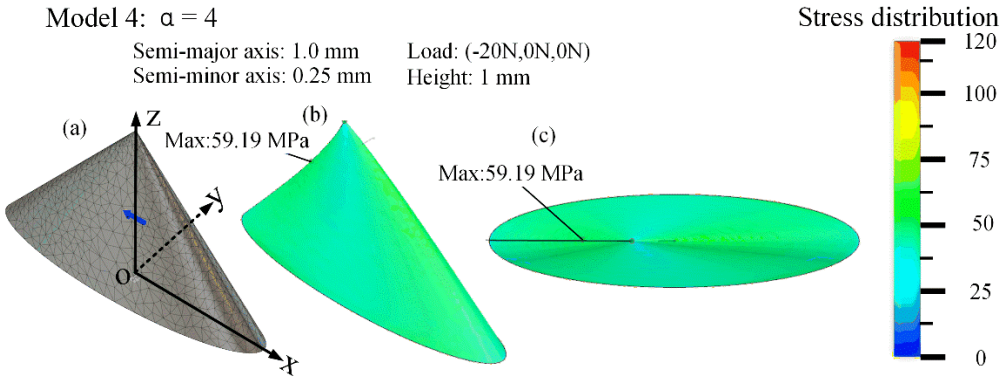

Fig. 3-15 Stress distribution of Model 4: (a) original model; (b) 3D view of the stress-strain simulation results; (c) top view of the stress-strain simulation results.

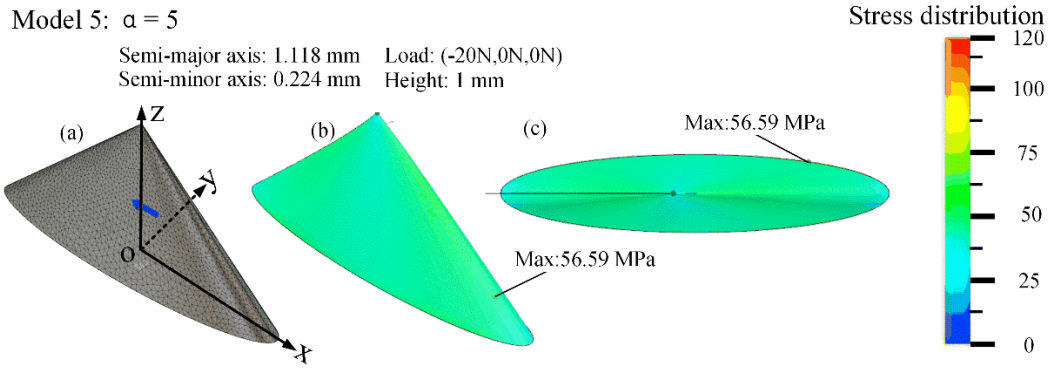

Fig. 3-16 Stress distribution of Model 5: (a) original model; (b) 3D view of the stress-strain simulation results; (c) top view of the stress-strain simulation results.

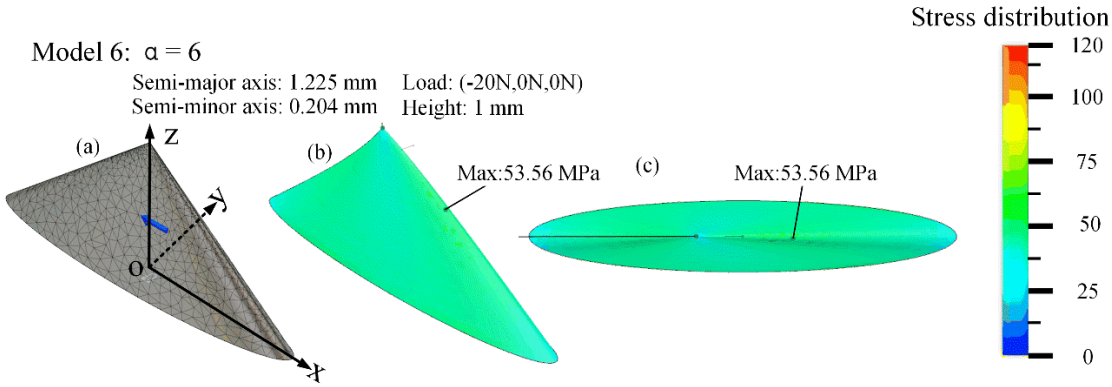

Fig. 3-17 Stress distribution of Model 6: (a) original model; (b) 3D view of the stress-strain simulation results; (c) top view of the stress-strain simulation results.

Within the examined models 1 to 6, each horizontal section of the micro-protrusion resembles the base's shape. In model 1, the circular base generated a uniform stress distribution due to its symmetry, resulting in even stress distribution around the circular edge, which is farthest from the base center. Conversely, models 3 to 6 adopted an elliptical base, and the asymmetry of the ellipse

induced a more dispersed stress distribution, consequently reducing stress concentration along a single direction. Moreover, stiffness varies along the major and minor axes in an elliptical structure due to differing geometric properties and cross-sectional areas. Generally, the longer axis exhibits higher stiffness and more excellent resistance to external forces due to its considerable length and cross-sectional area. Hence, from model 1 to model 6, an increase in the length of the major axis corresponded to a decreasing trend in maximum stress values for the micro-protrusion subjected to a singular x-axis load.

Additionally, alterations of the base shape affected the form of each horizontal cross-section of models along the z-axis. Thus, when the base took an elliptical form, stress distribution along each horizontal cross-section became non-uniform, causing stress behaviors to shift away from the base's edge to the midsection of the micro-protrusion. In summary, the base shape variation directly impacted the micro-protrusion models' maximum stress value and location. Elliptical base shapes introduced asymmetry and non-uniform stress distribution, leading to the relocation of the maximum stress from the base's edge to the model's midsection.

b) Maximum stress analysis under x-y biaxial load

After introducing the load applied along the y-axis, Fig. 3-18 illustrates the maximum stress values under various loading conditions for different models. Unlike the uniaxial x-load condition, the variation trend of maximum stress values under the x-y biaxial loading conditions exhibits more complexity. For instance, under the (-20N,1N,0N) load, models 1-6 continue to show a decreasing trend in maximum stress values, similar to what was observed under the previous (-20N,0N,0N) load. However, when the y-axis load was increased to 2 N (-20N,2N,0N load), models 1-5 still showed a decreasing pattern, but the maximum stress value in model 6 slightly increased, surpassing that of model 5.

With a y-axis load of 5 N, models 1-5 continued to exhibit decreasing maximum stress values, while a significant increase was observed in the maximum stress value of model 6, surpassing that of model 3. When the y-axis load reached (-20N,10N,0N), the maximum stress values in models 1-6 displayed a more intricate variation trend, with model 2 showing the lowest maximum stress value. Finally, as the y-axis load increased to (-20N,20N,0N), the maximum stress values in models 1-6 progressively rise.

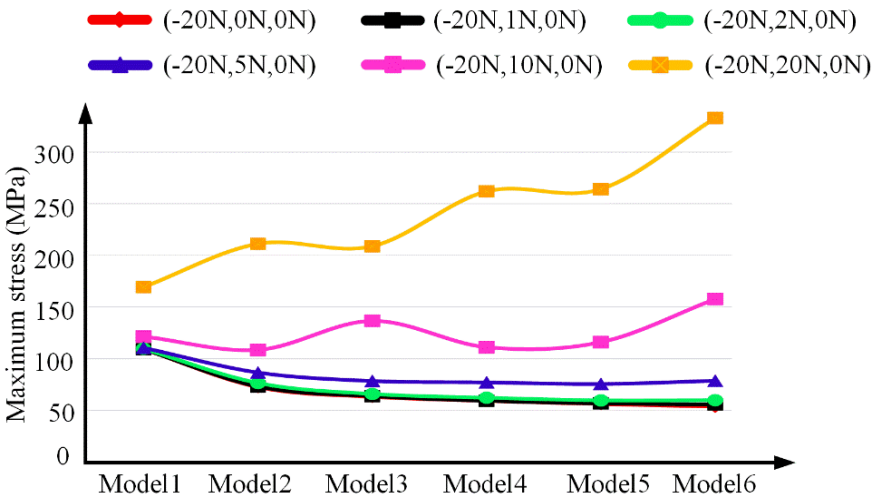

Fig. 3-18 Maximum stress values of models 1-6 under x-y biaxial different loads.

Regarding the location of maximum stress occurrence, in model 1, maximum stress consistently appeared at the base edge under all loading conditions. This is primarily due to the symmetry of the circular base shape, resulting in a uniform distribution of applied forces and the emergence of maximum stress values at the farthest edge from the base center. However, in models 2-6, due to the non-uniformity of the elliptical shape, maximum stress values were distributed at both the base edge and the waist area.

The intricate variation trends observed in Fig. 3-18 can be explained by considering the interaction between the geometric characteristics of the models and the applied loading conditions. When the y-axis load was introduced, the resultant force direction changed with variations in the y-axis load. Therefore, the most extended length along the resultant force direction within the base shape was measured for each of the six models, as illustrated in Fig. 3-19(a) and presented in Fig. 3-19(b). In model 1, with a regular circular base, the longest length remained constant at 1 mm for different loads. However, for models 2 to 6, which have ellipses with varying aspect ratios as their base shapes, the longest length gradually decreased with changes in the loads (-20N,0N,0N), (-20N,1N,0N), (-20N,2N,0N), (-20N,5N,0N), (-20N,10N,0N), and (-20N,20N,0N).

Fig. 3-19 shows that the arrangement of the longest length along the resultant force direction within the base changed as the load varied among the six models. When comparing the longest length of the six models under each load with the corresponding maximum stress values generated under the same load, an approximately inverse relationship between the length along the resultant force direction and the maximum stress value can be observed.

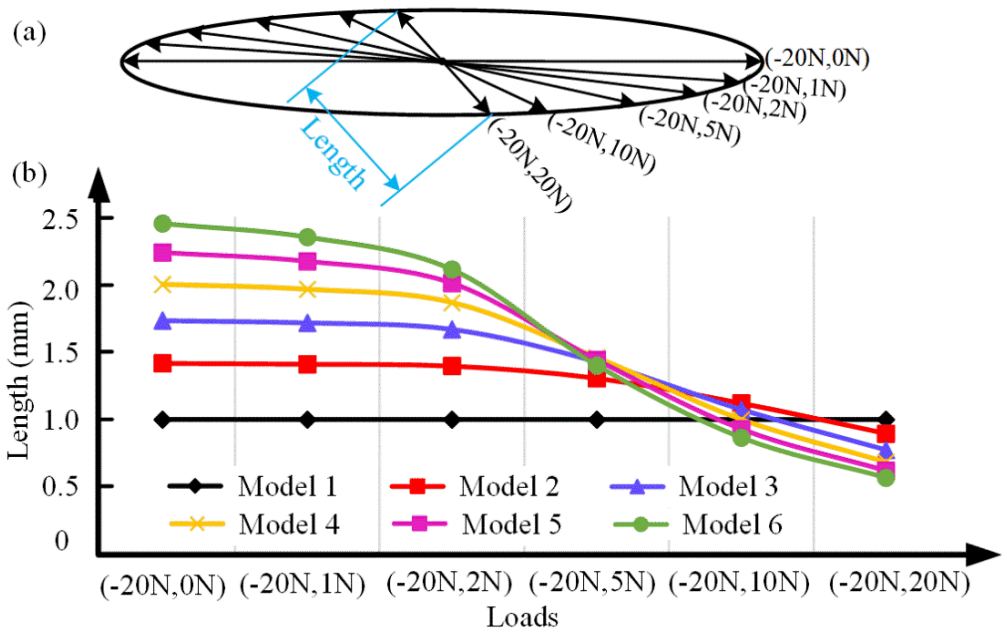

Fig. 3-19 Longest length along the resultant force direction within the base shape: (a) schematic of the longest length along the resultant force direction; (b) values of the longest length.

For the loads (-20N,0N,0N), (-20N,1N,0N), and (-20N,2N,0N), the arrangement of the longest length from models 1-6 was as follows: model 6 > model 5 > model 4 > model 3 > model 2 > model 1, while the arrangement of the maximum stress values under this load was essentially: model 1 > model 2 > model 3 > model 4 > model 5 > model 6. This indicated that as the length within the base along the resultant force direction increased, the resultant stress value gradually decreased.

Under the load (-20N,5N,0N), model 5 exhibited the longest length along this resultant load. With the load (-20N,10N,0N), model 2 had the maximum length along the resultant force direction within its elliptical base, resulting in the smallest maximum stress value. Conversely, under the load (-20N,20N,0N), the lengths along the resultant force direction within the base of all six models gradually decreased, subsequently causing the corresponding maximum stress values to increase progressively.

The findings from the above observations can be summarized by considering stiffness as a critical perspective, elucidated by the equation (3-1):

$$k = \frac{E}{3(1-2\sigma)} \tag{3-1}$$

Where k symbolizes the material's stiffness, E represents the material's elastic modulus, and σ signifies the Poisson's ratio. It becomes apparent from this equation that, under a consistent material composition, stiffness shares a direct proportionality with the elastic modulus.

Furthermore, the elastic modulus E can be mathematically represented by Equation (3-2):

$$E = \frac{\sigma}{\epsilon} = \frac{\sigma}{\delta/L} = \frac{L \cdot \sigma}{\delta} \tag{3-2}$$

In this equation, L corresponds to the length of the base geometry in the direction of the applied force, δ characterizes deformation, and σ denotes stress.

This equation clearly illustrates that the elastic modulus maintains a direct relationship with L, underscoring that the stiffness of a material is intimately linked to its length in the resultant force direction. Consequently, as the length along the force direction increased, the model's stiffness intensified, thereby augmenting its ability to resist deformation. This progression subsequently led to a reduction in the magnitude of the maximum stress value. Therefore, when determining the base shape for the rose thorn biomimetic structure, it is imperative to initially scrutinize its specific force distribution and subsequently judiciously amplify its length along the force direction.

3.5.2 Influence of Apex Position

Fig. 3-20 to Fig. 3-25 depict the locations and magnitudes of the maximum stress generated in models 7 to 12 under the load condition (-20N,10N,0N). Firstly, across models 7 to 12, the positions where the maximum stress values occur were consistently situated at the bottom of the right side of the models. Notably, model 7 exhibited the smallest maximum stress value at 158.1 MPa. As the tip of the model gradually shifts from left to right, a trend of increasing maximum stress values was observed in models 8 to 11. In model 11, the maximum stress value peaked at 720.1 MPa. Subsequently, as the apex of the model continues to move rightward, a slight decrease in the maximum stress value was observed in model 12, with a value of 589.3 MPa.

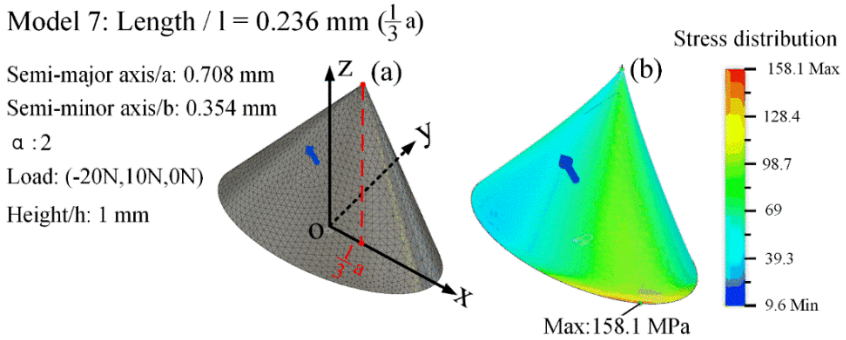

Fig. 3-20 Stress distribution of Model 7: (a) original model; (b) 3D view of the stress-strain simulation results.

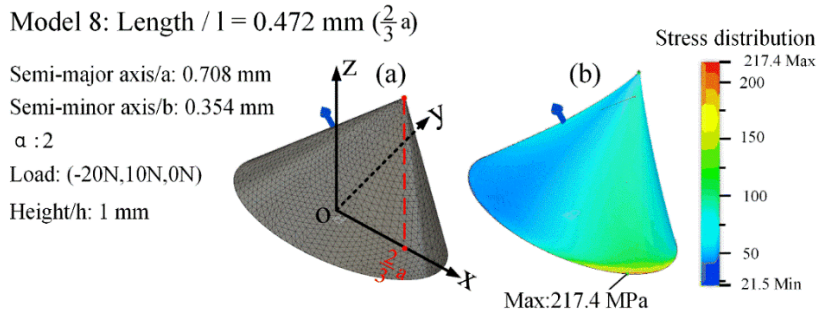

Fig. 3-21 Stress distribution of Model 8: (a) original model; (b) 3D view of the stress-strain simulation results.

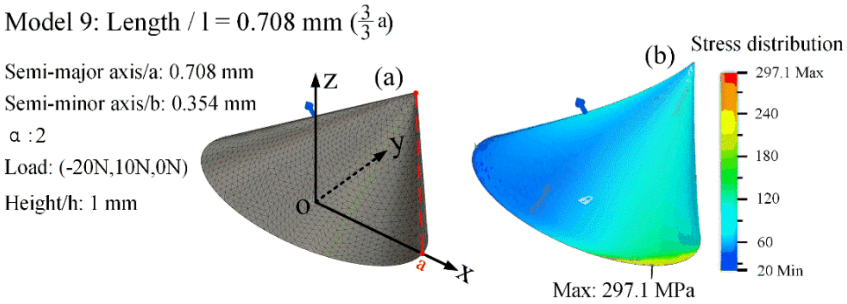

Fig. 3-22 Stress distribution of Model 9: (a) original model; (b) 3D view of the stress-strain simulation results.

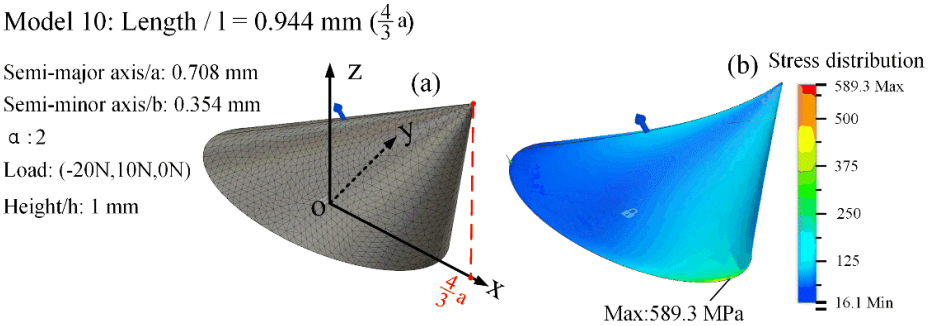

Fig. 3-23 Stress distribution of Model 10: (a) original model; (b) 3D view of the stress-strain simulation results.

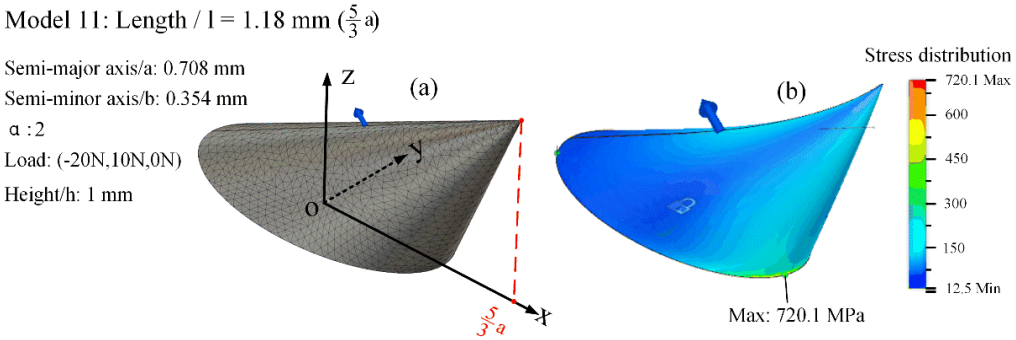

Fig. 3-24 Stress distribution of Model 11: (a) original model; (b) 3D view of the stress-strain simulation results.

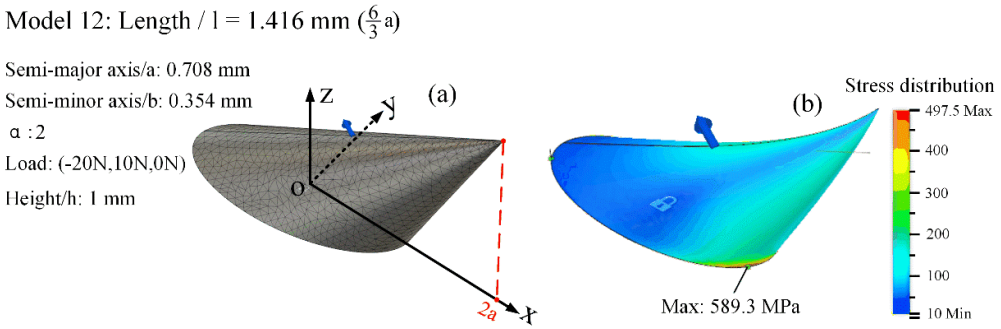

Fig. 3-25 Stress distribution of Model 12: (a) original model; (b) 3D view of the stress-strain simulation results.

Based on the simulation results and subsequent analysis, we observed a trend of increasing maximum stress values when the apex deviates from being directly above the base center. This is due to the micro-protrusion apex gradually shifting from left to right, increasing structural asymmetry, and sharpening the angle at the junction between the model's right side and the base. However, achieving enhanced joint strength and easy disassembly are essential goals for rose thorn-inspired protrusions, which require intentionally displacing the tip from the base center. In model 9, the apex aligns directly above the right endpoint of the base, ensuring more effective joining with the CFRP while avoiding excessive asymmetry in the model's shape. Consequently, we selected model 9 parameters as the basis for further analysis, highlighting the importance of meticulous design in optimizing the side profile of the rose thorn biomimetic protrusion.

3.5.3 Influence of Profile Curves

a) Influence of outer profile

In Section 3.4.4 a), the initial design of the outer contour curve of the micro-protrusion was carried out, and the resulting stress distribution under equivalent load was depicted in Fig. 3-26. With this micro-protrusion shape, the maximum stress was found at the base edge, aligning with model 9, and the value exhibited improvement. This indicated that the changes in the outer contour shape have resulted in variations in the stress distribution of the rose thorn, emphasizing the necessity of designing the inner-sides shape.

b) Influence of inner profile

After establishing the fixed outer profile curve of the micro-protrusion, attention turned to the design of the inner profile curve. As outlined in Section 3.4.4 b), a series of studies were conducted to assess the impact of distinct vertex positions and Rho values within the context of the conic curve on the micro protrusions' maximum stress values and positions. The influence of Rho values and vertex positions of the conic curve on the micro-protrusion primarily manifests in two critical

aspects: the location and the value of the maximum stress. Regarding the generation location of the maximum stress, it can typically be categorized into three areas: the base edge of the micro-protrusion, the apex area, and the vicinity of the conic curve vertex.

Fig. 3-27 illustrates a scenario where the maximum stress was located at the base edge, with a Rho value of 0.5 and vertex coordinates of the conic curve set at x = 0.3 mm, z = 0.5 mm, position 27 in Fig. 3-11. Compared to Fig. 3-26, it can be observed that the maximum stress value decreased. This implies that the design of the inner profile can significantly impact stress distribution. This situation often occurred when the vertex was positioned at a higher location and closer to the right edge of the micro-protrusion. Under these conditions, a smooth transition zone occurred at the higher position, while a less noticeable curvature resembled characteristics closer to a straight line at the base edge. In this case, the maximum stress location resembled the stress distribution observed in model 9.

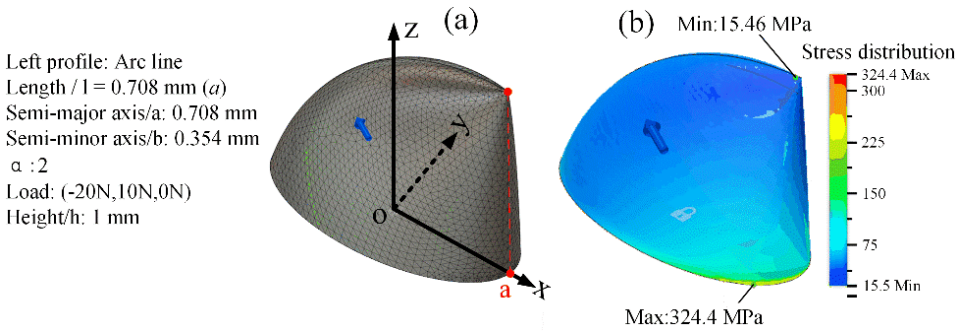

Fig. 3-26 Stress distribution with the designed outer profile curve: (a) original model; (b) 3D view of the stress-strain simulation results.

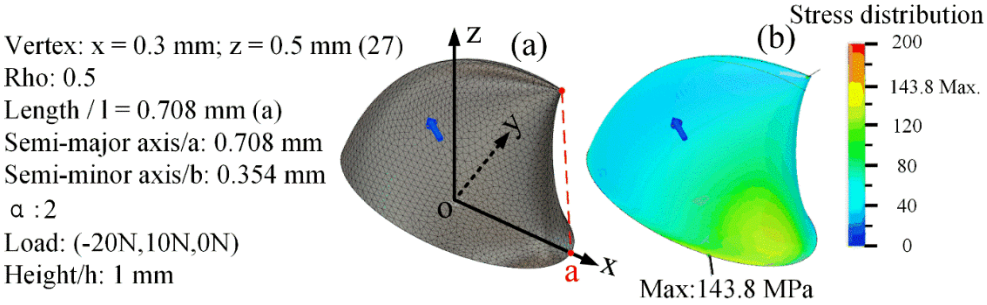

Fig. 3-27 Maximum stress occurred at the base edge: (a) original model; (b) 3D view of the stress-strain simulation results.

Fig. 3-28 illustrates a scenario where the maximum stress was observed near the apex. The associated coordinates of the conic curve's vertex were x = 0.4 mm and z = 0.2 mm, specifically at position 10 in Fig. 3-11, with a Rho value of 0.1. Based on the analysis in Fig. 3-27, it is confirmed that when the conic vertex position exceeded 0.5 mm, the maximum stress occurred at the base edge. However, this does not imply that other vertex positions lower than z = 0.5 mm in Fig. 3-11 would yield an ideal micro-protrusion. When the x-coordinate of the vertex exceeded 0.3 mm, it led to a reduction in the micro-protrusion's volume, as explained in Fig. 3-9(a)(c)(e). Notably, as the conic curve's vertex moved upward along the z-axis, approaching the tip of the model, it further reduced the overall dimensions. Consequently, it caused the maximum stress value to appear at the tip.

In the final scenario, the maximum stress of the micro-protrusion was located near the conic curve vertex zone, with a corresponding curve's Rho value of 0.3, as depicted in Fig. 3-29. The vertex coordinates were set at x = 0.3 mm and z = 0.3 mm, specifically at position 15 in Fig. 3-11. As the vertex position decreased, the junction area at the right corner of the base exhibited a smoother characteristic rather than forming a nearly 90° right angle. Consequently, the maximum stress value of the micro-protrusion began to move upward, approaching the vertical height of the conic curve's vertex zone.

Based on the analysis above, the selection of the vertex position of the conical curve can be divided into three Regions according to the location of the stress concentration, and the result is shown in Fig. 3-30. If the vertex position of the conical curve was chosen in Region 1, the final stress concentration occurred at the bottom edge of the micro-protrusion. If the vertex position of the conical curve was selected in Region 2, the corresponding stress concentration happened in the apex area of the micro-protrusion. If the vertex of the conical curve were chosen in Region 3, the related stress concentration would occur in the vicinity of the vertex of the conical curve.

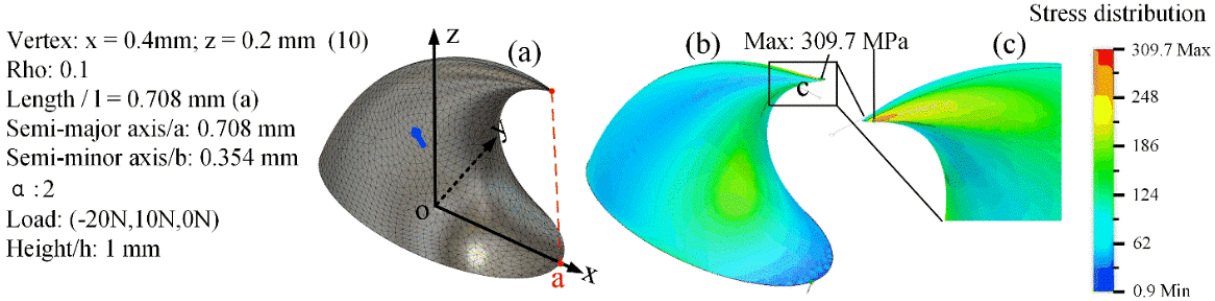

Fig. 3-28 Maximum stress occurred at the apex zone: (a) original model; (b) 3D view of the stress-strain simulation results; (c) magnification of the apex zone.

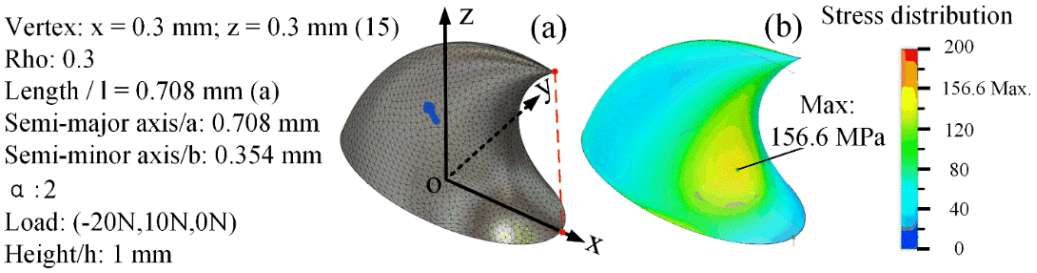

Fig. 3-29 Maximum stress occurred near the conic curve vertex zone: (a) original model; (b) 3D view of the stress-strain simulation results.

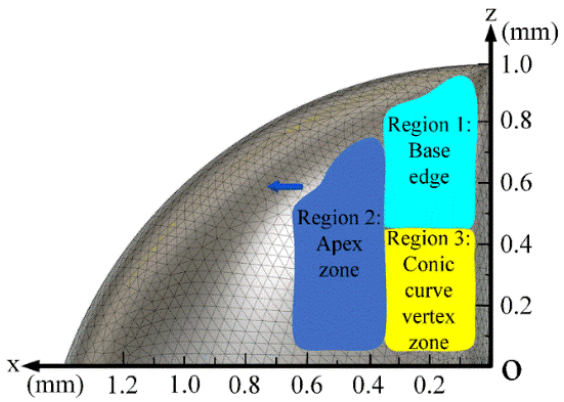

Fig. 3-30 The relationship between the selection of the conical curve vertex position and the related stress concentration location of the micro-protrusion, refer to Fig. 3-11.

3.6 Proposed Micro-Protrusion Shape for Metals-CFRP Easy Disassembly Joining

Considering the need to implement micro-protrusion fabrication on the metal substrate surface in the ongoing research, it is essential to avert stress concentration at the base of the micro-protrusion. This stress concentration could result in weak connections between the micro-protrusions and the metal surface, potentially leading to the failure of the metal and CFRP bonding [145, 146]. Furthermore, the diminutive geometry of the micro-protrusion's apex requires deliberate precaution. The apex's limited volume and load-bearing capacity necessitates a concerted effort to preclude stress concentration in this domain. This preemptive measure is essential to maintain the micro-protrusion's structural integrity and functional efficacy. Thus, the imperative lies in avoiding and reducing stress accumulation in the base edge and tip near the zone to mitigate structural vulnerabilities. Therefore, Optimal positioning of the vertex for the conical curve in the inner profile design is recommended within Region 3, as illustrated in Fig. 3-30.

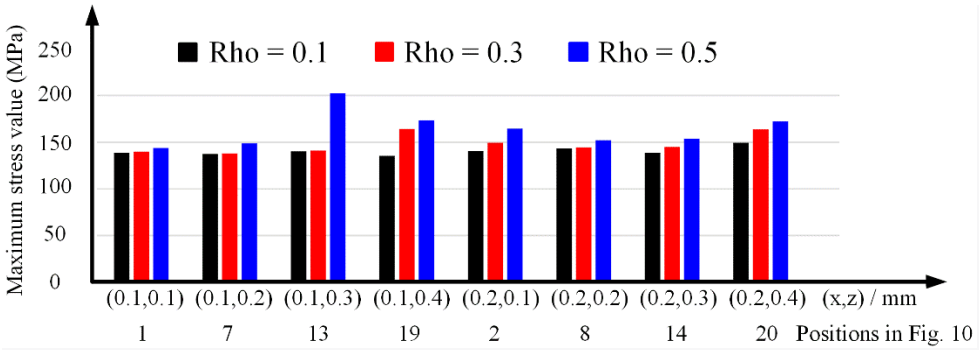

Fig. 3-31 The maximum stress values under different vertex positions and Rho values.

In Region 3 of Fig. 3-30, stress concentration can be prevented from occurring at both the base edge and the apex zone. However, different values of Rho and corresponding apex positions result in varying maximum stress values. Fig. 3-31 displays the outcomes of the maximum stress values for different vertex positions and Rho values. It is evident that, across all apex positions, the model with Rho = 0.1 consistently exhibits the smallest maximum stress values, while the model with Rho = 0.5 consistently yields the most significant maximum stress values. Calculating the standard deviation of these maximum stress values for the three Rho values, it can be found that when Rho = 0.1, the standard deviation of the maximum stress values was 4.3; when Rho = 0.31, it was 10.4; and when Rho = 0.5, it was 19. This indicates that the model with Rho = 0.1 produces relatively uniform maximum stress values.

This section explores the impact of Rho values and the positions of conic curve vertices on both the maximum stress value and micro-protrusions' location. The analysis of various combinations of Rho values and conic curve vertex positions showed that placing the conical curve vertex in Region 3 effectively avoids stress concentration at the base edge and the apex zone, thereby mitigating the fracture risk. Specifically, when the Rho value is set to 0.1, the smooth contour profile on the left side of the micro-protrusion promotes load dispersion, further reducing stress concentration at the base edge and the apex zone and mitigating the risk of fracture.

3.7 Conclusions

This chapter draws inspiration from the structural characteristics and functionalities of rose thorns in nature. This research applies the rose thorn biomimetic micro-protrusions to the metal surface and explores its utility and shape design in joining metals with CFRP. Key findings of this study include:

1、successfully establishing a geometrical model for the biomimetic micro-projections inspired by rose thorns. Precise control of the micro-protrusion shape can be achieved through the raised parameters, offering a novel design approach for connecting metals with CFRP.

2、The bottom shape of the micro-protrusions directly influences the distribution of maximum stress values. When designing the bottom surface shape, considering the structural operating environment and elongating the bottom surface length to increase structural rigidity are essential strategies to reduce stress concentration.

3、Shifting the micro-protrusion apex position can increase the maximum stress values. However, controlled vertex displacement can be employed to facilitate disassembly and optimize the side contour to minimize stress concentration.

4、The position of the vertex of the conic curve and the Rho value affect the shape of the inner profile of the micro-protrusion. Conical curve vertex position can influence the stress concentration in the happened area. Meanwhile, smaller Rho values, such as 0.1, promote smoother contours, dispersing loads and reducing stress concentration. Conversely, larger Rho values, like 0.5, lead to sharper contours, potentially increasing stress concentration and compromising structural stability.

5、Analysis of stress distribution under load conditions for the biomimetic micro-protrusion revealed that appropriate micro-protrusion shape design significantly reduces maximum stress values and optimizes their locations, ultimately enhancing connection strength and reliability.

Simultaneously, this study has certain limitations. For instance, the consideration of the service environment for rose thorns does not encompass all possible scenarios. Additionally, the applicability of the final structure requires further validation through feedback from subsequent manufacturing and joining processes.

Chapter 4: Manufacture of Rose Thorn Biomimetic Micro-Protrusions via Fused Deposition Modeling Method

In this chapter, we delved into the practical realization of the rose thorn-inspired micro-protrusions that were determined in Chapter 3. The cutting-edge technique of Fused Deposition Modeling (FDM) is employed to manufacture the structures on the SPCC surface. The manufacturing process unfolds across various stages, encompassing modeling, debinding, and sintering at different temperatures and times. Through the lens of FDM, this chapter not only realizes the complex bio-inspired structures' manufacturing but also provides insights into the intricate processes essential for post-heat treatment of the resulting products.

4.1 Introduction

This chapter extensively investigated multiple critical aspects of rose-thorn-inspired micro-protrusions manufacturing processes through the FDM method. The FDM process commences with the polymer melting in the printing nozzle at a temperature slightly above its melting point, typically around 230 ℃, followed by precise layer-by-layer deposition onto the printer hotbed under computer control. The deposited layers seamlessly fuse with the underlying ones, resulting in a cohesive structure. This initial 3D-printed model, commonly called the "green part", does not represent the final state of the metal components. This is attributed to the presence of a polymer matrix containing metal components within the green part. Furthermore, the green part fails to meet the performance requirements to fully realize metal products. To achieve authentic metal components, it is imperative to undergo the subsequent steps, namely debinding and sintering. These essential processes play a pivotal role in removing the binder components and enhancing the material's performance characteristics to meet the stringent demands of metal applications. A comprehensive illustration of the entire FDM processes and the responding microstructure composition can be found in Fig. 4-1.

In this chapter, we first experimented with the influencing factors during the modeling process to comprehensively understand their potential impact on product performance, such as forming accuracy and macro defects. Subsequently, our focus shifted to studying the variation of post-heat temperatures and holding time during the sintering process to explore their effects on the final metal.

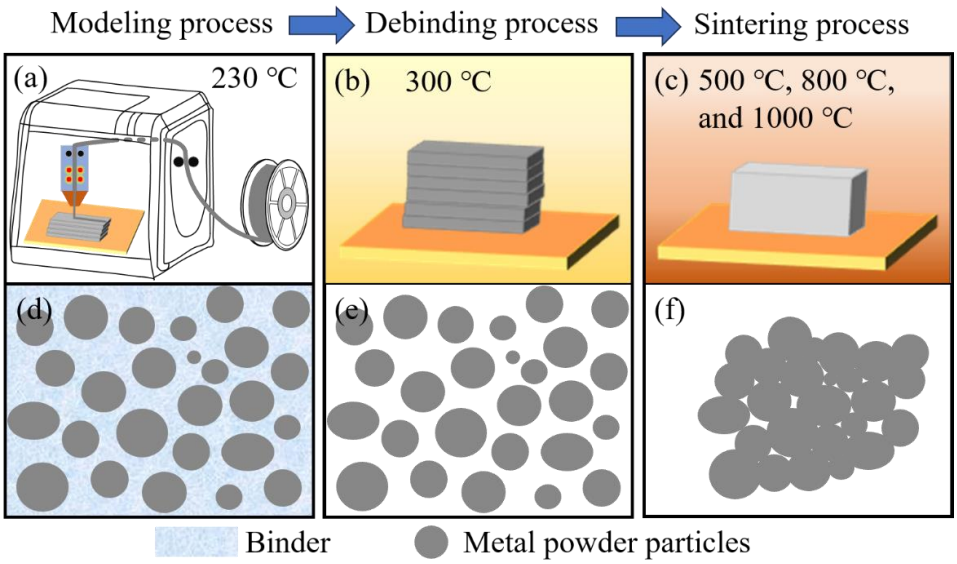

Fig. 4-1 Schematic diagram of the FDM processes.

This involves a systematic investigation of the microstructure and mechanical properties during the sintering process to unveil the product properties under different process conditions. Through this series of studies, we successfully fabricated rose thorn biomimetic structures on the metal surface, laying the foundation for future development in the easy disassembly joining between metals and CFRP.

4.2 Experimental Material and Equipment

4.2.1 Materials

The ultrafuse 316L filament, as shown in Fig. 4-2, an innovative metal-polymer composite feedstock filament developed by BASF company, Japan, redefines the landscape of additive manufacturing within the realm of FDM 3D printers, specifically to produce rose thorn-shaped protrusions in this research. This filament possesses outstanding 316L stainless steel particles with weight content surpassing 80%, and this filament demonstrates compatibility with 1.75 mm diameter open-source FDM printers [147]. The polymer blend, incorporating polyformaldehyde and additives such as polypropylene, enhances fluidity and thermo-stability [147]. Noteworthy is the filament's melt flow rate of 23.56 g per 10 mins at 230 °C, ensuring a seamless printing process [148]. The distinctive attributes of this filament have positioned it as a focal point in ongoing research endeavors, particularly in the context of low-cost additive manufacturing equipment.

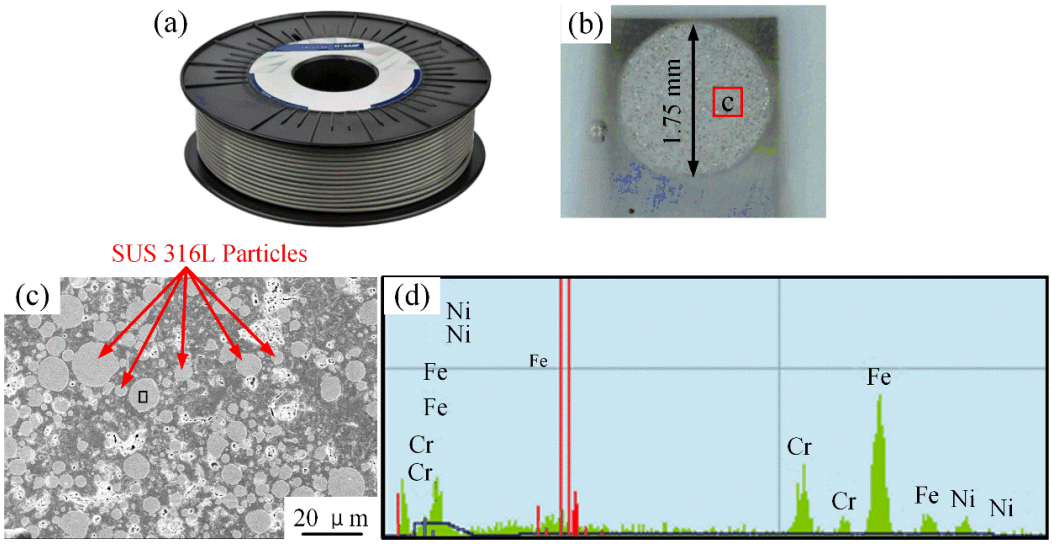

Fig. 4-2 Ultrafuse 316L filament: (a) filament scroll; (b) filament cross section and diameter; (c) filament microstructure; (d) elements composition.

4.2.2 FDM Equipment

In this study, we utilized Adventure 3 series FDM equipment provided by APPLE TRESS company, Japan, for the 3D printing process, as shown in Fig. 4-3. This cutting-edge equipment offers precise control over the additive manufacturing process, ensuring the high-quality fabrication of complex rose thorn-shaped structures. To translate our design concepts into tangible models, we relied on FLASHFORGE software for the slicing and printing of the rose thorn models. FLASHFORGE's intuitive interface and robust features facilitated the seamless translation of digital designs into physical prototypes, enabling us to explore the intricate details of our envisioned structures with ease and precision.

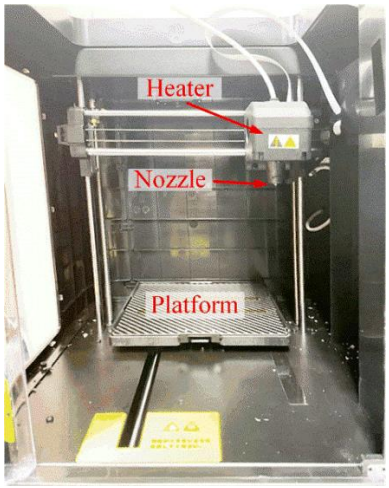

Fig. 4-3 FDM equipment.

4.2.3 Furnace

A crucial step in the thermal processing of FDM printed products involves the use of a high-performance furnace. Specifically, the FT-101M lab furnace from Full-Tech, Japan, was employed for thermal debinding and sintering processes. Operating within a controlled Nitrogen atmosphere with 2 L / min throughout the entire process, the furnace enables oxidation prevention and precise thermal treatments to enhance the quality of the final metal part.

4.2.4 Scanning Electron Microscope (SEM)

The SEM instrument was extensively utilized in experiments to observe the microstructure of object surfaces and microstructures. During the FDM process, SEM provided high-resolution images, revealing the deposition status of the filament at different stages. This aided in understanding the hierarchical structure, surface roughness, and potential defects.

4.3 Modeling Phase

4.3.1 Preliminary Modeling Results

During the FDM process, the modeling stage is a critical step, where various factors come into play, directly influencing the quality and performance of the final part. In this section, meticulous attention was dedicated to the Green Parts fabrication, and precision and macroscopic defects are considered two fundamental criteria and the most intuitive standards for evaluating the products produced in this process. The following parameters in Table 4-1 were printed preliminary to explore the potentiality of the printing process. The results are presented in Fig. 4-4, which were printed under the conditions of ambient platform temperature and a layer thickness of 100 micrometers. It is evident that when the model's height was 1 mm, the forming results were entirely unsuccessful, similarly observed at a height of 2 mm. Subsequently, the model was uniformly scaled to three times its original dimensions. With the continuous amplification, the forming process of the model exhibits notable improvements, particularly in the waist region. However, due to the smaller dimensions at the top of the micro-protrusion, the forming remained suboptimal in smaller sections. Following this, when the model was uniformly scaled four times, corresponding to a height of 4 mm, a significant enhancement in the forming of the top section of the micro-protrusion was observed, although the result was not yet optimal. Upon reaching a scaling factor of 5, the forming result entirely replicated the geometric shape of the designed model, as shown in Fig. 4-4(b).

Table 4-1 Printing parameters used in FDM.

Printing parameters	**Values**
Filament material	Ultrafuse SUS 316L
Nozzle diameter	400 μm
Nozzle temperature	230 ºC
Platform temperature	Room temperature
Layer thickness	100 μm
Printing speed	40 mm/s
Infill density	100%

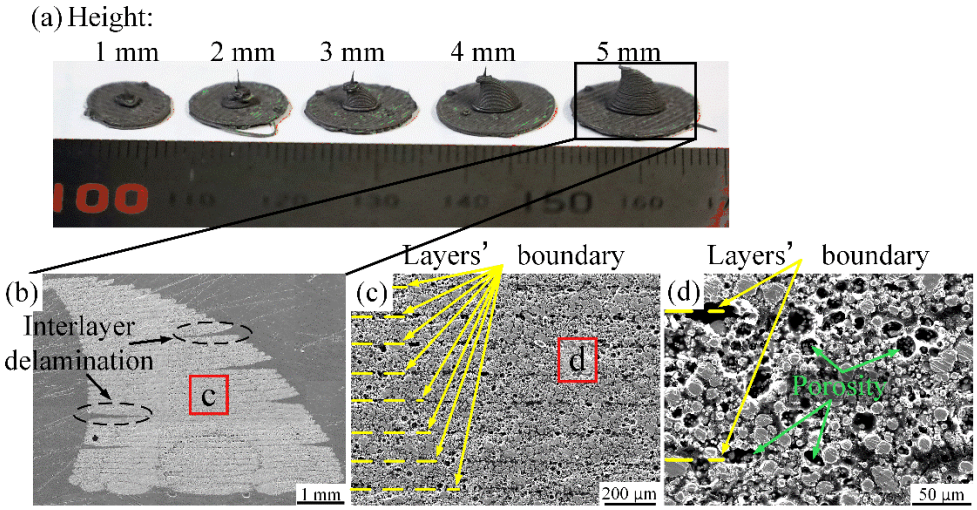

Fig. 4-4 Modeling results of the Green Part with room temperature platform and 100 μm layer thickness: (a) forming results with different scale under optical camera; (b) vertical section of the protrusion with 5 mm height; (c) layers' boundary; (d) porosity defects.

This indicates that smaller-sized sections experienced a more substantial impact, and with the increase in scale, the shape's performance gradually stabilized. The findings highlight the critical role of dimension adjustments in FDM modeling, particularly in achieving high precision and mitigating macroscopic defects. However, it is important to highlight that a structure with a height of 5 mm deviated significantly from the designed model scale in Chapter 3. Therefore, corresponding optimization should be undertaken to enhance precision and minimize structural scale.

In addition to the macroscopic forming precision, another prominent defect observed in structures printed under ambient room temperature conditions on the platform was interlayer delamination, as illustrated in Fig. 4-4(b). Interlayer delamination can weaken the product's

structural integrity, thereby affecting its mechanical properties and the joint performance in the subsequent joining process. Notably, all these products were printed with the platform temperature set at room temperature, while the corresponding nozzle temperature was maintained at 230 degrees Celsius. The substantial temperature gradient resulted in inadequate adhesion between adjacent layers, leading to the occurrence of delamination. The improvement of this phenomenon will be discussed in the following section.

Observation of the microscopic structure in the cross-section of the obtained products reveals another defect: the presence of pores within the material matrix. These pores are commonly distributed in two primary regions: at the interfaces between adjacent layers and within the internal of each layer. Notably, the size of the pores tends to be larger at interlayer positions. The formation of these pores is primarily attributed to excessive temperature gradients, resulting in uneven flow of melted binder, lower adhesion between layers, and rapid cooling rates, consequently leading to the formation of bubbles. These defects adversely affect the performance and diminish the product's mechanical properties.

4.3.2 Optimized Modeling Results

Building upon the analysis in the previous section, this section adopted optimized parameters for the 3D printing of the micro-protrusions. In particular, we increased the platform temperature from the ambient environment to 100 degrees to reduce the temperature gradient and raised the layer thickness from 100 μm to 120 μm. Fig. 4-5 is the modeling results obtained under optimized printing parameters. The print results are depicted in Fig. 4-5(a). Currently, in the printing process, we attempted for the first time to print four rose thorn structures on the 15mm x 15mm area. These four rose thorn structures were arranged in two rows and two columns, ensuring the presence of the structures in both the x and y directions on the same plane.

Similar to the previous modeling experiments, the initial attempt to model a micro-protrusion with 1 mm height yielded an unsatisfactory result. It was confirmed again that the minute size was a crucial factor leading to the complete failure of the modeling process. Then, a double-scale model was adopted. The forming result indicated that it improved compared to the printing result of the previous model, which was the same size. This modification improved the modeling effect in the bottom region, but challenges in achieving shape satisfaction persisted in the tip area, as shown in Fig. 4-5(b). Subsequently, satisfactory modeling can almost be obtained by further enlarging the model to 2.5 times its original size. The base section presented a well-forming result, while the tip

section was still dissatisfactory. The cross-section morphology of the 2.5-scaled structure is presented in Fig. 4-5(c). Scaling the model to three times its initial size also demonstrated successful manufacturing, as shown in Fig. 4-5(d). To achieve the smallest possible model size while ensuring its form accuracy, the model size of 3 mm was ultimately chosen for subsequent debinding and sintering experiments.

Fig. 4-6 presents the obtained microstructure of the Green Part obtained with new printing parameters. Compared to Fig. 4-4(d), no porosity was observed within the product's interior. Under this set of printing parameters, the microstructure of the Green Part distinctly reveals the distribution of the binder and metal particles. Additionally, an increased binder between layers leads to observable boundaries between layers at the macroscopic level. The experimental results above demonstrate that reducing the temperature gradient between the printing platform and the printing material can effectively control inter-layer delamination defects and the occurrence of pores within the internal micro-structure of the Green Part. Additionally, increasing the thickness of the printing layers appropriately contributes to improving the forming accuracy of the final product.

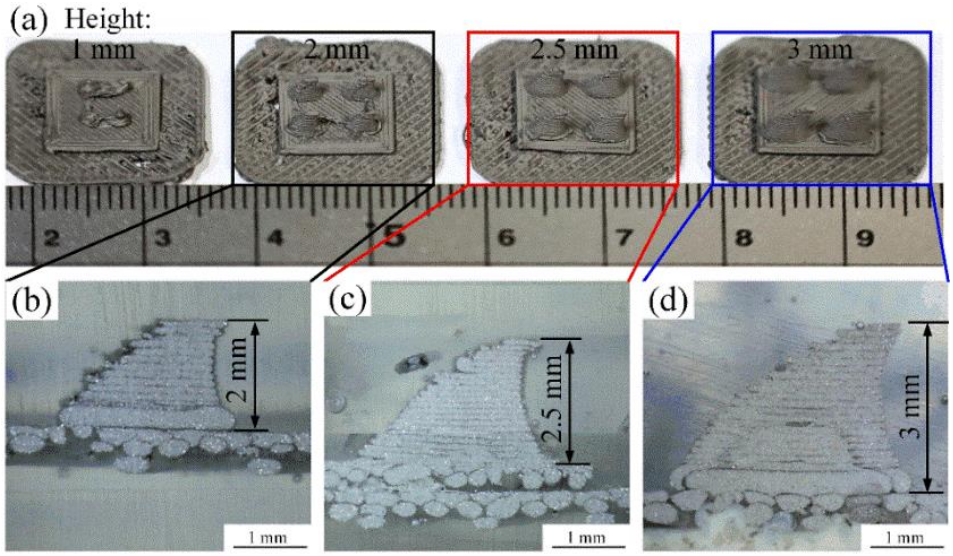

Fig. 4-5 Modeling results of green part with 100°C platform and 120 μm layer thickness: (a) modeling results with different scale under optical camera; (b) vertical section of the 2 mm protrusion; (c) vertical section of the 2.5 mm protrusion; (d) vertical section of the 3 mm protrusion.

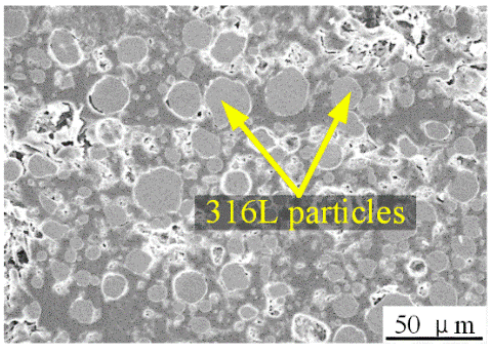

Fig. 4-6 Microstructures of the green part under new printing parameters.

4.4 Debinding Phase

Debinding is an indispensable stage in the post-modeling phase, particularly crucial for metal parts fabrication through the FDM process. It serves as an essential step wherein the polymeric matrix is meticulously removed from the green parts and retains the well-bonded 316L particles [149]. The significance of debinding extends beyond mere binder material removal. It stands as a pivotal factor influencing the final microstructure and properties of the sintered components [150]. The intricate interplay between debinding and sintering is instrumental in achieving the desired material characteristics, ensuring the printed components attain the required strength, density, and overall performance [151]. Thus, debinding stands as a critical and transformative stage, playing a key role in shaping the quality and properties of the final metal components manufactured through the FDM process [152].

According to the previous research results from other researchers, the debinding process is mainly influenced by the gas flow rate, where an insufficient rate impedes binder evaporation, leading to the retention of binders in brown parts [153]. This phenomenon can give rise to issues such as cracks, blistering, bloating, and internal voids during subsequent sintering [147]. In this experiment, we selected a debinding temperature of 300 degrees Celsius, a holding time of 90 minutes, and heating and cooling rates of 5 degrees per minute, as illustrated in Fig. 4-7, aiming to achieve an optimal debinding effect on the green parts [154]. The temperature of 300 degrees is effective in decomposing the polymer matrix. A holding time of 90 mins ensures efficient decomposition and removal of the polymer matrix, while heating and cooling rates help balance the impact of temperature changes on the structure and material, minimizing the occurrence of residual pores during the debinding process.

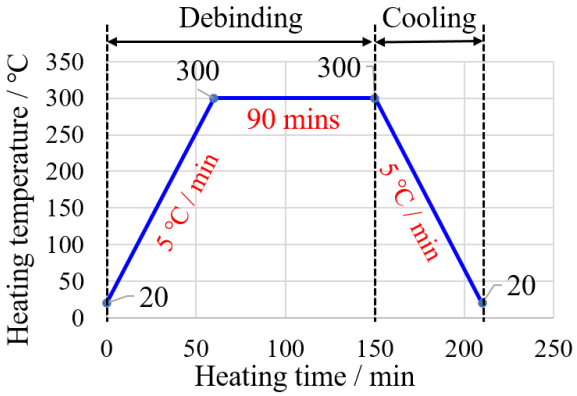

Fig. 4-7 Debinding temperature profile.

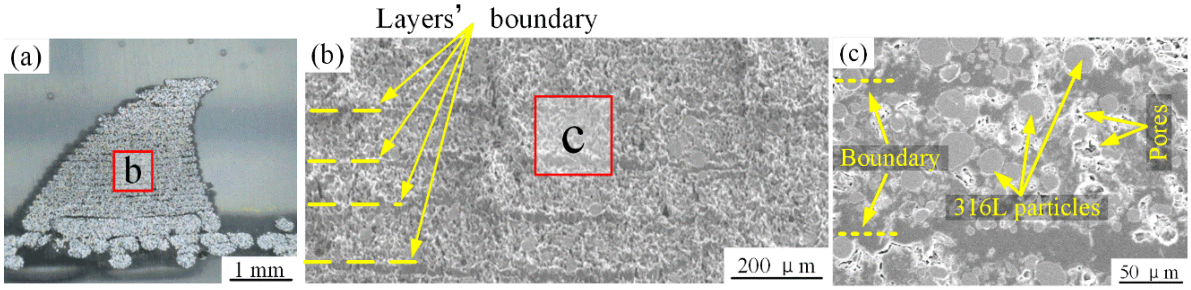

Fig. 4-8 Debinding results: (a) vertical section under the optical microscope; (b) microstructure of region b in Fig. 4-8(a); (c) magnification microstructure of region c in Fig. 4-8(b).

The microstructure of the debinded part serves as a tangible testament to the profound impact of debinding. The cross-section microstructure of the product is presented in Fig. 4-8. Fig. 4-8(a) illustrates the vertical section of the debinded product, which exhibits no significant difference in geometrical shape compared to Fig. 4-5(c). Fig. 4-8(b) presents the microstructure of region b in Fig. 4-8(a), and a more pronounced trace at the layers' boundary was observed. Additionally, there is a significant increase in the density of metal particles in interlayers, as shown in Fig. 4-8(c). Furthermore, some small pores were present in the microstructure at this stage, resulting inevitably from the melting and decomposition process of the matrix resin. By reducing the heating and cooling rates, the quantity and size of these pores at this stage can be effectively suppressed, although their occurrence cannot be entirely avoided.

4.5 Sintering Phase

Sintering, the final phase in the FDM process, is crucial in consolidating loose particles into a dense and cohesive body through controlled thermal treatment [186]. During sintering, the aggregation of powder particles forms cohesive bonds while undergoing pore shrinkage [187].

Among the various influential factors during the sintering process, the sintering temperature stands out as pivotal. It is noteworthy that many scholars in the field typically opt for sintering temperatures exceeding 1300 degrees Celsius, approaching the melting point of the metal [155, 156]. This process demands stringent requirements for the thermal treatment equipment. In our experimental setup, we deliberately employed comparatively lower temperatures to explore the effects, specifically at 500 ℃, 800 ℃, and 1000 ℃. Similarly, diverse durations of dwell time were also examined, including 90 mins, 180 mins, and 600 mins.

Additionally, influence factors, such as heating and cooling rates, in the sintering atmosphere are acknowledged to influence the sintering outcome. However, in alignment with prevailing research, our other experimental parameters were chosen to maintain consistency with established results [148, 157]. Ultimately, the microstructural characteristics of the produced structure under varying parameters were analyzed, and the effects of different parameters were summarized.

4.5.1 500 degrees Celsius

During the sintering process, the temperature is initially maintained at 500 ℃, designated as the starting stage of the sintering process. The temperature profile of the heat treatment process is illustrated in Fig. 4-9. Before sintering, the debinding process was reiterated to remove the binder from the Green Parts. Subsequently, the sintering process was carried out with a heating rate of 5 degrees per minute until reaching the maximum temperature of 500 ℃, held for 90 minutes, and then cooled to room temperature at a rate of 5 degrees per minute. The entire heat treatment process was conducted in the same furnace, with precautions taken to maintain the continuity by avoiding opening the furnace door during the sintering.

Fig. 4-10 presents the internal microstructure of the parts obtained under sintering conditions of 500 ℃ for 90 mins. Fig. 4-10(a) displays the product's vertical section, which resembles the morphology of the Green Part in Fig. 4-5. Fig. 4-10 (b) showcases the internal microstructure of the product obtained under these experimental conditions, with yellow lines representing the layers' boundaries. This figure shows a significant presence of numerous holes, contrasting sharply with the morphology of the Green Part and the product after debinding. The holes depicted in Fig. 4-10 (b) extend not only to the surface but also into the product's internal structure. Moreover, these holes exhibit distinct regional concentrations, primarily concentrated at the boundaries between layers.

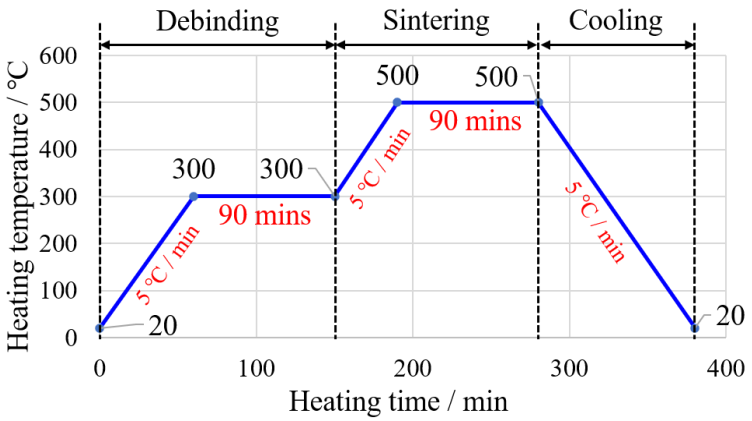

Fig. 4-9 Temperature profile of sintering under 500 °C, 90 mins.

Additionally, Fig. 4-10 (b) reveals a collapsing phenomenon where the entire region is notably lower than the surrounding area. This also indicates the thorough removal of organic matter from the product in this environment, resulting in a volumetric loss in that region. Another phenomenon observed is that after sintering at 500 °C for 90 minutes, the boundaries between layers are no longer very distinct. This suggests that in this sintering environment, metal particles undergo deposition, reducing gaps between metal particles and increasing density, as demonstrated in Fig. 4-10(c) and 4-10(d). Furthermore, it is noteworthy that despite the significant defects present in the products obtained under these sintering parameters, relatively ideal results can still be observed in the cross-section, as shown in Fig. 4-10(d), where the microstructure indicates the absence of pore occurrence between layers. However, organic matter still existed between metal particles, indicating that the final product obtained under these deposition parameters is not ideal.

In addition to addressing microstructural intricacies and managing porosity during the sintering process, ensuring optimal mechanical performance of the final sintered parts is paramount. The controlled removal of binders and subsequent sintering steps significantly influence the components' mechanical properties. Typically, a sintering temperature of 500°C is not sufficient to achieve complete melting and bonding of metal particles. Consequently, inter-particle bonding is insufficient to provide adequate structural support. Under slight force application, structural disintegration of the product occurred, with the product easily crumbling into powder upon gentle pressure, indicative of its brittleness, as illustrated in Fig. 4-11.

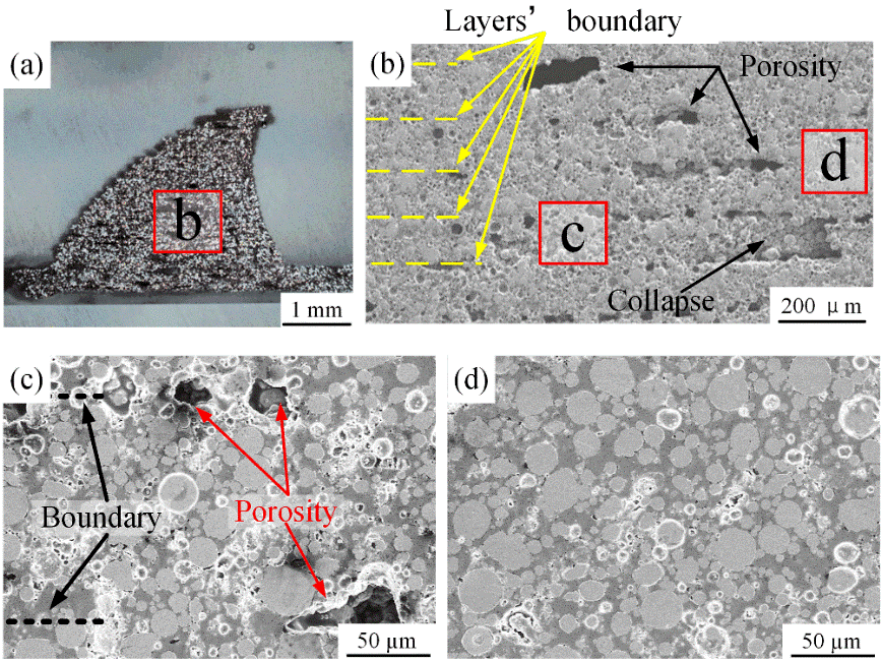

Fig. 4-10 Sintering results under 500 ℃, 90 mins：(a) vertical section under optical microscope; (b) microstructure of region b in Fig. 4-10(a); (c) magnification microstructure of region c in Fig. 4-10(b); (d) magnification microstructure of region d in Fig. 4-10(b).

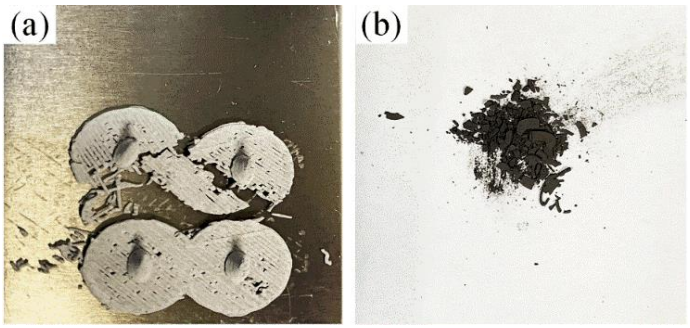

Fig. 4-11 Brittle phenomenon observed after sintering under 500 ℃, 90 mins: (a) the product just removed from the furnace; (b) slight crushing of the powder with the fingertip.

Higher sintering temperatures are often necessary to ensure thorough bonding of metal particles, enhancing mechanical strength in the final product and providing superior mechanical performance. This necessitates a meticulous balance between sintering temperature and duration to achieve optimal densification and mechanical integrity while mitigating the risk of over sintering-induced defects. Such optimization endeavors are crucial for fabricating components that meet stringent mechanical specifications and withstand operational stresses within demanding applications.

4.5.2 800 Degrees Celsius

Based on the sintering results at 500 °C, we further elevated the temperature to 800 °C and extended the holding time to 180 minutes. It is noteworthy that the heating and cooling rates remained unchanged. The adjusted temperature curve is depicted in Fig. 4-12.

The microstructural analysis was conducted under the conditions of 800 °C and 180 minutes of holding time. As depicted in Fig. 4-13(a), observations between deposition layers reveal the persistence of hole defects. These defects were concentrated predominantly at the boundaries between layers, consistent with previous findings. Moreover, their aggregation appeared more pronounced compared to the conditions illustrated in Fig. 4-10(b). Notably, the size of these holes slightly exceeds those observed at 500 °C. Furthermore, the internal organization displays a noticeable increase in the density of metal particles, as evidenced in Fig. 4-13(b) and (c). Noteworthy is the occurrence of localized fusion phenomena at the boundaries between metal particles, like in Fig. 4-13(c). This observation suggests a more pronounced sintering phenomenon under the specified sintering condition, indicative of enhanced metal particle coalescence.

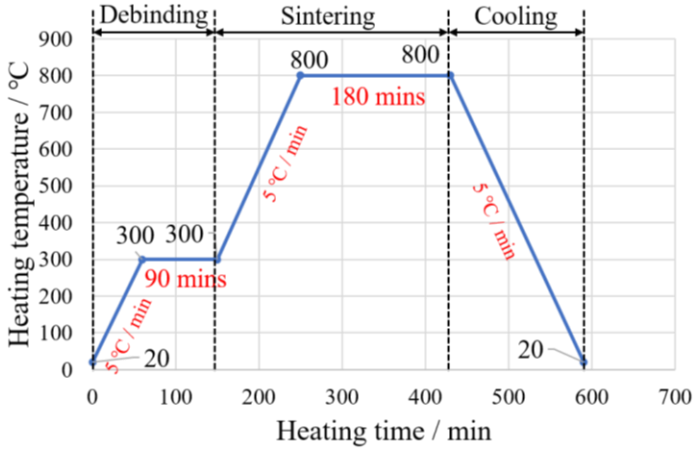

Fig. 4-12 Temperature profile of sintering under 800 °C, 180 mins.

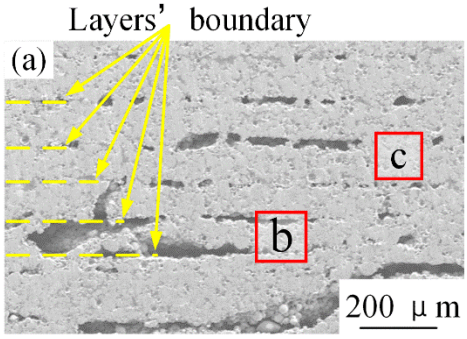

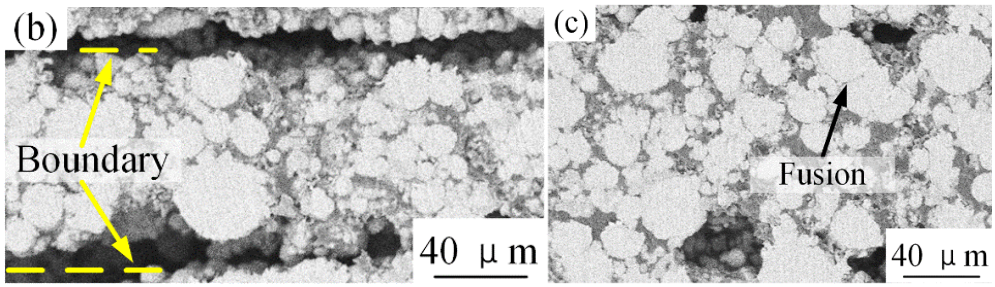

Fig. 4-13 Sintering results under 800 ℃, 180 mins holding time：(a) microstructure of the vertical section; (b) magnification microstructure of region b in Fig. 4-13(a); (c) magnification microstructure of region c in Fig. 4-13(a).

The aforementioned results suggest that raising the sintering temperature to 800 °C and extending the holding time to 180 minutes significantly affect the sintering process. Firstly, elevating the sintering temperature to 800 °C resulted in more thorough particle deposition and surface diffusion, thereby enhancing the interaction between metal particles. This is expected to increase the density and mechanical properties of the sintered body and further optimize its microstructure. Simultaneously, extending the holding time to 180 minutes provides more ample time for the sintering process, ensuring uniform heating and reaction of the material, thereby further enhancing the density and performance of the sintered body. To further eliminate hole defects while maintaining the sintering temperature at 800 °C, the sintering time was extended to 10 hours. The temperature curve at this point is shown in Fig. 4-14.

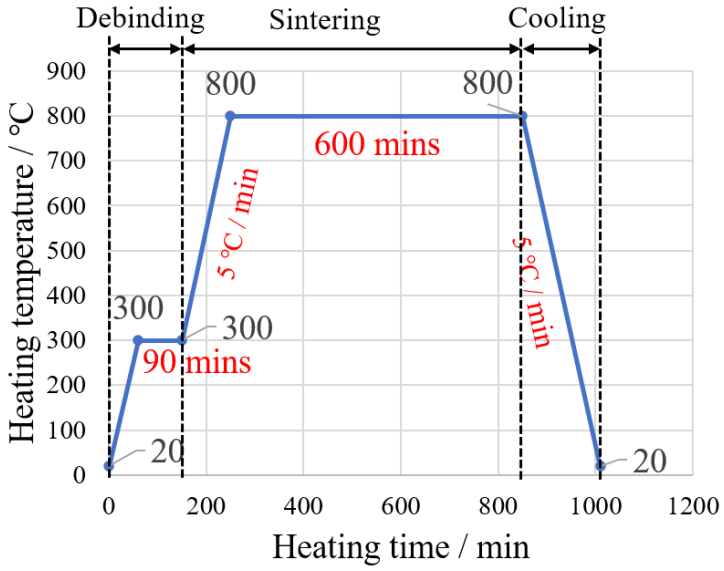

Fig. 4-14 Temperature profile of sintering under 800℃, 600 mins.

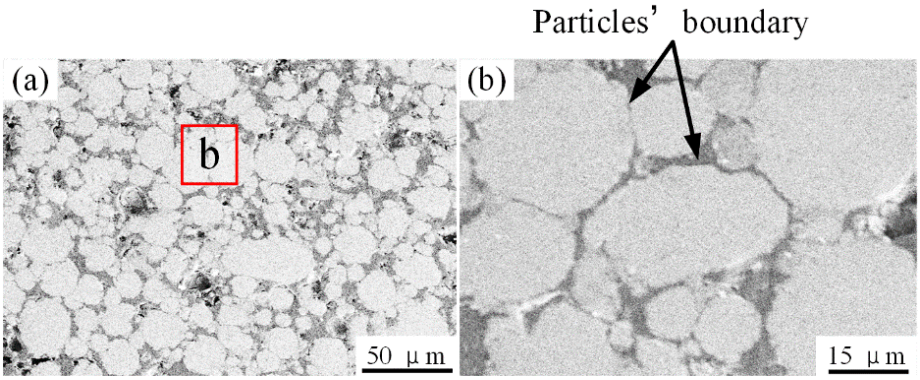

Fig. 4-15 Sintering results under 800 ℃, 600 mins holding time：(a) microstructure of the vertical section; (b) magnification microstructure of region b in Fig. 4-15(a).

Fig. 4-15 presents the microstructure obtained after extending the deposition time to 10 hours under sintering conditions at 800°C. Upon observing the results in the figure, a noticeable trend of significant reduction in pore size and quantity is evident. This indicates that extending the deposition time effectively reduces the occurrence of pores during the FDM process. However, it is noteworthy that microscopic observation reveals the presence of some bonding between the boundaries; however, due to limitations in sintering temperature and time, this bonding was not complete, resulting in minor gaps and incomplete fusion at the boundaries, as shown in Fig. 4-15 (b).

The aforementioned phenomena illustrate that during the sintering process, the diffusion process between metal particles was more fully developed with the extension of deposition time, which is conducive to reducing interparticle voids and pore formation. However, although extending the deposition time can significantly reduce the porosity, achieving complete fusion of metal particles requires further process optimization and control.

In addition, we performed binarization processing on the microscopic morphology of the products obtained under different parameters using ImageJ software and conducted a detailed analysis of the volume fraction of metal particles and binder in the images. As shown in Fig. 4-16, the volume fraction of metal particles shows a gradual increase trend with the progress of post-heat treatment. When the sintering temperature reaches 800 ℃ and lasts for 10 hours, the volume fraction of metal particles reaches the highest value of 94.7%. This trend suggests that post-processing significantly enhances the proportion of metal particles, providing an important reference for the ultimate performance of the material.

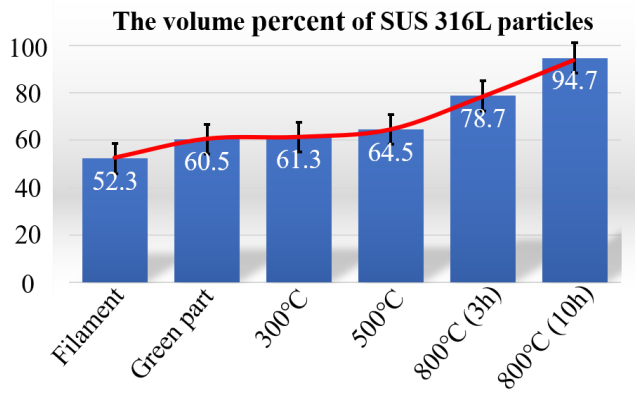

Fig. 4-16 The volume percentage of SUS 316L particles.

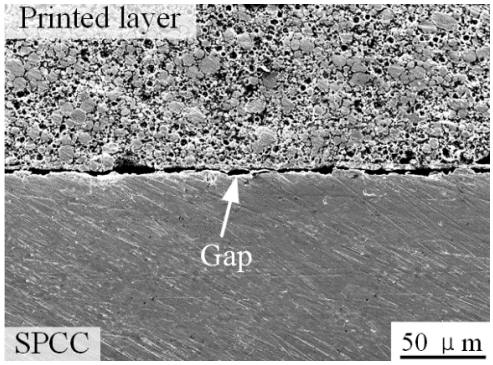

Fig. 4-17 The binding result between the printed part and the metal substrate.

Under the current heat treatment conditions, poor connecting between the printed micro-protrusions and the metal surface, as depicted in Fig. 4-17, has been noted. The primary cause is attributed to insufficient metallurgical bonding due to inadequate diffusion, resulting in substantial gaps between the printed product and the metal substrate. Such poor connection adversely affects the performance of joints when joining with CFRP. This inadequate bonding arose from the failure to achieve sufficient inter-metallic diffusion during the heat treatment process.

4.5.3 1000 Degrees Celsius

To address the issues encountered at 800 ℃, this study further elevated the sintering temperature to 1000 ℃ and employed insulation times of 180 and 600 minutes, respectively. This adjustment aimed to enhance the sintering process by elevating the sintering temperature and extending the holding time, thereby improving the density and structural stability of the parts. The time-temperature curves, as depicted in Fig. 4-18 and 4-19, illustrate the heat treatment process of the material under different conditions.

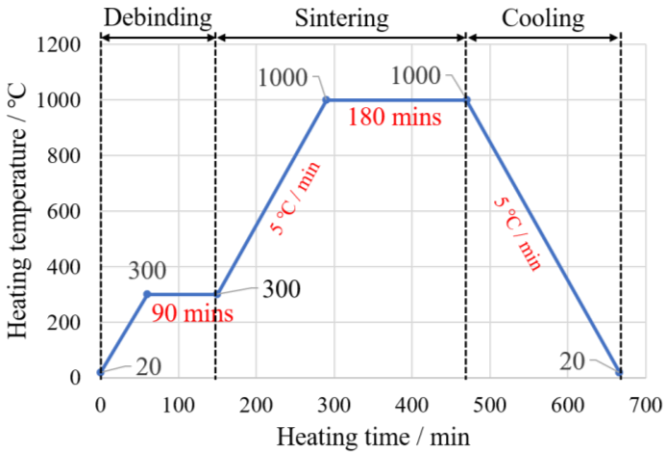

Fig. 4-18 Temperature profile of sintering under 1000℃, 180 mins.

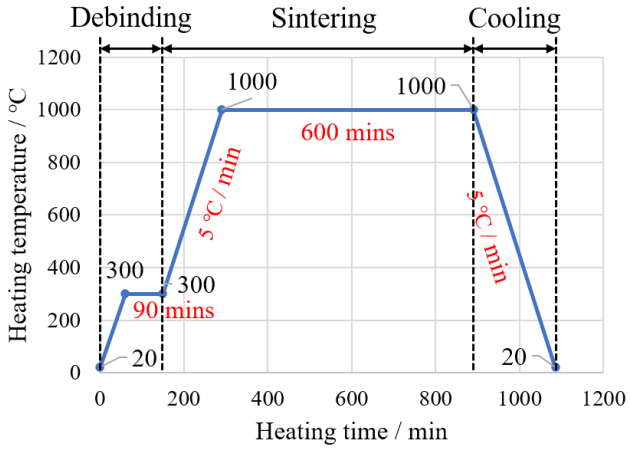

Fig. 4-19 Temperature profile of sintering under 1000℃, 600 mins.

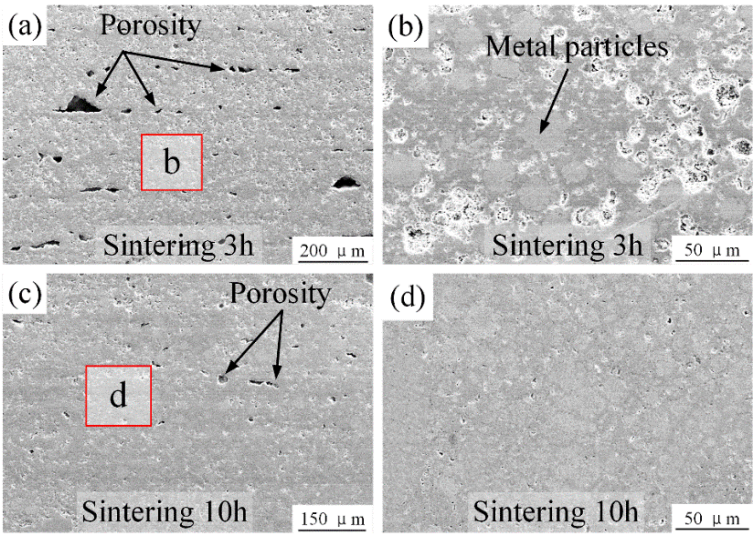

Fig. 4-20 Sintering results under 1000 ℃, 180 mins, and 600 mins holding time：(a) microstructure of the vertical section under 1000 ℃ and 180 mins; (b) magnification microstructure of region b in Fig. 3-20(a); (c) microstructure of the vertical section under 1000 ℃ and 600 mins; (d) magnification microstructure of region d in Fig. 4-20(c).

Fig. 4-20 illustrates the product's microstructure obtained under 1000°C sintering with the holding time of 3 hours and 10 hours, respectively. By comparing Fig. 4-20 (a) and 4-20 (c), significant pore size and quantity differences are observed under the same sintering temperature but different holding times. Pores are larger with a 3-hour holding period while slightly smaller with a 10-hour holding period. Furthermore, compared to Fig. 4-13, there is a gradual decrease in pore size and quantity in Fig. 4-20. Additionally, when the sintering time is 3 hours, the fusion between metal particles was insufficient, as evidenced by the relatively separated metal particles observed in Fig. 4-20 (b). Conversely, with a sintering time of 10 hours, the fusion between metal particles becomes more pronounced. The overall structure exhibits uniformity, as depicted in Fig. 4-20 (d). This indicates that with prolonged sintering time, the degree of bonding between metal particles increases, reducing pore size and quantity and creating a denser and more uniform microstructure.

The influence of sintering time and temperature in the FDM process is considered to be two primary factors during the solidification process. With an increase in solidification time, the degree of bonding between raw materials strengthens, increasing product density, which suppresses pore formation, resulting in relatively smaller pore size and quantity. On the other hand, the elevation of solidification temperature promotes the movement and diffusion of raw material molecules, facilitating the reduction of pore size and quantity. Additionally, it aids in the fusion between metal particles, enhancing the final product's mechanical properties. However, it is worth noting that small pores persist even with a sintering temperature of 1000°C and an insulation time of 10 hours adopted in this study. This phenomenon remains unresolved in the current study.

4.6 The Final Micro-protrusion

After conducting the aforementioned experiments and analyzing the observed phenomena, we opted to subject all micro-protrusions to sintering post-processing, with a sintering temperature of 1000 degrees Celsius and a holding time of 10 hours. The final appearance of the micro-protrusions is depicted in Fig. 4-21. Given that the printed model was three times the original model's size, the micro-protrusions' dimensions in the longitudinal and transverse directions were initially 4.248 millimeters and 2.124 millimeters, respectively. Following sintering, the dimensions of the micro-protrusions in the longitudinal and transverse directions were measured at 3.37 millimeters and 1.72 millimeters, respectively. This indicates a horizontal shrinkage of approximately 21% during sintering.

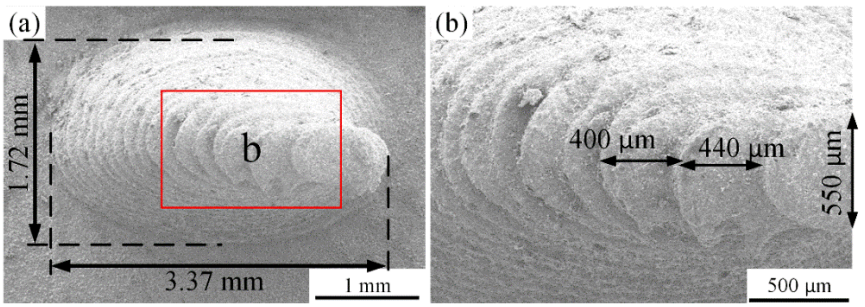

Fig. 4-21 Final product obtained under 1000℃, 10 h sintering condition: (a) from top view; (b) magnification of the region b in Fig. 4-21(a).

At the apex of the micro-protrusions, the final morphology is not entirely sharp, with the maximum dimension of the topmost deposited layer being approximately 550 μm. Additionally, the accuracy of the top few layers of the micro-protrusions' formation is relatively low, with a noticeable "step-like" transition between layers, with these "steps" measuring up to approximately 400 μm. As one moves towards the middle and lower sections of the structure, the size of the "steps" slightly decreases, although the stratification between layers remains clearly visible.

4.7 Conclusions

Based on the rose thorn biomimetic-shaped structure identified in Chapter 3, this chapter employed the FDM method to print it and investigated three stages of the entire FDM process. The following conclusions were drawn:

1、During the modeling stage, the platform temperature emerged as a critical influencing factor. Excessive temperature gradients led to phenomena such as interlayer separation and the formation of numerous small pores within the internal structure. This may be attributed to uneven material curing and stress accumulation induced by temperature gradients, resulting in diminished product quality.

2、Sintering phenomena began to occur at 500 degrees Celsius, although this sintering temperature alone did not yield satisfactory mechanical properties in the final product. The poor mechanical performance of the final product was attributed to incomplete removal of the debinding agent and the absence of effective metal fusion between metal particles. This insufficiency in sintering temperature likely hindered the bonding and fusion between metal particles.

3、Throughout the sintering process, the emergence of small pores posed a significant defect issue. Elevating the temperature to 1000 degrees Celsius and holding it for 10 hours

effectively reduced the size and quantity of these small pores. However, under these conditions, the complete elimination of small pores remained elusive. This may be due to the release of volatile substances from the material during the sintering process and structural adjustments, necessitating further research to address this issue.

Chapter 5 Joint Mechanical Properties and Disassembly Process Evaluation Based on FDM-Manufactured Biomimetic Micro-Protrusions

5.1 Introduction

In the preceding chapters, comprehensive investigations explored the feasibility of achieving easy disassembly joints between metal and CFRP materials. Specific rose thorn biomimetic micro-protrusions were developed through systematic analyses and design to facilitate this objective. In particular, Chapter 4 utilized FDM technology to fabricate rose thorn biomimetic micro-protrusions on the surface of SPCC substrates. These micro-protrusions aimed to facilitate the easy disassembly joining between the structured SPCC and CFRP. Building upon the insights gained from earlier experimental studies, the 5th chapter delves deeper into the characterization and evaluation of surface-structured SPCC and CFRP joints. This includes a detailed examination of the morphology of the joint interfaces, mechanical performance, and the disassembly process post-joining. By elucidating the intricacies of these surface-structured joints, this study seeks to provide valuable insights into the metal-CFRP joining for applications requiring ease of assembly and disassembly.

5.2 Experimental Procedures

5.2.1 Materials

a) Chopped CFRP

The CFRP material is adopted the same as in Fig. 2-1. Although chopped CFRP sheets exhibit good formability in practical applications, they have noticeable deficiencies in mechanical performance. This is primarily due to the fabrication process of this material. As a composite, chopped CFRP sheets are produced by cutting carbon fibers into shorter lengths and combining them with a PA6 intermediate layer. However, unlike continuous fibers, this bonding method does not provide the same strength and load-bearing capacity. Additionally, since the carbon fibers in chopped CFRP sheets are in short-fiber form, their dispersion and interlayer bonding in the composite are relatively poor, resulting in weaker connections between the fibers, affecting overall tensile strength and toughness. Consequently, when tensile stress is applied in the planar direction, the PA6 intermediate layer becomes the primary load-bearing component.

To improve the mechanical performance of chopped CFRP sheets, this study proposes enhancing the structural strength of this material through epoxy resin coating on its surface. This

surface treatment is expected to strengthen the bond between the carbon fibers and the matrix, thereby improving overall mechanical properties, including tensile strength, impact resistance, and fatigue life.

b) Epoxy resin

Epoxy resin is a versatile and widely used material in various industries, including aerospace, automotive, marine, and construction, due to its exceptional properties and ease of use [89, 158]. One of its notable applications is in the enhancement and protection of chopped CFRP sheet surfaces [159]. Using epoxy resin on chopped CFRP surfaces yields many advantages, including enhanced aesthetic appeal, high transparency, and a smoother surface texture. Importantly, epoxy resin contributes to the enhancement of mechanical properties of the chopped CFRP sheet, such as strength, stiffness, fatigue resistance, impact resistance, and surface wear resistance [160].

In terms of handling characteristics, the epoxy resin offers a pot life of approximately 28 minutes, allowing sufficient time for application and manipulation before it begins to cure. Once applied, the resin fully cures within about 16 hours at a temperature of 25°C, forming a durable and resilient bond with the chopped CFRP substrate.

c) Epoxy resin infused chopped CFRP

A manual coating method was employed in this experiment to enhance the mechanical properties of the chopped CFRP sheet, utilizing epoxy resin to treat the surface of the chopped CFRP. Firstly, the chopped CFRP was cut into the required dimensions and placed on a suitable working platform. Ensuring surface cleanliness and dryness to facilitate effective epoxy resin penetration and curing. Subsequently, epoxy resin was mixed in a 2:1 ratio and evenly applied to the surface of the chopped CFRP sheet using a brush. During the coating process, it was ensured that the resin penetrated sufficiently between the fibers to enhance bonding strength. Then, a compaction tool was used to compact the coated samples to ensure uniform resin distribution and effective fiber bonding. Finally, the samples were cured in an environment at 25°C. It is worth noting that during the manual coating process, one end of the chopped CFRP sheet was preserved for the area where the joint with the metal would be formed. As this area was not hardened by resin, the tip of the rose thorn on the metal surface facilitated piercing through the entire carbon fiber, forming the joint. Schematic and actual images of the entire process are shown in Fig. 5-1.

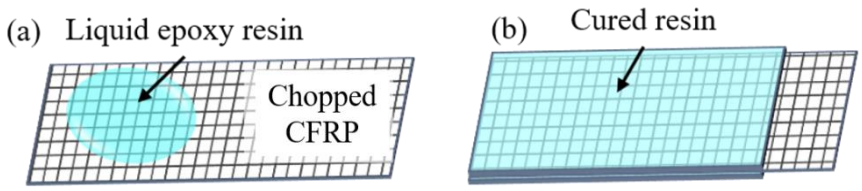

Fig. 5-1 Epoxy resin-infused processes: (a) pour liquid epoxy resin on chopped CFRP; (b) partially cured chopped CFRP.

5.2.2 Joining Methods

The metal part is manually integrated into the CFRP during the forming process, using the interlocking technique of the carbon fibers with the metal anchors. The CFRP component of the joint is manufactured by utilizing a manual process of applying epoxy resin to a dry twill carbon fiber weave.

After obtaining the chopped CFRP sheet infused with epoxy resin is connected to an SPCC plate with micro-protrusions. Prior to the connection, the cleanliness of the SPCC plate surface is ensured, and alignment between the reserved connection area of the chopped CFRP sheet infused with epoxy resin and the structured area on the SPCC surface is confirmed to ensure connection accuracy. During the connection process, the tips of the micro-protrusions are first inserted into the gaps between the carbon fibers at an appropriate angle, and external force is then applied to compress the CFRP onto the metal plate. The micro-protrusions gradually penetrate the carbon fiber sheet throughout this process, ultimately achieving the connection effect. The entire process is illustrated in Fig. 5-2. Following the completion of the connection, the same resin is applied to the connection area to ensure uniformity of the entire carbon fiber sheet. Subsequently, after the resin has solidified and formed the final connection joint, it is ensured during the connection process that the tips of the micro-protrusions are effectively inserted into the carbon fiber sheet, and an adequate amount of resin is applied to ensure the strength and durability of the joining.

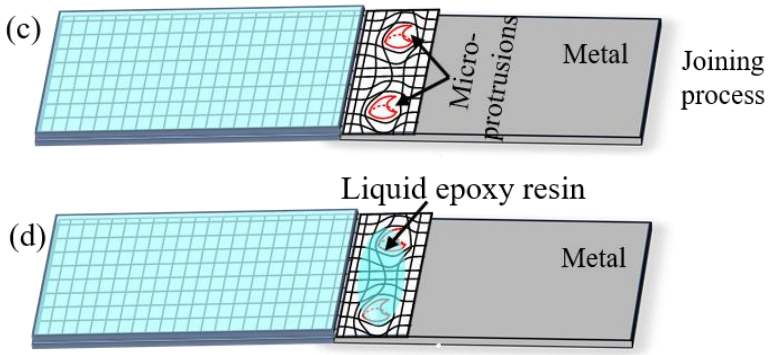

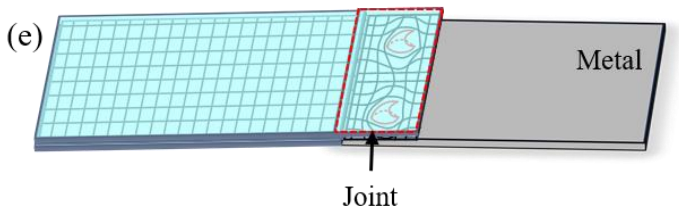

Fig. 5-2 Schematic diagram of the joining processes: (c) joining process; (d) pour liquid epoxy resin on the joining area; (e) finished joint.

5.2.3 Disassembly Method

A simplified disassembly process helps improve the maintenance efficiency and reusability of the joints. On the other hand, in studying the damage to materials after disassembly, we will focus on the impact of the disassembly process on metal and carbon fiber sheets. Particularly, attention will be paid to whether the disassembly process causes material damage, deformation, or other forms of damage, thus affecting the material's reusability or continued use.

The CFRP-SPCC joints based on FDM-manufactured micro-protrusions on the metal surface exhibit certain challenges and characteristics during disassembly. The disassembly strategy has been elaborated in detail in the previous section, 3.3.2, and Fig. 5-3 can be used to illustrate the disassembly steps. According to the design, the outer profile of the micro-protrusion was designed to be arc-shaped, aiming to facilitate the disassembly process. The disassembly process starts from the left side of the joint. Initially, the metal plate was fixed on the platform, and then one side of the carbon fiber was gripped with pliers to separate the carbon fiber plate from the metal in a tearing manner. The disassembly process can be divided into the following three steps.

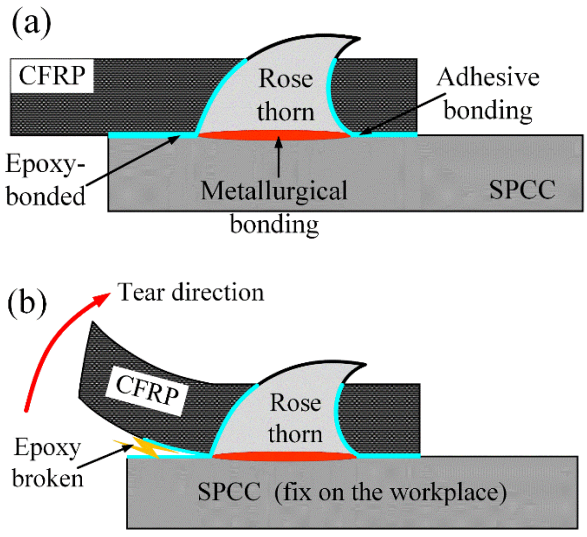

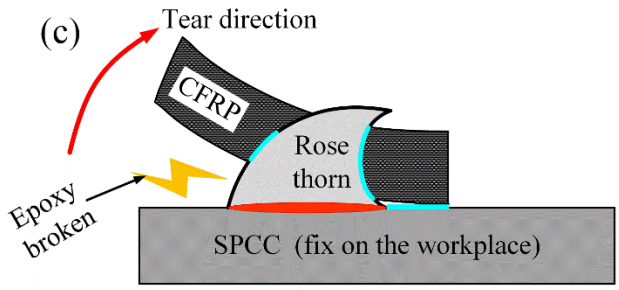

Fig. 5-3 Schematic diagram of disassembly processes: (a) initial joint stage; (b) tear direction diagram; (c) tear process.

5.3 Joint Morphology Analysis Based on FDM-Manufactured Micro-Protrusions

In this section, the analysis is first conducted on the joint between CFRP and SPCC, which fabricated the rose thorn biomimetic micro-protrusions on its surface using the FDM method. Fig. 5-4 illustrates the morphology of the joints at various locations under an optical microscope. Specifically, Fig. 5-4(a) depicts a schematic diagram of the joint at different positions. In the joint prepared by this joining method, the morphology of the upper surface and the location of the left side significantly influence the joint's performance. Therefore, the morphology at these two positions was analyzed in detail. Fig. 5-4(b) displays the morphology of the upper surface of the joint after the structured SPCC is joined to the CFRP without epoxy resin curing. The apex of the micro-protrusions penetrated through the entire chopped CFRP sheet, causing fracture of the carbon fiber filaments in the surrounding area of the micro-protrusions. Fig. 5-4(c) shows the surface morphology after epoxy resin curing of the joint area, where the resin uniformly covered the upper surface of the joint, with some areas exhibiting reflection.

Fig. 5-4(d) illustrates the morphology of the left side of the joint before resin curing. A significant gap between the chopped CFRP sheet and the SPCC was observed, with partial micro-protrusions visible at the root of this gap. This situation represents the limit of the joining, meaning that the chopped CFRP cannot be fully matched with the SPCC plate. This is attributed to the large rough micro-protrusions produced on the SPCC surface by the FDM method, as shown in Fig. 4-21, with their outer profile not being smooth, especially in the tip region. Due to the large “stage-platform” spacing between adjacent layers, the chopped CFRP encountered significant resistance when sliding down after passing through the tip region, leading to this phenomenon. Fig. 5-4(e) shows the morphology of the left side of the joint after resin curing, where the cured resin filled the gap area observed in Fig. 5-4(d), indicating an ideal joint.

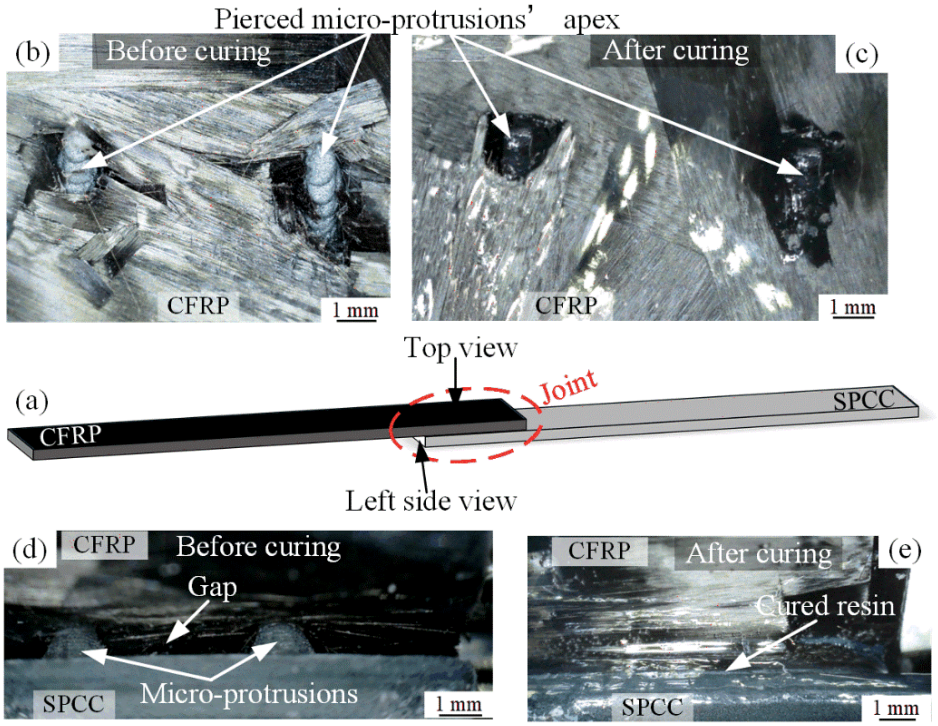

Fig. 5-4 Joint morphology based on FDM: (a) diagram of the joint positions; (b) joint top surface morphology before epoxy resin curing; (c) joint surface morphology after epoxy resin curing; (d) joint left side view before epoxy resin curing; (e) joint left side view after epoxy resin curing.

Fig. 5-5 presents the upper surface morphology of the joint observed using SEM. In contrast to the macroscopic morphology under optical microscopy, SEM allows for the observation of more detailed features. In Fig. 5-5(a), it can be observed that when the tips of micro-protrusions penetrated the chopped CFRP, the carbon fibers on the surface were severely damaged, resulting in many carbon fibers breaking. Fig. 5-5(b) and 5-5(c) provide clearer details of the carbon fiber breakage issue. The damage to the chopped CFRP sheet caused by this joining will inevitably lead to a decrease in the overall performance of the carbon fiber board.

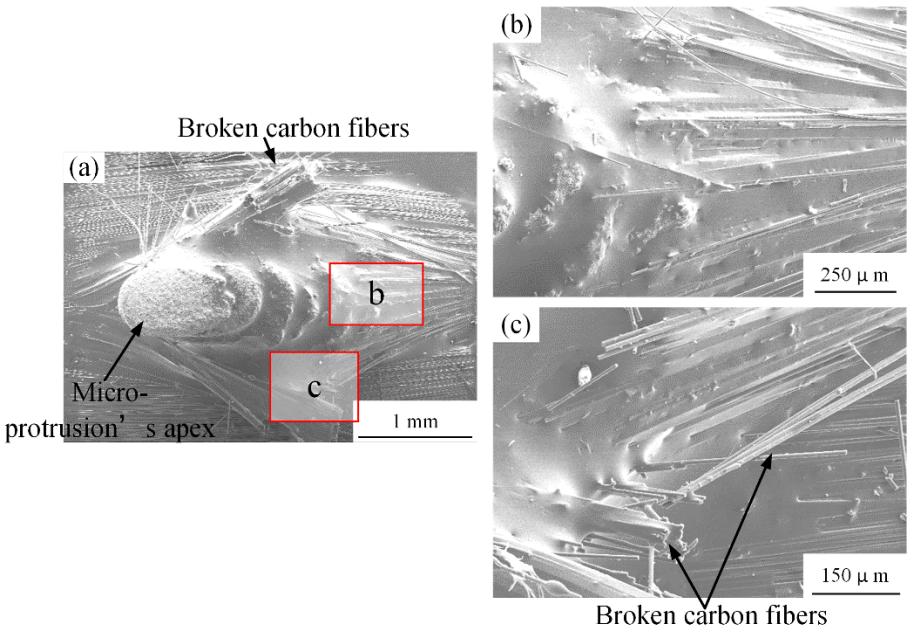

Fig. 5-5 Top side view of the joint under SEM: (a) morphology of the joint top surface; (b) magnification of zone b in Fig. 5-5(a); (c) magnification of zone c in Fig. 5-5(a).

Fig. 5-6 presents the microstructure of the vertical section of the joint. Fig. 5-6(a) represents the image obtained through an optical microscope. From Fig. 5-6(a), the positional relationship between micro-protrusions and the CFRP can be clearly observed, indicating that the CFRP cannot fully conform to the root of the micro-protrusions. This is consistent with the gap on the left side of the joint shown in Fig. 5-4(d), which was explained before. Additionally, delamination of the CFRP can be observed at the upper left position in Fig. 5-6(a), which is also attributed to the excessive surface roughness of the micro-protrusions manufactured based on FDM. When subjected to external force, the CFRP encounters significant resistance as it slides along the contour of the micro-protrusions, ultimately leading to the separation of carbon fibers in chopped CFRP. Such delamination during the joining process is bound to affect its performance; therefore, it should be avoided as much as possible during the joining process.

Fig. 5-6(b) illustrates the vertical section morphology of the joint obtained through SEM. In the image, the structure of the micro-protrusions is clearly visible, although the carbon fibers are less pronounced in Fig. 5-6(b) due to the poor conductivity of carbon fiber filaments. However, their presence can still be observed, and their position is almost identical to that in Fig. 5-6(a). Furthermore, the joining situation between the carbon fibers and the inner and outer contours of the micro-protrusions was further examined. Fig. 5-6(c) demonstrates the joining condition between the outer contour of the micro-protrusions and carbon fibers. There are no observed gaps

or significant porosity over the contact boundary. Even some filling in the step area between adjacent layers of micro-protrusions is visible, indicating a good joining effect between carbon fibers and micro-protrusions in this contact area. Fig. 5-6(d) displays the joining result between the inner contour of the micro-protrusions and carbon fibers, showing no gaps between carbon fibers and micro-protrusions. And some carbon fibers on the CFRP side remain consistent with the inner contour of the micro-protrusion. This further demonstrates that this joining method can achieve effective joining at the vertical section of the micro-protrusions and carbon fibers interface.

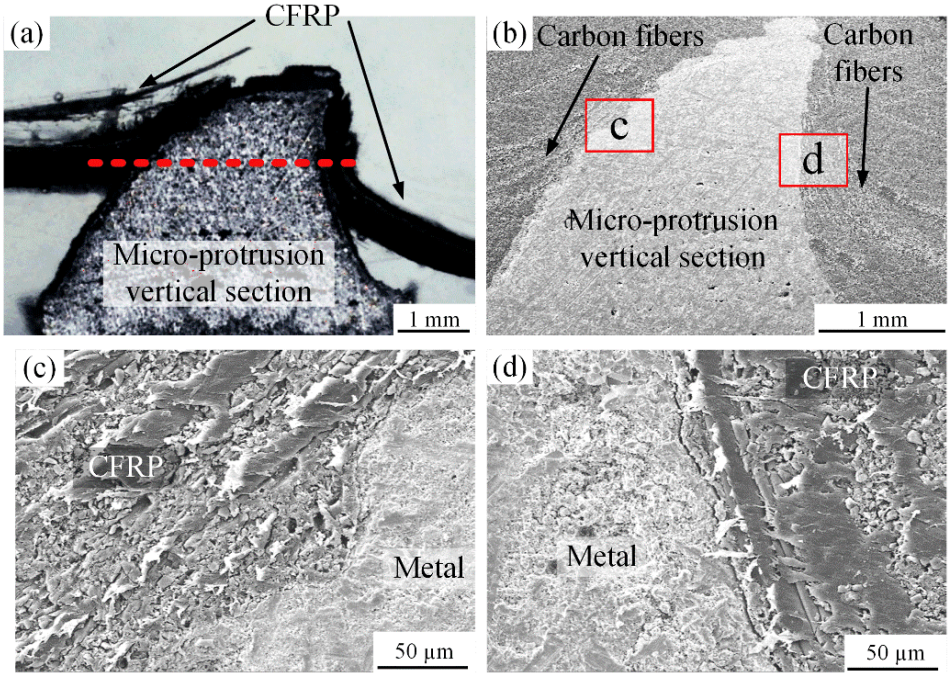

Fig. 5-6 Joint cross-section microstructures based on FDM: (a) joint cross-section under the optical microscope; (b) joint cross-section under SEM; (c) magnification of zone c in Fig. 5-6(b); (d) magnification of zone d in Fig. 5-6(b).

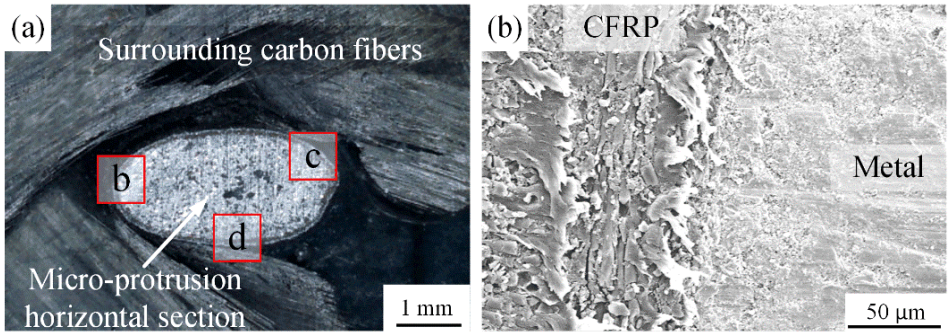

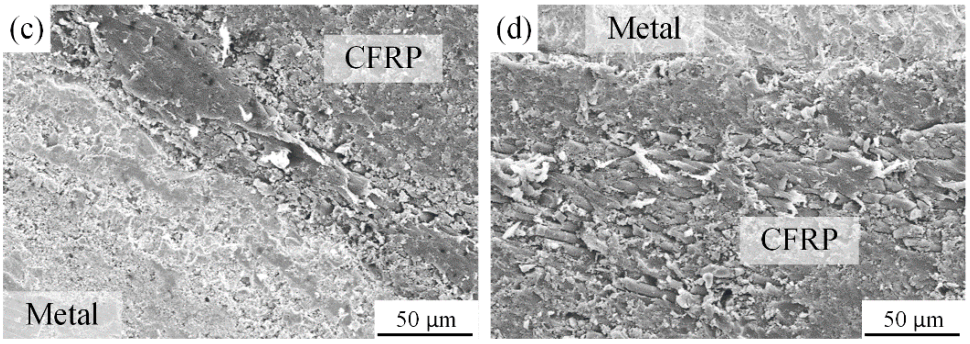

Fig. 5-7 Middle horizontal section view of the joint based on FDM: (a) joint morphology under the optical microscope; (b) magnification of zone b in Fig. 5-7(a); (c) magnification of zone c in Fig. 5-7(a); (d) magnification of zone d in Fig. 5-7(a).

Fig. 5-7 illustrates the morphology of the joint at a horizontal section. This section is located at the position indicated by the red dashed line in Fig. 5-7(a), encompassing both the carbon fiber sheet and the micro-protrusion. By examining the bonding condition at this location, a better understanding of the joining mechanism at the joint site can be obtained. Fig. 5-7(a) displays the joining condition at this horizontal section obtained under an optical microscope. It can be observed that the horizontal section of the micro-protrusion appears elliptical and is surrounded by carbon fibers. However, the optical microscope cannot reveal the condition at the boundary between the micro-protrusion and the carbon fibers. Therefore, regions b, c, and d were selected for observation under SEM in Fig. 5-7(a). The results, as shown in Fig. 5-7(b), (c), and (d), indicate that in each region, there are no noticeable bonding defects, such as gaps or pores at the boundary between the micro-protrusion and the carbon fibers. This further demonstrates that this joining method can achieve a robust joint at the interface between the micro-protrusion and the carbon fibers.

In the process of joining CFRP to metal after applying rose thorn biomimetic micro-protrusions manufactured using the FDM method, certain defects were observed in the joint morphology. Firstly, due to the significant rough of the micro-protrusion surface, there was incomplete contact between the CFRP and the metal plate, resulting in areas of inadequate contact. This condition may potentially reduce the strength and stability of the joint. Secondly, during the joining process, the large platform gap between adjacent layers of the micro-protrusion surface could cause delamination of the CFRP under external forces, leading to structural instability in the joint area, thereby affecting the performance and reliability of the joining.

However, despite these defects, the regions capable of forming effective joining, including the horizontal and vertical cross-sections, exhibit favorable joint formation under observation. This

indicates that although challenges exist in certain aspects, micro-protrusions manufactured based on the FDM method still hold the potential for achieving reliable joining between CFRP and metal under specific conditions. Therefore, future research efforts could focus on improving the fabrication process of micro-protrusions and optimizing the joining process further to enhance the quality and stability of the joining.

5.4 Joint Mechanical Properties Based on FDM-Manufactured Micro-Protrusions

The tensile test results of the joints connecting metal and carbon fiber with surface-structured patterns using the FDM method are as follows. During the tensile process, the schematic diagram of the fracture location is shown in Fig. 5-8(a), with the final fracture occurring at the joint. Along with the joint, the FDM-manufactured micro-protrusions also fractured. Fig. 5-8(d) depicts the metal side's morphology after fracture, showing residual carbon fibers on the metal surface and the fractured micro-protrusions. The presence of carbon fibers on the metal surface was attributed to the phenomenon of carbon fiber delamination during the joining process, the causes of which have been analyzed and discussed in Section 5.3. The delamination of carbon fibers results in the failure of carbon fibers at the joint, leading to fracture during the tensile process.

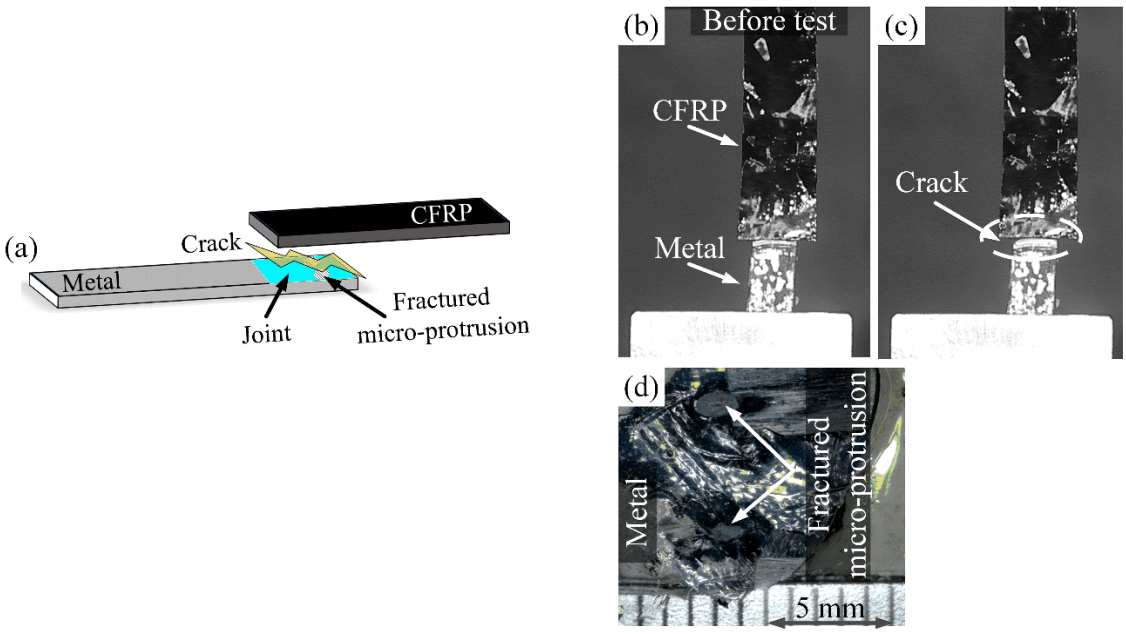

Fig. 5-8 Tensile test of the CFRP-SPCC joint based on FDM-manufactured micro-protrusions: (a) diagram of the break position; (b) sample before test; (c) sample after test; (d) fracture joint morphology of the metal side.

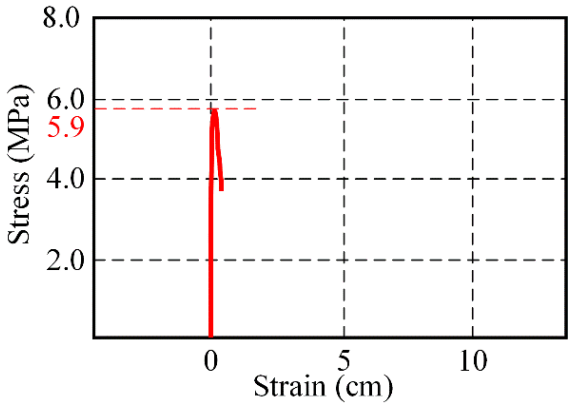

Fig. 5-9 Stress stain curved of the CFRP-SPCC joint that is based on FDM-manufactured micro-protrusions.

The final stress strain of the CFRP-SPCC joint based on FDM-manufactured micro-protrusions, as shown in Fig. 5-9, indicates that the maximum strength of the joint reaches approximately 6.6 MPa. Compared to joints between SPCC and CFRP directly bonded with resin, this joint exhibited a certain degree of strength enhancement. However, the strength enhancement is primarily attributed to the increased amount of resin between the carbon fiber plate and the metal plate, like the scenario presented in Fig. 5-4(e), where significant gaps exist between the metal plate and carbon fiber plate, and these areas were adequately filled with resin during the curing process. Consequently, the strength of the joint was also improved. This indicates that the increase in tensile strength of the joint cannot be solely attributed to the mechanical interlocking effect of the rose thorn-inspired micro-protrusions.

5.5 Joint Disassembly Process Evaluation Based on FDM-Manufactured Micro-Protrusions

The joint disassembly process can be illustrated in Fig. 5-10. Firstly, a separation fracture occurred between the metal and the CFRP sheet at the edge of the metal plate. This process involves the rupture of hydrogen bonding, i.e., the rupture that occurs after resin curing during the joining process. In this area, the performance of joints solely bonded by resin has been characterized in section 5.3. In this step, a fracture was first formed between the metal and carbon fiber plates, as shown in Step 1. Subsequently, the fracture gradually enlarges with external force, as shown in Step 2. With the continued increase in force, the crack eventually extended to the position of the micro-protrusions, and with further force, the carbon fiber plate was completely separated from the metal side, as shown in Step 3. This disassembly process reveals the joints' specific behaviors and performance characteristics during joining release, providing important references for their performance assessment and improvement.

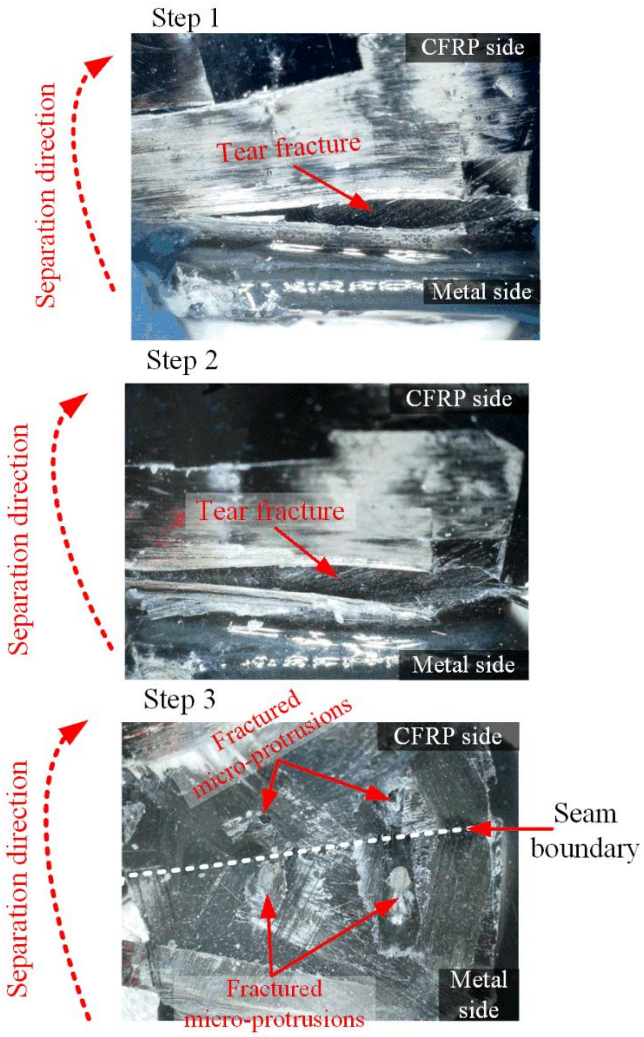

Fig. 5-10 Disassembly steps of the CFRP-SPCC joint based on FDM-manufactured micro-protrusions.

After disassembly, the morphology of the separated sides was first observed through an optical microscope. The purpose of observing the morphology of the disassembled parts is to determine the extent of damage caused to the materials during disassembly. In Fig. 5-11(a), the morphology of the metal plate side is displayed, showing carbon fiber bundles covering the surface of the metal plate as well as broken micro-protrusions during the tearing process. This indicates that the fracture did not occur in the resin region between the metal and the carbon fiber plate. Meanwhile, Fig. 5-11(b) displays the morphology of the torn carbon fiber side, revealing the occurrence of delamination in the carbon fibers. This delamination initially appeared during the joining process and was exacerbated during tearing disassembly. Due to delamination at this location, its performance deteriorated, leading to the progressive exacerbation of delamination and eventual failure at this location. This phenomenon highlights potential issues during the joining

process, which are significant for joint design and performance assessment.

The disassembled metal plate and carbon fiber plate morphology was subsequently observed using SEM to confirm the extent of material damage after disassembly. Fig. 5-12(a) shows the morphology of the carbon fiber side after disassembly, where embedded fractured micro-protrusions and tearing of the carbon fiber plate during disassembly can be observed. This indicates that the disassembly process caused damage to both the micro-protrusions on the metal surface and the carbon fiber plate. Fig. 5-12(b) presents the morphology of the metal plate side after disassembly, showing torn carbon fiber bundles on the metal plate surface, further indicating severe damage to the carbon fiber plate caused by the disassembly process. Additionally, broken micro-protrusions can also be observed on the side of the metal plate.

Subsequently, observations were made on the sectional morphology of the fractured micro-protrusions and their joining condition with the surrounding carbon fibers, as shown in Fig. 5-12(c) and (f), respectively. In these two images, the presence of spherical SUS 316L particles that remain spherical suggests that there were particles in the micro-protrusions manufactured based on FDM that were not completely melted, which may be related to the sintering temperature being only 1000 degrees Celsius. Moreover, a certain number of pores and even holes can be observed, further indicating that the micro-protrusions' performance significantly affects the joint's performance.

In Fig. 5-12(d) and (e), the connection between the fractured micro-protrusions and the surrounding carbon fibers is shown. No obvious defects are around them, which is consistent with the results of the previous analysis. This further indicates that the failure mode of the surface-structured metal and carbon fiber joint based on FDM is the delamination failure of carbon fibers at the joint rather than the failure at the interface with carbon fibers.

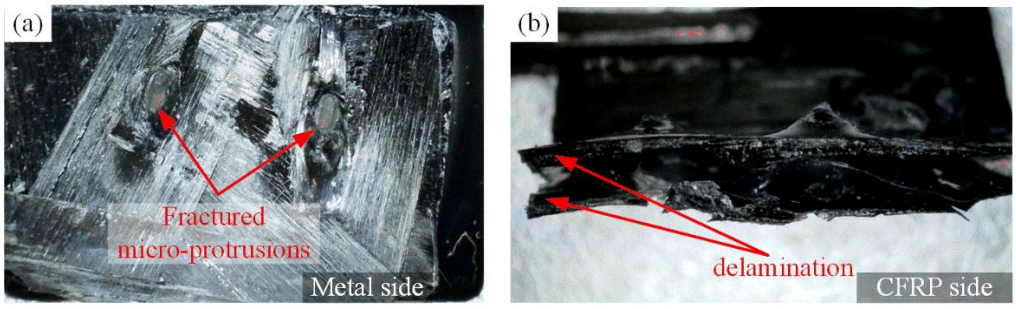

Fig. 5-11 Disassembled materials morphology: (a) metal side; (b) CFRP side.

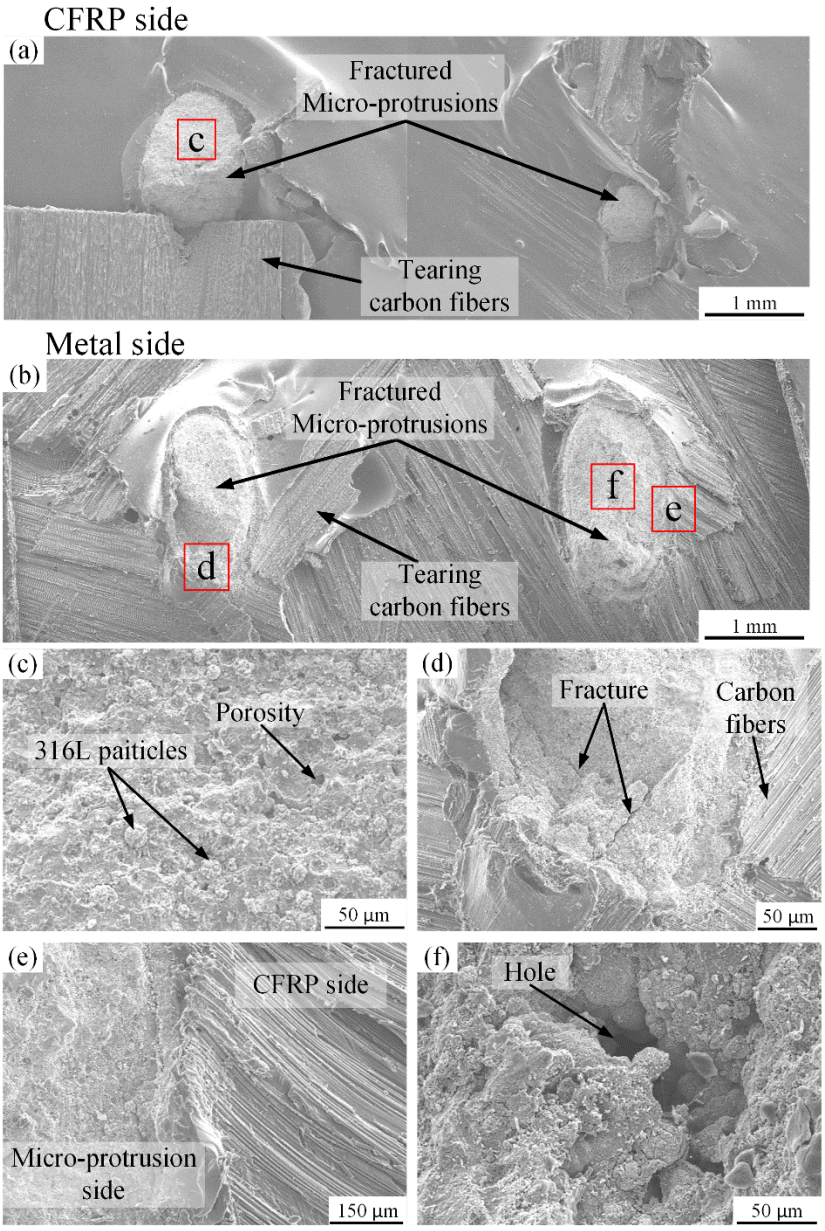

Fig. 5-12 The disassembled materials morphology under SEM: (a) CFRP side; (b) metal side; (c) fractural morphology of the c zone of the micro-protrusion in Fig. 5-12(a); (d) fractural morphology of the d zone of the micro-protrusion in Fig. 5-12(b); (e) fractural morphology of the e zone of the micro-protrusion in Fig. 5-12(b); (f) fractural morphology of the e zone of the micro-protrusion in Fig. 5-12(b).

5.6 Conclusions

This chapter primarily discusses the experimental process for connecting metals with carbon fiber using the FDM method for surface structuring and provides analysis and characterization of joint performance and disassembly processes. Based on the experimental results, we can draw the following conclusions:

1、Due to the lower accuracy and larger size of the FDM-manufactured micro-protrusion's tip, the penetration process of the CFRP sheet inevitably causes damage to the sheet.

2、Because the tip of the FDM-manufactured micro-protrusion has significant "stair" between layers, the CFRP sheet experiences substantial resistance when extending along the contour of the micro-protrusion, ultimately leading to incomplete adhesion to the metal substrate.

3、In the area where the CFRP sheet forms an effective joining with the micro-protrusion, microscopic observation showed no signs of defects such as cracks or pores, indicating high-quality connections in this region.

4、Tensile test results indicated that fractures occurred at the micro-protrusions, suggesting that the FDM method significantly impacts the performance of welded joints. When the mechanical properties of the micro-protrusions are inadequate, the welded joint tends to fracture at the micro-protrusions.

These results indicate that the FDM-manufactured rose-thorn structure has certain limitations in surface connection processes, highlighting the need to improve the manufacturing method to enhance joint performance.

Chapter 6: Manufacture of Rose Thorn Biomimetic Micro-Protrusions via Selective Laser Melting with a Low-Power Laser System

In this chapter, we employed Selective Laser Melting (SLM) technology to manufacture rose thorn biomimetic micro-protrusions on metal surfaces. Given that this study utilizes a low-power laser system with a maximum power of 30 W, we first investigated the interaction mechanisms and influencing factors between the low-power laser and SUS 316L particles.

6.1 Introduction

In this study, we conducted an in-depth investigation into the interaction between a low-power fiber laser (with a maximum average power of 30 W) and SUS 316L particles as well as the SPCC matrix, focusing on determining influencing factors such as laser average power density, laser peak power, original metal particle size, powder layer thickness, laser irradiation time, and powder bedding temperature. By systematically analyzing these parameters' impact on the manufacturing process and the related phenomena, we aimed to establish the groundwork for utilizing low-power lasers in creating millimeter-scale structures. Additionally, we explored the possibility of future optimization and enhancement, aiming to promote the widespread and efficient adoption of low-power lasers in laser additive manufacturing.

Additionally, we upgraded the design of a fully automated powder-spreading platform. This enhanced system offers increased manufacturing flexibility and advanced production automation, improving production efficiency and enabling more precise laser additive manufacturing. We examined the performance and applications of this integrated system in SLM, driving further development in laser additive manufacturing technology and offering innovative solutions for practical applications.

6.2 Experimental Procedures

6.2.1 Materials

This study employed Steel Use Stainless (SUS) 316L particles to fabricate the rose thorn-shaped micro-protrusions on the SPCC surfaces. SUS 316L particles have been considered to mitigate defects arising from excessive chemical composition differences during manufacturing. These particles served as the powder bedding material, aligning closely with the chemical composition of the SPCC. Table 6-1 provides the chemical composition details of the SUS 316L

particles. Additionally, this research utilized three different-grade particles: #10, #20, and #30, with nominal sizes of 10 μm, 20 μm, and 30 μm, respectively. These three particle types' morphology and size distribution are visually represented in Fig. 6-1.

Table 6-1 Chemical composition of SUS 316L particles (wt.%)

Chemical	Mo	Cr	Ni	Mn	Si	C	Fe
SUS 316L	2.08	17.25	12.56	0.70	0.84	0.017	Bal.

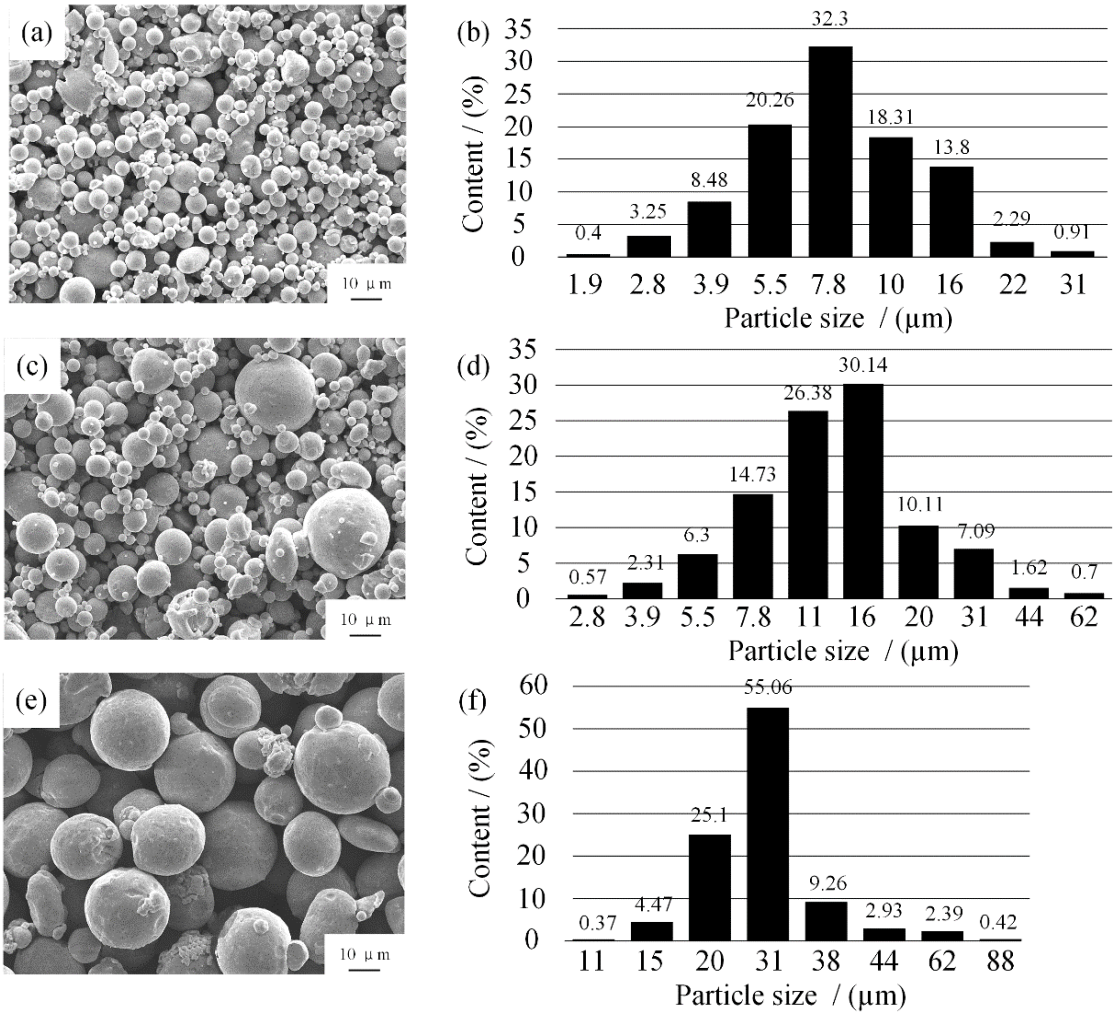

Fig. 6-1 SEM microphotographs of three-grade SUS 316L particles and size distribution: (a) grade #10 particles; (b) size distribution of grade #10 particles; (c) grade #20 particles; (d) size distribution of grade #10 particles; (e) grade #30 particles; (f) size distribution of grade #30 particles.

6.2.2 Experimental Instruments

a) Laser system

This study used a Ytterbium (Yb) fiber laser to melt SUS 316L particles. Renowned for its high efficiency and reliability, the Yb fiber laser was chosen for its suitability for precision manufacturing processes, thanks to its superior beam quality and stable output characteristics ideal for laser marking. The lower energy consumption and reduced operating cost make it a cost-effective solution. Detailed specifications of the Yb fiber laser system used in our experiments are provided in Table 6-2, encompassing laser power, wavelength, and pulse duration, among other parameters. With its advanced features and comprehensive specifications, the Yb fiber laser enables precise control over the melting process of SUS 316L particles, facilitating the fabrication of microscale structures with enhanced mechanical and physical properties.

Laser peak power refers to the maximum instantaneous power generated by a laser at the peak moment of a laser pulse. The peak power largely determines the melting depth and effect on the material. However, the peak power of the laser system is usually not directly displayed on the system interface, so it needs to be calculated. The laser peak power at different frequencies can be calculated using the laser system parameters listed in Table 6-2 and Formula 6-1. The calculation results are listed in Table 6-3.

$$P_{(pk)} = P_{(av)}/(f * t) \tag{6-1}$$

Table 6-2 Laser system parameters.

Laser type	**MD-F3200**
Average power	30 W
Scanning speed	1 mm/s ~ 12000 mm/s
Wavelength	1090 nm
Frequency	60 KHz ~ 120 KHz
Pulse width	60 KHz 100 ns
	80 KHz 90 ns
	100 KHz 80 ns
	120 KHz 70 ns

Table 6-3 The related peak power at different frequencies.

Maximum Average power ($P_{(av)}$)		Maximum Laser Peak power ($P_{(pk)}$)
30 W(100%)	60 KHz	5000 W
30 W(100%)	80 KHz	4167 W
30 W(100%)	100 KHz	3750 W
30 W(100%)	120 KHz	3571 W

b) Metal power cladding system

The accuracy of the automatic powder-spreading equipment plays a crucial role in the SLM process. The thickness of the powder layer is one of the key factors influencing the quality and performance of SLM manufacturing. To precisely control the powder layer thickness during the SLM process, we self-designed and constructed an automated powder spreading system, ensuring its capability to meet specific research requirements. This section will provide an introduction to this equipment.

This section first emphasizes the hardware components of the powder-spreading equipment required during the SLM process. Specifically, the schematic diagram of the powder spreading platform is shown in Fig. 6-2(a), which primarily includes three powder storage tanks, two micro-motors moving along the Z-axis direction, a scraper, and the full flighted screw of the scraper. The main frame of the platform was constructed using aluminum alloy, as illustrated in Fig. 6-2(b). Plastic encapsulation was applied on the foundation of the aluminum alloy main frame to ensure the platform's air-tightness during operation, as detailed in Fig. 6-2(c). Fig. 6-2(d) presents a physical schematic of the powder spreading platform, clearly indicating the positions of each component. Fig. 6-2(e) demonstrates the actual situation after placing SPCC workpieces and powder in the working area.

The powder-spreading platform was meticulously designed and constructed to ensure seamless coordination among its hardware components. The layout of three powder storage tanks, coupled with the scraper and full-flight screw combination, guarantees a uniform powder layer distribution. Moving along the Z-axis, two micro-motors enable precise positioning and motion control through a sophisticated system. The robust aluminum alloy main frame ensures structural strength and stability. Encapsulation with plastic maintains air-tightness and enhances corrosion and wear resistance, meeting specific requirements of the laser powder bed fusion process. These components' precision design and integrated structure support laser additive manufacturing,

establishing a reliable foundation for subsequent research and experiments.

At the software-controlled level, this system primarily involves two key aspects: the scraper's motion and the z-axis micro-stage's movement. The scraper moves along a linear trajectory, with relatively lenient requirements for motion speed and stroke. Therefore, the control of multiple scrapers is relatively simple, utilizing G-code scripts and the Universal Gcode Sender software.

However, for the movement of the z-axis micro-stage, a more precise control is required to ensure accurate powder layer thickness. This system employed the AMH-15 series stepper motors provided by the Japan Central Precision Industry as the power source for the z-axis micro-stage. Subsequently, this system utilized an Arduino circuit board and corresponding control code to control these micro-stages precisely**.** The control circuit scheme is as follows: the pulse signal used has a frequency of 2000 Hz, a duration of 400 microseconds for a single pulse, and a pause time of 100 microseconds, operating at a voltage of 5V. Specific parameters are illustrated in the figure below. The number of pulse signals generated has been experimentally validated to exhibit a basic linear relationship with the corresponding motor's displacement, as shown in the data presented in Fig. 6-3 below.

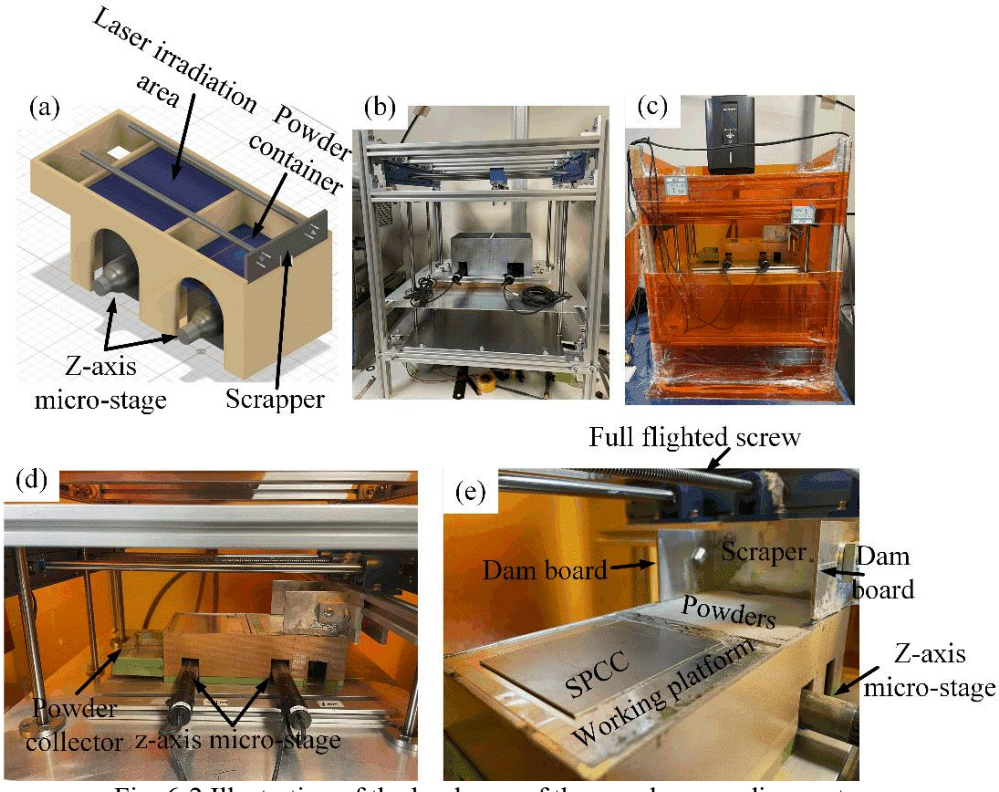

Fig. 6-2 Illustration of the hardware of the powder spreading system.

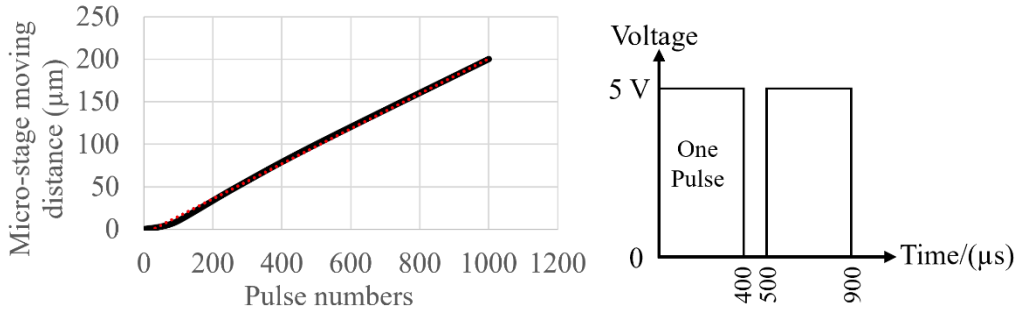

Fig. 6-3 Relationship between pulse numbers and micro-stage moving distance.

This precise control scheme ensures highly controllable movement of the z-axis micro-stage during the laser selective melting process, achieving accurate powder layer thickness control. Such meticulous control mechanisms provide a reliable foundation for laser additive manufacturing, ensuring precision and stability throughout the manufacturing process.

After the powder spreading process, the thickness of the obtained powder layer was initially measured. During the powder spreading, a scraper was employed to spread the powder from left to right for the first layer, covering the entire SPCC steel sheet and forming the first powder layer. Subsequently, the second layer was applied using 250 pulse signals, not completely covering the entire SPCC steel sheet to retain part of the first layer's thickness while preserving the second layer's thickness, resulting in some excess powder accumulation, as shown in Fig. 6-4(a). The process was repeated for the third layer, employing the same procedure as the previous step, generating 3 layers of powder. The third layer's powder spreading involved 500 pulse signals. Next, the fourth layer was applied with 1000 pulse signals. After the powder spreading, the SPCC steel sheet and its powder layers are illustrated in Fig. 6-4. At this point, the SPCC steel sheet bore multiple layers of powder generated by different pulse counts.

Subsequently, the obtained SPCC steel sheet and its powder layers underwent solidification treatment using epoxy resin, followed by cutting according to the red solid line pattern in Fig. 6-4(a). Fig. 6-4(b) depicts the resulting cross-section after cutting. Optical microscope observations were then conducted on regions c, d, e, and f in Fig. 6-4(b), and the obtained results are presented in Fig. 6-4(c), (d), (e), and (f).

We can substantiate the outstanding precision of the self-built powder spreading equipment through systematic measurement and analysis of the powder layer thickness obtained under different pulse numbers. The results indicate that this equipment can achieve uniform bedding of powder layers at the level of 50 μm, and it can also exhibit minimal thickness variations at the micrometer scale. This capability provides a reliable foundation for subsequent SLM operations.

The stability demonstrated during the powder spreading process ensures the consistency of material layers and provides a reliable process assurance for the subsequent stages of laser selective melting.

After the construction and verification of the powder bedding system, SLM experiments were immediately initiated, as illustrated in Fig. 6-5. In the experiments, the laser head was positioned at the top of the SPCC surface, and the laser beam radiated from the laser head, reaching the surface of the workpiece vertically. To maintain the purity of the experimental environment, the workpiece was placed in a nitrogen-filled protective box, with a gas flow rate maintained at 2 L/min. Thirty minutes before the start of the experiment, nitrogen was injected to purge the air inside the protective box. Detailed steps and conditions of the experiment will be further elaborated in subsequent chapters, providing a comprehensive presentation of our systematic investigation and precise control of the SLM process.

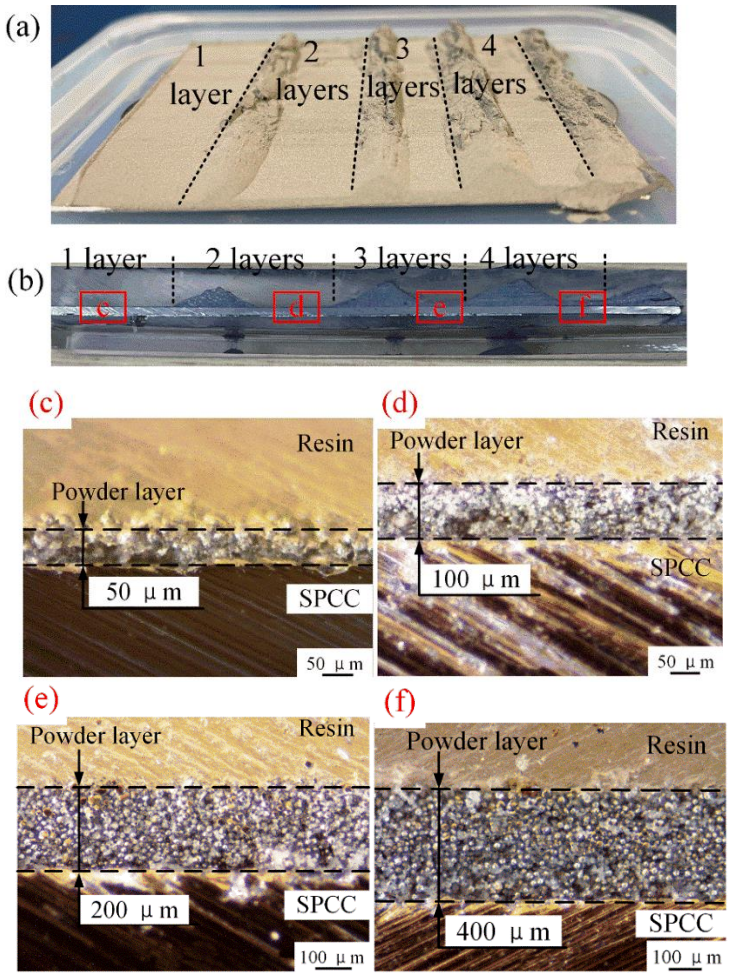

Fig. 6-4 Measurement of the powder layer thickness under different pulse numbers.

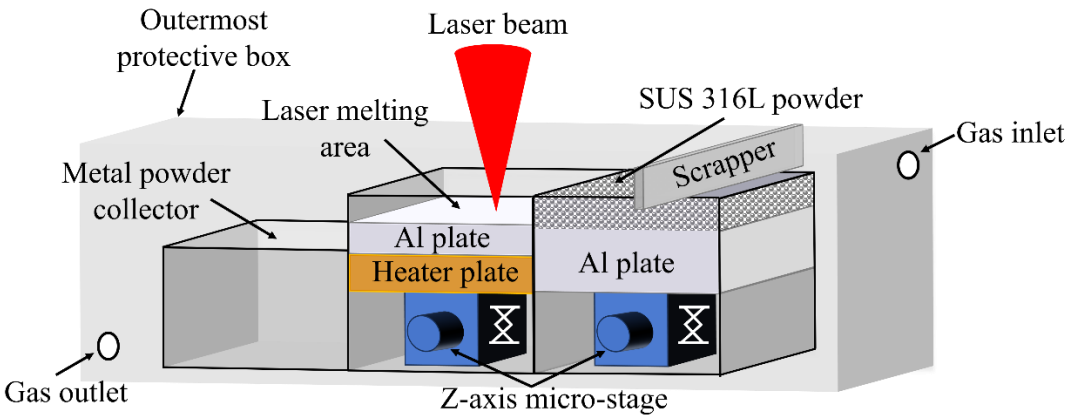

Fig. 6-5 Schematic diagram of the laser melting process and the equipment.

6.3 Influence of Laser Average Power Density

The laser average power density is a crucial parameter in the laser selective melting process. It is defined as the average laser power divided by the laser spot size. Power density indicates the amount of laser power per unit area, which measures the concentration of laser energy in the target area. It is typically used to evaluate the intensity of the laser and its interaction with the target object. However, most of the parameters used in current laser selective melting experiments are average power, not power density [161, 162]. Therefore, in this study, we first analyzed the impact of average laser power density on SUS 316L particles.

6.3.1 Calculation of Laser Average Power Density

Despite being known for high directionality, laser beams also have a certain natural divergence angle. This divergence angle is quite small, but as the propagation distance of the laser increases, the effect of divergence becomes more noticeable, leading to an expanded spot area, as shown in Fig. 6-6, which in turn affects the laser's average power density. The formula for calculating the laser power density is as follows:

$$I = \frac{E}{S} \tag{6-2}$$

where E is the average power of the laser beam, and S is the laser spot area. Therefore, measuring the laser spot size under different laser beam lengths is essential for calculating laser power density.

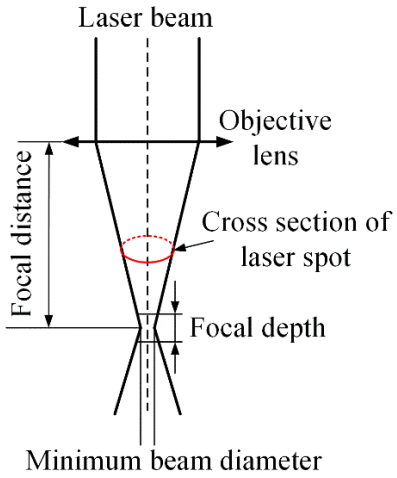

Fig. 6-6 Schematic diagram of the laser beam divergence.

The energy distribution on the laser spot is not uniform; instead, it exhibits a Gaussian curve characteristic, as shown in Fig. 6-7(a). Thus, in this study, the method for defining the size of the laser spot differs from traditional methods such as pinhole or diffraction pattern measurements. A more straightforward approach is used, which involves observing the interaction results between the laser and the metal material used in the experiment. Fig. 6-7(b) illustrates the outcome of the laser beam's interaction with the SPCC surface, and Fig. 6-7(c) depicts the three zones of this interaction region: the innermost laser spot zone, the central fusion zone, and the outermost heat-affected zone. Each region can be approximately considered as different shaped ellipses, facilitating the subsequent calculation of the corresponding area's size.

The interaction results between the laser and SPCC shown in Fig. 6-7 show that the actual melted region is larger than the actual laser spot size. Therefore, in this experiment, the melted trace left by the laser and substrate interaction is defined as the size of the laser spot, that is, the area within the fusion zone. Furthermore, to measure the size of the laser spot at different laser beam lengths, as the laser spot size at the same position is independent of the emitted energy, the experiment used a 20 W power to measure the size of the laser spot to obtain an accurate measurement.

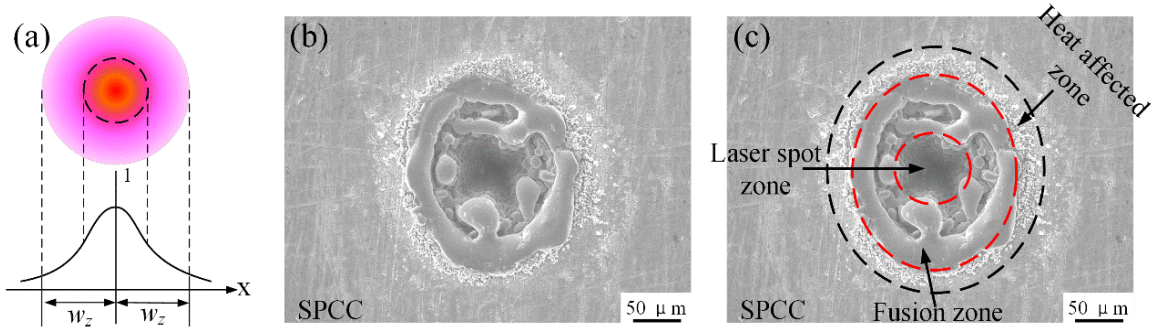

Fig. 6-7 Laser spot power distribution and real effect on SPCC surface: (a) Gaussian energy distribution of the laser spot; (b) laser effect on the SPCC surface; (c) different zone definition of the laser spot.

Based on our preliminary experimental results, the working distance between the laser lens and the SPCC surface is measured from 300 mm, because at this distance, the laser begins to cause significant chemical reactions with the metal surface, rather than just heat accumulation. At this point, the melting marks that appear on the SPCC surface are more likely caused by thermal effects, as shown in Fig. 6-8(a). When the laser working distance is increased to 360 mm, effective laser spot marks cannot be obtained on the SPCC surface, as shown in Fig. 6-8(h). Therefore, it can be concluded that the effective working distance for this laser system for melting metal particles is between 310 mm and 350 mm.

Figs. 6-8(b) to 6-8(g) display the melting marks left by the laser beam at distances between 300 mm and 350 mm. The red dashed box indicates the laser spot's effective area, which was measured using ImageJ software. Within this area, high-energy laser radiation caused the metal plate to melt. This phenomenon is considered a fundamental energy requirement in the SLM process. If the metal particles do not melt, the SLM process cannot proceed.

Fig. 6-8(b) shows the melting marks left on the SPCC surface when the laser working distance is 310 mm. At this point, the primary diameter of the laser spot is about 255 micrometers. As the laser working distance increases, the laser spot diameter gradually decreases, and the melting marks become more pronounced. When the working distance reaches 320 mm, the primary diameter is approximately 220 μm, as shown in Fig. 6-8(c). Additionally, a "pitting" shape appears at the center of the laser radiation area, indicating that partial evaporation of the metal occurred in this region.

When the laser working distance is increased to 325 mm, the diameter of the laser spot is about 190 μm, and the melting pit is deeper, with a cone-shaped melting hole appearing in the center of the SPCC. This indicates that the increased laser power density significantly impacts the metal. When the laser working distance is increased to 330 mm, the laser spot diameter increases

again, as shown in Fig. 6-8(e). This suggests that the laser working distance exceeds the focal length, but the laser energy density is still sufficient to melt and even evaporate the surface metal. Fig. 6-8(f) shows the melting marks left on the SPCC surface when the laser working distance reaches 340 mm, with the laser spot diameter being about 265 μm. Finally, when the laser working distance is increased to 350 mm, the results are shown in Fig. 6-8(g). At this point, the effective length of the laser spot is about 300 μm, and the melting marks on the SPCC surface are still quite pronounced, while the central region's pitting phenomenon has disappeared.

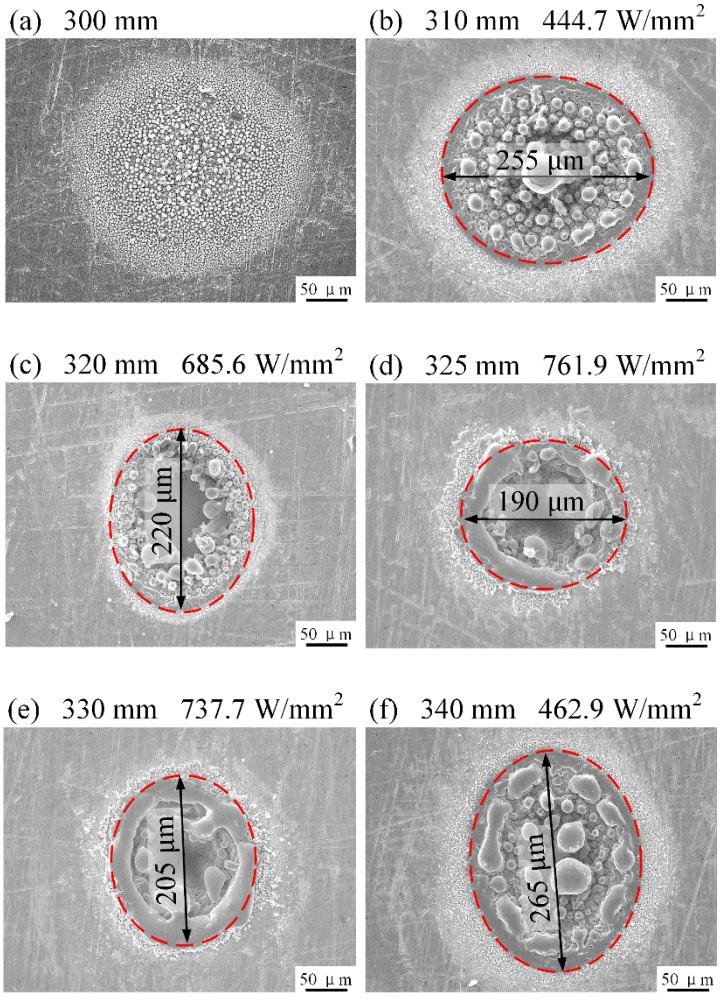

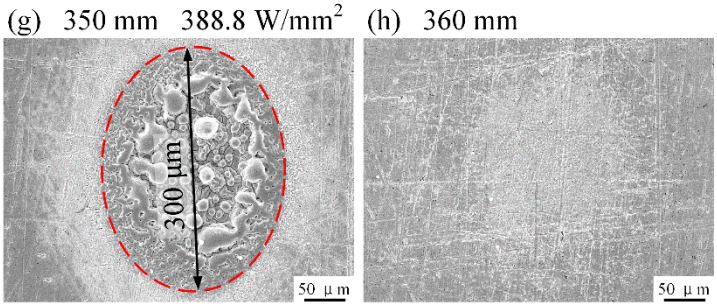

Fig. 6-8 Laser spot diameter at different laser working distances: (a)300 mm; (b)310 mm; (c)320 mm; (d)325 mm; (e)330 mm; (f)340 mm; (g)350 mm; (h)360 mm.

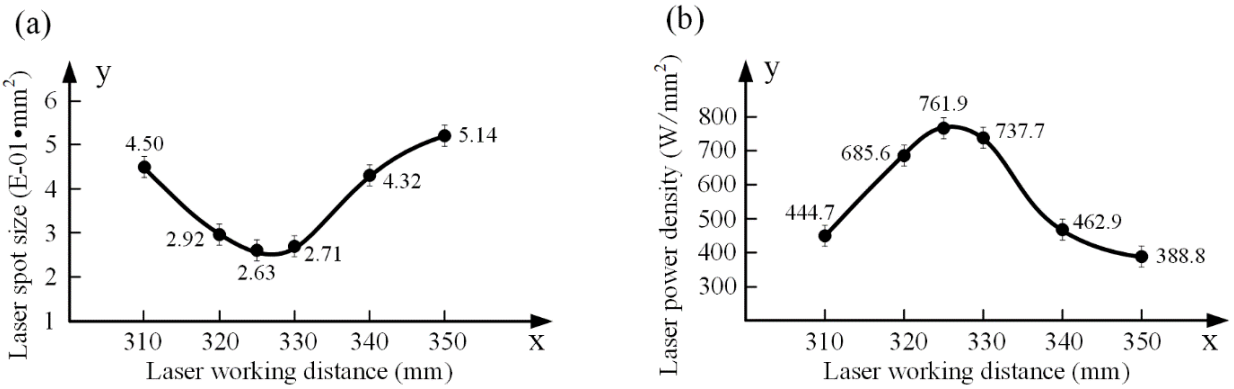

Fig. 6-9 Relationship between laser working distances and laser spot area: (a) laser spot size; (b) laser power density.

The above analysis found that this laser system's efficient working distance that can melt the SPCC surface ranged from 310 mm to 350 mm. If the laser working distance exceeds this range, the SPCC surface only generates heat but does not melt. This means only in this range does the laser power density have enough energy to melt the particles and fabricate the micro-protrusion structures on the SPCC surface. Fig. 6-9 shows the variation tendency of the laser spot size and the laser power density at different laser working distances. The laser spot area decreased first and then increased with the increase of the laser working distance, while the laser power density had the opposite tendency. The calculation result shows that this laser system's process window is around between 380 W/mm^2 to 760 W/mm^2.

6.3.2 Experimental Results and Discussion

Based on the previously calculated laser power density, we first investigated the interaction between lasers and SUS 316L metal powders at different power density levels. By observing and analyzing the experimental results of the laser's interaction with SUS 316L under varying average

laser power densities, we identified several distinct phenomena that can be summarized as follows.

a) Out-of-situ formation phenomenon

The out-of-situ formation of the micro-protrusions phenomenon occurred in tests 1 and 2, and the corresponding experimental parameters are listed in Table 6-4. It presented that the formed micro-protrusions did not stay at the laser irradiation position but outside it, as shown in Fig. 6-10(a) and Fig. 6-10(d). By analyzing the parameters of tests 1 and 2, it is found that the original particle size, powder bedding thickness, and laser power density are the same, and their value is 10 μm, 50 μm, and 444.7 W/mm^2, respectively. The only different parameter is the laser irradiation time, which is 1 s and 5 s, respectively.

Fig. 6-10 shows micrographs of the dislocated forming phenomenon taken by a SEM. Due to the relatively low average laser power density, this significantly reduces the amount of melted material. Consequently, in Figs. 6-10(a) and 6-10(d), it can be observed that no melting marks appear on the SPCC surface, indicating that the structures formed under laser irradiation could not achieve metallurgical bonding with the metal substrate. This insufficient melting causes the formed structures to move to the periphery of the laser irradiation area under the laser force instead of remaining within the laser-irradiated region. By observing the formed structures, we can see that the original metal particles did not fully melt during manufacturing, regardless of whether the laser exposure time was 1 s or 5 s. This suggests that the dislocated forming phenomenon is not related to the laser exposure time. In Figs. 6-10(c) and 6-10(f), some partially melted SUS 316L particles can be seen on the surface of the micro-protrusions. This further indicates that inadequate laser average power density can lead to insufficient melting of the metal particles.

Table 6-4 Experimental parameters of test 1 and test 2.

Test number	Particle size (μm)	Powder bedding thickness (μm)	Laser working distance (mm)	Laser power density (W/mm^2)	Laser irradiation time (s)
1	10	50	310	444.7	1
2	10	50	310	444.7	5

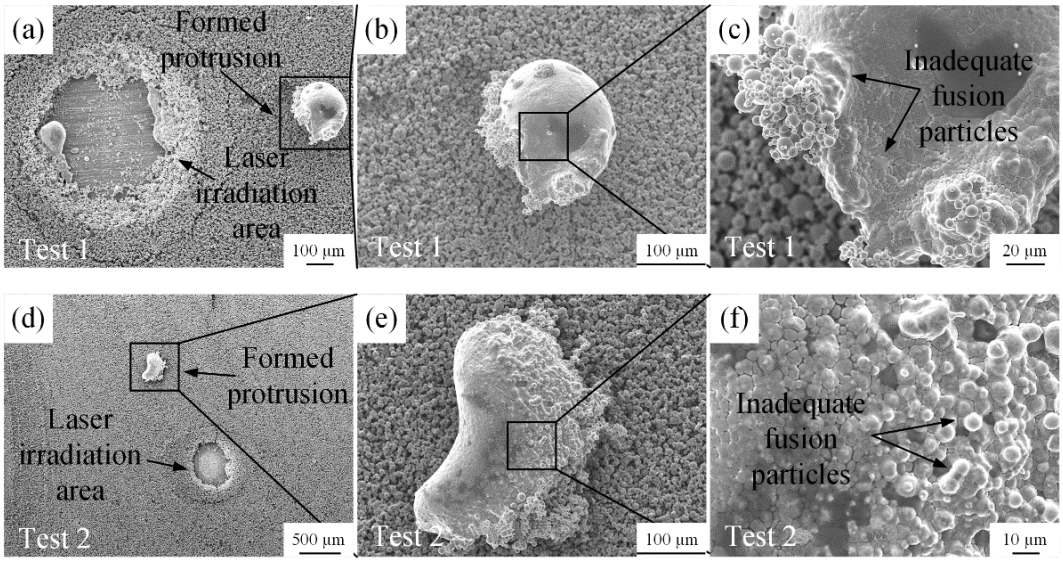

Fig. 6-10 Out-of-situ formation phenomena: (a) test 1 at 100x magnification; (b) test 1 at 250x magnification; (c) test 1 at 700x magnification; (d) test 2 at 30x; (e) test 2 at 250x; (f) test 2 at 1000x.

b) Generation of impurities substance

When the laser working distance is increased to 320 mm, the average laser power density reaches 685.6 W/mm². Other experimental parameters remained unchanged, as indicated in Table 6-5. From a macroscopic perspective, the experimental results show a layer of black material on the surface of the unmelted powder, as depicted in Fig. 6-11(a). This black material does not form in the areas directly irradiated by the laser but instead appears around the already-formed micro-protrusions. Through SEM observation, this black material appears as a layer of opaque glass covering the top of the powder layer, as shown in Figs. 6-11(b) and 6-11(c).

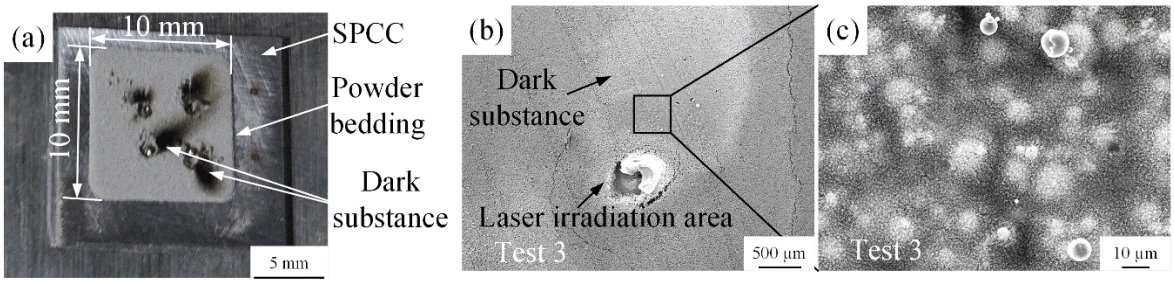

Fig. 6-11 SEM microphotographs of the dark substance: (a) 50x magnification; (b) 1000x magnification.

Table 6-5 Experimental parameters of test 3

Test number	Particle size (μm)	Powder bedding thickness (μm)	Laser working distance (mm)	Laser power density (W/mm^2)	Laser irradiation time (s)
3	10	50	320	685.6	1

When the working distance of the laser is extended to 330 mm, the corresponding average laser power density reaches its maximum value of 761.9 W/mm². We experimented with different coating layer thicknesses at this laser power density, with specific parameters provided in Table 6-6. Fig. 6-12 shows that at this maximum average laser power density, the laser pierces the SPCC surface within 1 second, creating a deep hole. This indicates that this level of laser power density is sufficient to melt and even evaporate the metal. Based on this observation, the formation of dark material is primarily related to excessively high laser power density. Under high power density, SUS 316L metal particles are evaporated and deposited on top of the powder layer, forming dark material. This dark material formation is mainly due to the evaporated metal particles oxidizing with oxygen in the air under high-temperature conditions, resulting in an oxide layer. This oxide layer typically appears black and resembles frosted glass under the SEM.

Therefore, material evaporation and oxidation caused by excessively high laser power density are the main reasons for the presence of dark material around the laser irradiation area. This phenomenon is significant in the SLM process, as it reveals the potential impact of high power density on material structure and surface quality. Understanding this phenomenon is crucial for ensuring the stability of the SLM process and the quality of the final product.

Table 6-6 Experimental parameters of tests 4, 5, 6

Test number	Particle size (μm)	Powder bedding thickness (μm)	Laser working distance (mm)	Laser power density (W/mm^2)	Laser irradiation time (s)
4	10	50	330	761.9	1
5	10	100	330	761.9	1
6	10	200	330	761.9	1

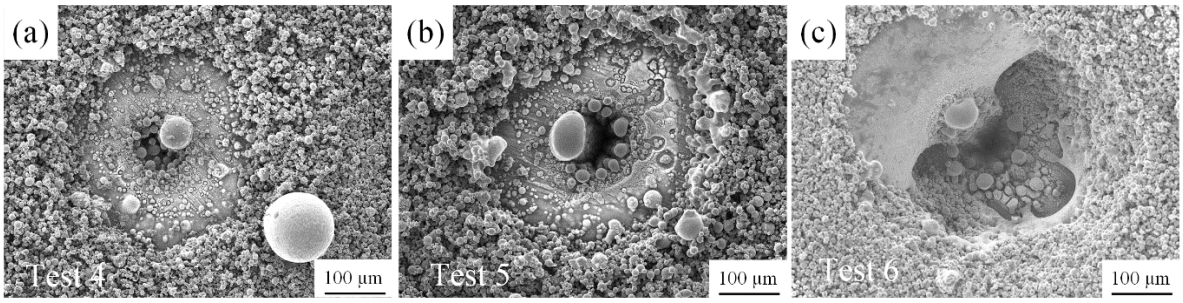

Fig. 6-12 Micro-protrusion formation at the highest laser power density: (a) test 4 at 200x magnification; (b) test 5 at 200x magnification; (c) test 6 at 200x magnification.

6.4 Influence of Laser Peak Power

The previous section mainly examined the effect of average laser power density on SUS 316L. In pulsed lasers, the frequency of laser pulses is also a key factor affecting the SLM process. This parameter can be directly viewed and adjusted on the laser equipment, so many researchers often use laser frequency as a significant parameter in SLM studies. However, in this study, we consider the core role of laser pulse frequency to be its impact on laser peak power. Laser peak power represents the instantaneous power of the laser beam per unit area, reflecting the concentration of energy, directly influencing the instant melting and evaporation of materials. Higher laser peak power density usually leads to rapid melting and even evaporation, which is beneficial for precise manufacturing and the formation of fine structures. However, excessive peak power density can cause issues like ablation, spatter, and surface roughness. In this study, we delve into the effect of laser peak power on the metal particle melting process and emphasize the importance of controlling peak power density in the SLM process. Optimizing this parameter contributes to achieving high-quality laser melting and a stable production process.

Table 6-3, section 6.2.2, shows that different pulse frequencies correspond to different laser peak power in laser system parameters. Therefore, this section first investigates the influence of laser pulse frequency on the metal additive manufacturing process. A laser with an average power of 30 W, a frequency of 60 KHz, corresponding to a laser peak power of 5000 W, and a parameter combination of 1 mm/s were used for additive manufacturing. The corresponding powder layer thickness was 50 micrometers, and the nominal size of the particles was 10 μm. The obtained results are shown in Fig. 6-13.

Fig. 6-13(a) and (b) show the SPCC substrate after the removal of un-melted SUS 316L particles. The current melted particles forming exhibit a spherical or nearly spherical structure, indicating that the melt-forming results of metal particles are not improved under this laser

parameter combination. Spherical forming leads to weaker bonding between the metal substrate and, during SEM observation after the removal of un-melted particles, may simultaneously remove the formed spherical structures. This section temporarily does not discuss the formation of spherical structures but focuses on the state of the metal substrate.

After irradiation with the laser parameter combination mentioned above, numerous small holes form on the SPCC surface, and these holes interconnect to create an effect similar to cutting. This phenomenon can be explained by the excessive focusing of laser energy and a too high peak power density, resulting in intense melting and evaporation of the local area on the SPCC surface. However, the presence of these cutting holes is likely to have a significant adverse effect on the mechanical and physical properties of the metal substrate. This further emphasized the necessity for precise control of laser parameters in laser additive manufacturing to achieve the desired metal structure and maintain its integrity.

Subsequently, we adjusted the pulse frequency to 80 KHz while maintaining other laser power parameters constant. At this point, the corresponding laser peak power is 4167 W. At this frequency, the observed phenomenon on the SPCC surface was characterized by the appearance of small holes no longer in a continuous state but rather as individual, independent single holes. Detailed observations are shown in Fig. 6-14.

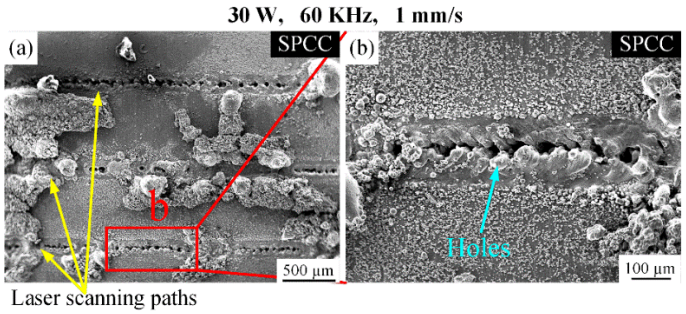

Fig. 6-13 Holes phenomenon on the SPCC substrate shocked by 30 W, 60 KHz, 1 mm/s parameters.

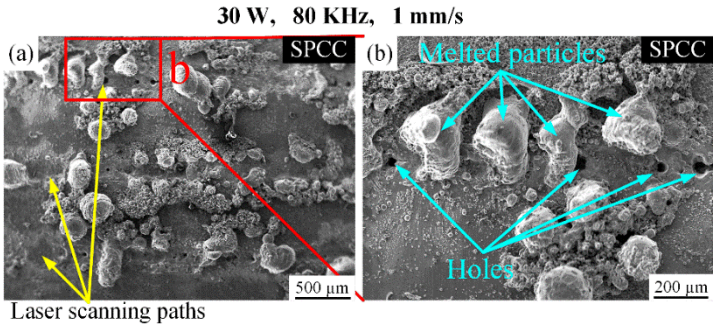

Fig. 6-14 Holes phenomenon on the SPCC substrate shocked by 30 W, 80 KHz, 1 mm/s parameters.

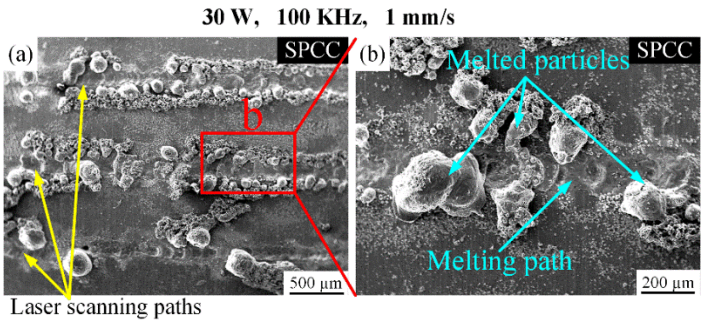

Fig. 6-15 Forming result on the SPCC substrate shocked by 30 W, 100 KHz, 1 mm/s parameters.

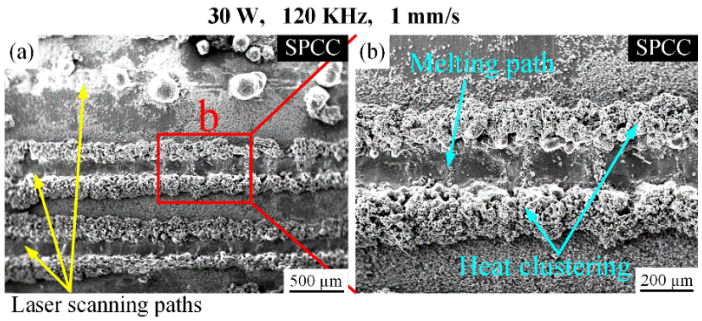

Fig. 6-16 Forming result on the SPCC substrate shocked by 30 W, 120 KHz, 1 mm/s parameters.

When the laser frequency increases to 100 KHz, the corresponding research results are shown in Fig. 6-15. In this scenario, the laser system achieves a peak power of 3750. Notably, under these conditions, the SPCC surface no longer exhibits the hole but instead shows characteristics of surface melting. This observation indicates that reducing the laser peak power density effectively avoids perforation of the metal substrate. The selection of this laser peak power density has been demonstrated to be relatively appropriate in subsequent experiments.

However, merely reducing the peak power density of the laser does not necessarily imply a significant improvement in the protective effect on the SPCC substrate. When the laser frequency increased to 120 KHz, the corresponding peak power reached 3571 W. This result is shown in Fig. 6-16. Under these conditions, as the laser's peak power density decreases, the localized accumulation of metal particles around the laser scanning path exhibits a thermal clustering phenomenon. The occurrence of thermal clustering indicates lateral dispersion of laser energy in the working area, suggesting a decrease in the laser's effectiveness in the longitudinal direction. However, excessively low energy may result in insufficient melting of the SPCC surface, preventing the formation of a well-metallurgically bonded micro-protrusion on its surface, leading to the unstable presence of the formed structure on the metal surface.

In summary, adjusting the laser's peak power requires a comprehensive consideration of its

influencing factors to find the optimal balance point. This ensures that there is sufficient energy during the metal additive manufacturing process to ensure complete melting while avoiding excessively high energy that leads to lateral thermal clustering and reduced longitudinal effectiveness. This approach enhances the stability of the manufactured structure on the metal surface and improves the metallurgical bonding quality.

6.5 Conclusions

In this chapter, we conducted Selective Laser Melting (SLM) experiments with a low-power laser using a self-built powder bed setup and analyzed the effects of key laser parameters on SUS 316L particles. Through experimental observations and analytical results, we reached the following conclusions:

1、The average laser power density significantly impacts the melting of metal particles. Low power density can lead to insufficient melting of the metal particles, affecting the quality of the SLM process.

2、Excessive average laser power density may cause the evaporation and oxidation of metal particles, which not only introduces impurities on the surface of the powder bed but could also lead to quality issues with the workpiece.

3、The pulse frequency of the laser affects the peak power density. Excessively high peak power density may result in effects similar to cutting, which can compromise the continuity and stability of the SLM process.

4、There are two methods to reduce the laser peak power density: lowering the average power or increasing the laser frequency. However, merely lowering the average power could lead to insufficient melting of the metal particles, so a balance must be struck between reducing peak power and ensuring adequate melting.

These findings underscore the importance of controlling laser power density in the SLM process. By optimizing laser parameters, sufficient melting of the metal particles prevents excessive evaporation and oxidation, thereby improving the SLM process's stability and the final product's quality.

Chapter 7: Joint Mechanical Properties and Disassembly Process Evaluation Based on SLM-Manufactured Biomimetic Micro-Protrusions

7.1 Introduction

Chapter 6 experimented with a low-power pulsed laser system and a self-built powder bedding platform for SLM, but this approach did not yield the desired rose-thorn-shaped micro-protrusions in my experiments. Consequently, to investigate the working conditions of rose thron that fabricated by the SLM, we collaborated with the ORIX Rentec in Japan to produce the rose-thorn biomimetic micro-protrusions, still using the SLM method and the same designed shape. The resulting shapes and dimensions of the micro-protrusion are illustrated in Fig. 7-1. Building upon this achievement, this chapter further investigates the joining and disassembly challenges between surface-structured SPCC and epoxy resin-infused chopped CFRP, providing a comprehensive analysis of joint performance and the disassembly process.

7.2 Experimental Procedures

In Chapter 7, the materials, joining method, and disassembly method remain consistent with those described in Section 5.2, with detailed information available.

7.3 Joint Morphology Analysis Based on SLM-Manufactured Micro-Protrusions

Firstly, a macroscopic analysis of the joint morphology was performed. Fig. 7-2 presents the results of the joint at different positions and stages under an optical microscope. Special attention was paid to the joint's upper surface and left side. Fig. 7-2(b) shows the upper surface result before resin curing, following the insertion of the tips of the micro-protrusions fabricated by SLM into the chopped CFRP sheet. The presence of micro-protrusions' tip can be observed, but no fracture of the surrounding carbon fibers occurred. In Fig. 7-2(c), the results after completion of the joining and resin curing are shown without any damage occurring during this process. Fig. 7-2(d) illustrates the morphology of the left side of the joint after completion of the joining but before resin curing. Unlike the micro-protrusions manufactured using FDM methods, those prepared using the SLM method demonstrated a good fit between the SPCC plate and the CFRP sheet during the joining process. Finally, Fig. 7-2(e) shows the left-side morphology of the joint after resin curing, indicating that the cured resin effectively filled the tiny gaps between the SPCC plate and the CFRP sheet, forming a slight resin bulge externally.

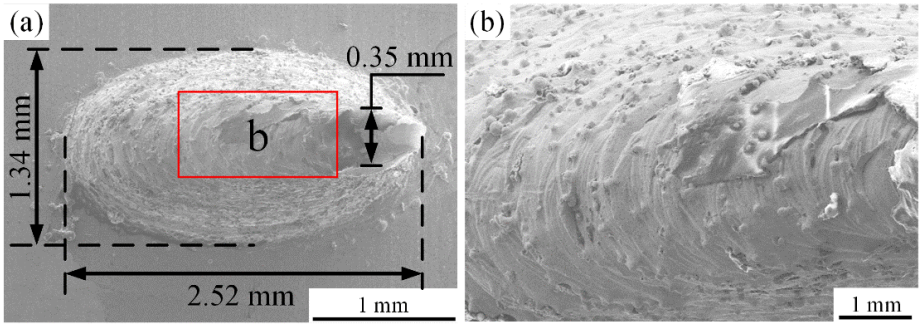

Fig. 7-1 The rose thorn biomimetic micro-protrusion fabricated by the ORIX Rentec Corporation.

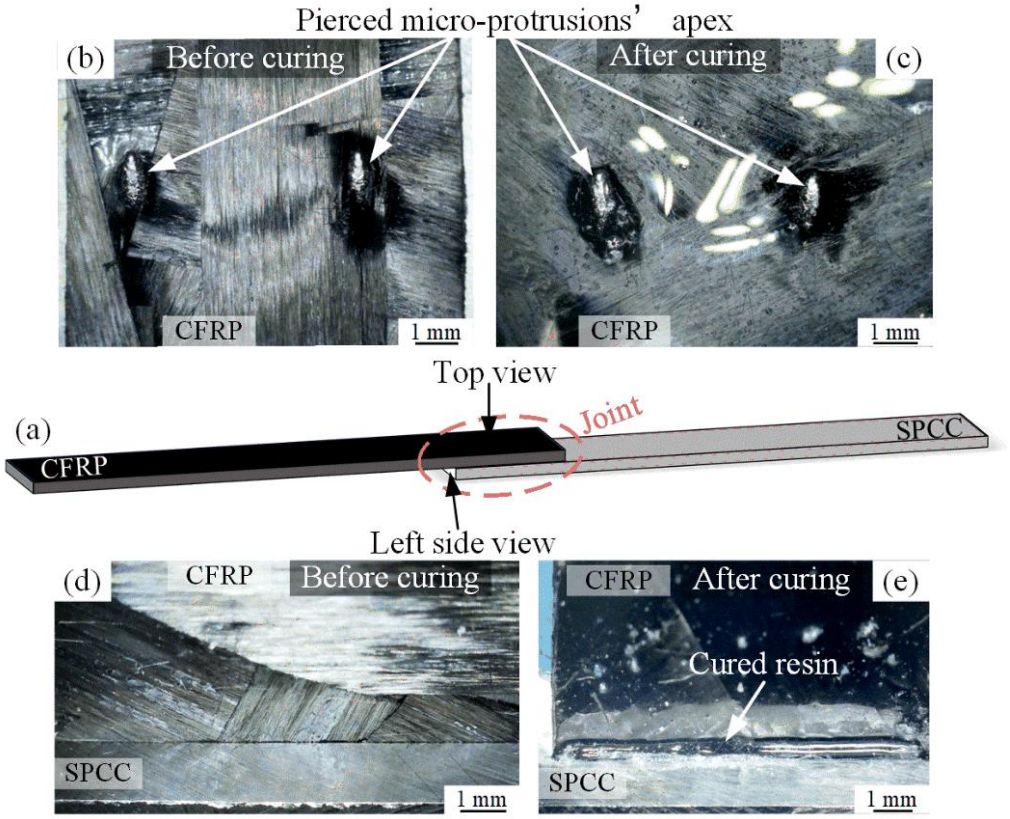

Fig. 7-2 Joint morphology based on SLM: (a) diagram of the joint positions; (b) joint top surface morphology before epoxy resin curing; (c) joint surface morphology after epoxy resin curing; (d) joint left side view before epoxy resin curing; (e) joint left side view after epoxy resin curing.

Fig. 7-3 illustrates the top surface morphology of the joint under SEM. In Fig. 7-3(a), the penetration of the micro-protrusions into the CFRP is clearly shown, with the tip passing through the gap between the carbon fibers. Notably, as the more micro-protrusion volume penetrates, the carbon fibers are squeezed to the sides, resulting in a uniform arrangement surrounding the micro-protrusion. However, throughout the process, there was no apparent breakage or damage to the carbon fibers, which is markedly different from previous results illustrated in Section 5.3. Upon

magnification of regions b and c on either side of the micro-protrusion, it can be observed that the carbon fibers in these regions uniformly encircle the micro-protrusion without any signs of fracture. This outcome is depicted in Fig. 7-3(b) and (c), respectively.

Fig. 7-4 illustrates the vertical sectional morphology of the joint, providing a clearer view of the joining between the surface-structured SPCC and CFRP. Fig. 7-4(a) presents an image obtained under an optical microscope, clearly showing the spatial relationship between the metal plate and CFRP sheet within the joint. This spatial relationship remains consistent with the initial design schematic of the joint, as shown in Fig. 3-5, indicating successful macroscopic joining. To further investigate the joining effect between the surface-structured SPCC and CFRP, SEM observations were conducted on four regions (c, d, e, f) in Fig. 7-4(b), representing different parts of the joint. The specific results are shown in Fig. 7-4(c), (d), (e), and (f), respectively. In regions d and e, close contact was observed between the micro-protrusion and carbon fibers. However, a certain amount of resin was found at the base of the micro-protrusion's outer and inner contours. Despite the presence of resin in these areas, no defects were detected in any of the four regions.

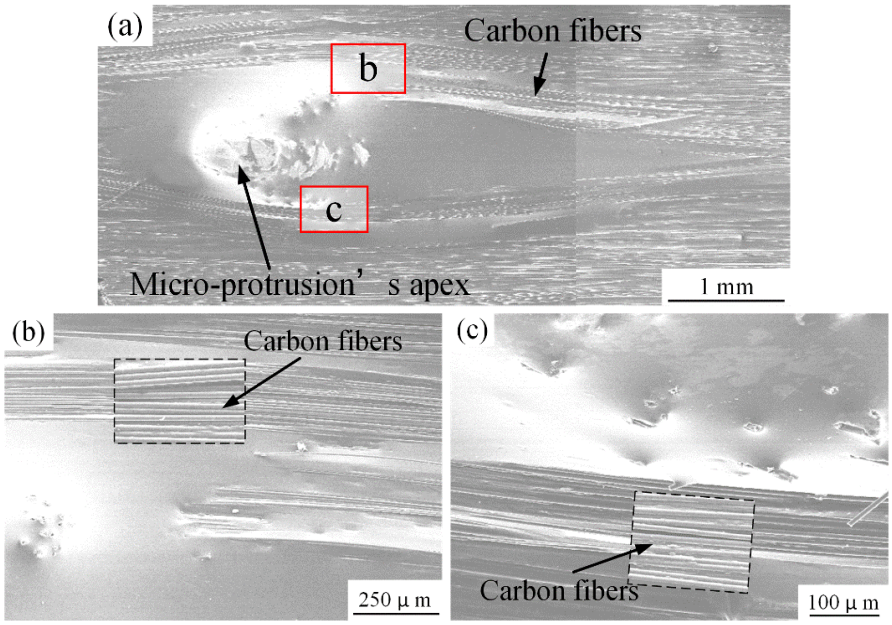

Fig. 7-3 Joint morphology based on SLM: (a) top surface under SEM; (b) magnification of the region b in Fig. 7-3(a); (c) magnification of the region c in Fig. 7-3(a).

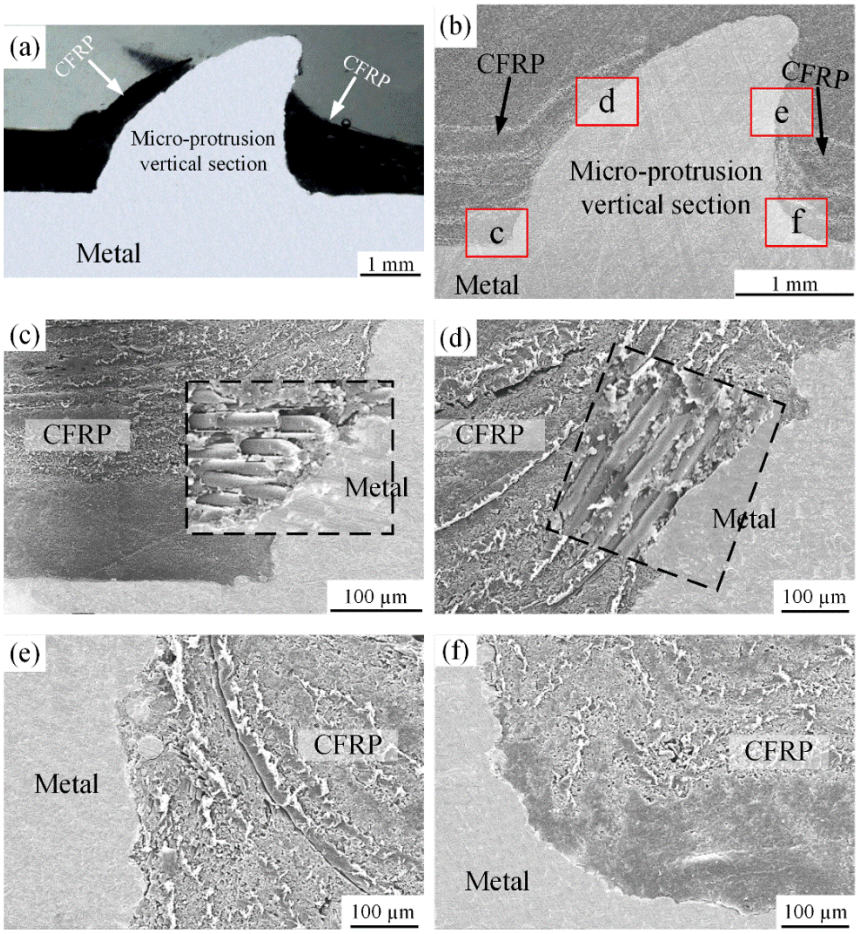

Fig. 7-4 Joint vertical section microstructures based on SLM: (a) joint vertical section under the optical microscope; (b) joint vertical section under SEM; (c) magnification of zone c in Fig. 7-4(b); (d) magnification of zone d in Fig. 7-4(b); (e) magnification of zone e in Fig. 7-4(b); (f) magnification of zone f in Fig. 7-4(b).

The morphology results of a horizontal section of the joint are presented in Fig. 7-5. In Fig. 7-5(a), a small hole was observed over the left-up side; however, this hole is attributed to accidental damage to the CFRP sheet during the sample grinding process and is unrelated to the joining process. Three different areas were further selected for SEM observation. The results are shown in Fig. 7-5(b), (c), and (d). In these areas, carbon fibers exhibit regular and orderly arrangements, and no holes or defects were observed at the boundary between carbon fibers and SPCC. This indicates that on the horizontal section of the joint, the joining effect between the micro-protrusion and carbon fibers was good and consistent, with no apparent structural defects.

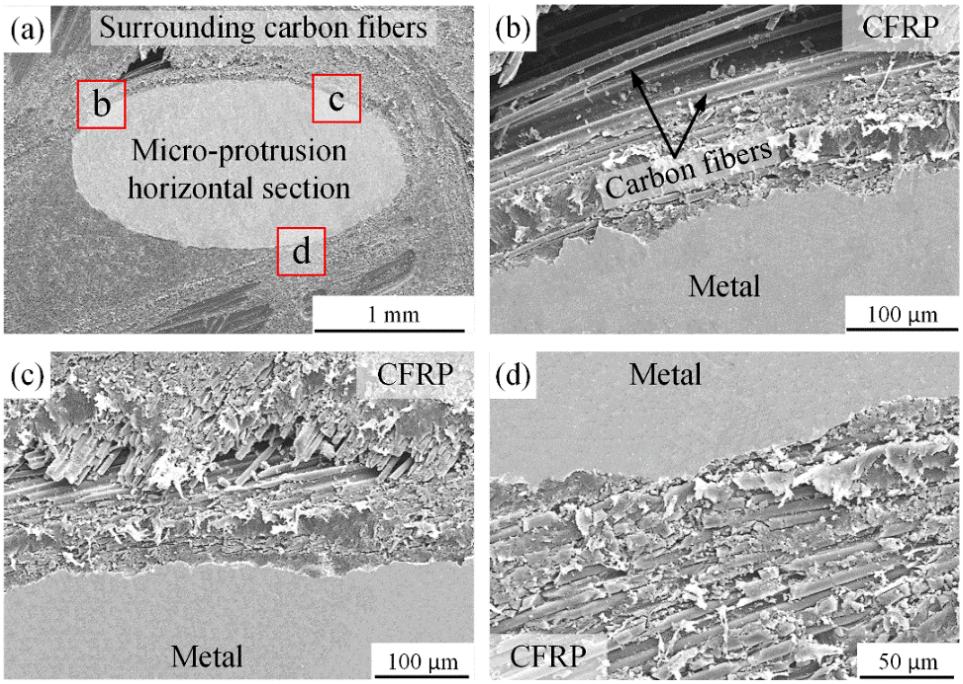

Fig. 7-5 Middle horizontal section view of the joint based on SLM: (a) joint morphology under SEM; (b) magnification of zone b in Fig. 7-5(a); (c) magnification of zone c in Fig. 7-5(a); (d) magnification of zone d in Fig. 7-5(a).

7.4 Joint Mechanical Properties Analysis

According to the results shown in Fig. 7-6, the joint of CFRP-SPCC that surface structured based on SLM manufacturing demonstrates satisfactory performance. Observation of the fracture location reveals that the ultimate fracture occurs at the epoxy resin-infused chopped CFRP sheet, indicating that the strength of the welded joint formed by this joining method exceeds that of the epoxy resin-infused chopped CFRP sheet itself. Specifically, Fig. 7-6(a) provides a schematic diagram of the fracture location, while Fig. 7-6(d) exhibits the surface morphology of the fracture location, where the presence of the CFRP sheet and the micro-protrusions in the joint area was observed. These results further validate the effectiveness of the micro-protrusions manufactured using SLM on the metal surface, indicating its good strength and reliability to withstand certain tensile loads, thereby directing the fracture of the joint to concentrate on epoxy resin-infused chopped CFRP sheet rather than the joint itself.

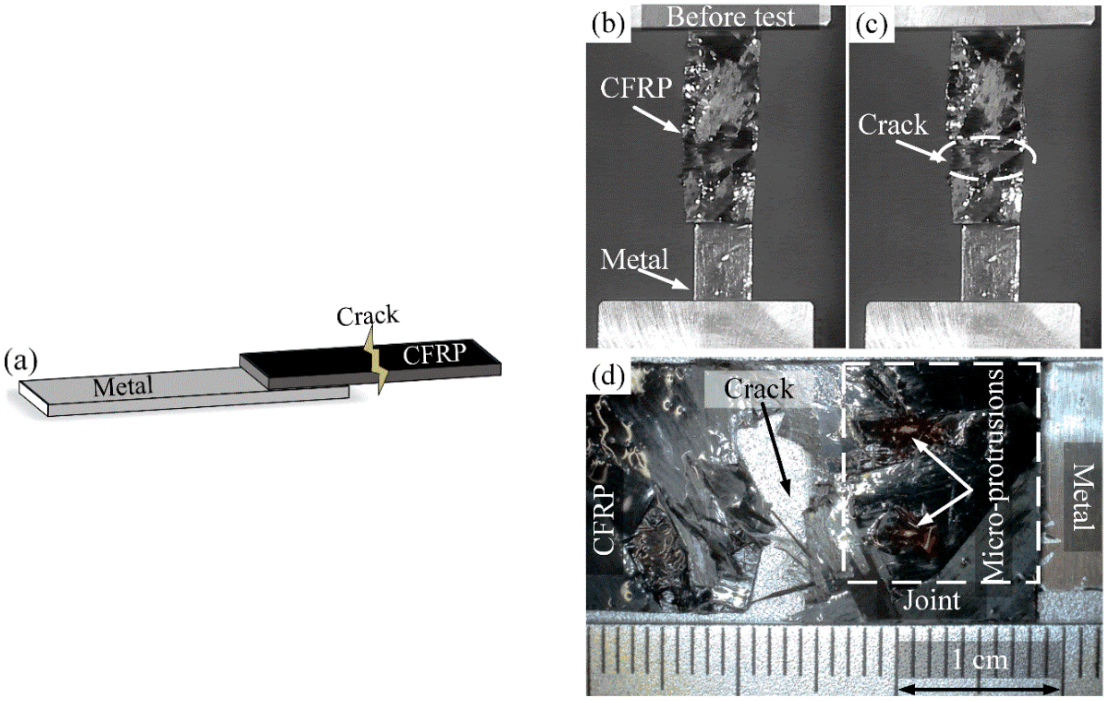

Fig. 7-6 Tensile test of the CFRP-SPCC joint based on SLM-manufactured micro-protrusions: (a) diagram of the break position; (b) sample before test; (c) sample after test; (d) fracture joint morphology of the metal side.

7.5 Disassembly Process Evaluation

In Chapter 5, the disassembly process of the joint based on FDM-manufactured micro-protrusions has been assessed. In this section, the disassembly process of the joint based on SLM-manufactured micro-protrusions will be evaluated. Through the analysis of the disassembly performance of joints based on FDM and SLM-manufactured micro-protrusions, the impact of these two manufacturing methods on the disassembly performance of joints can be evaluated, providing reference and guidance for the design and manufacture of joints that are easier to disassemble**.**

The disassembly process of the CFRP-metal joint based on SLM is illustrated in Fig. 7-7. Employing the same disassembly method, the metal plate side was first fixed, followed by the separation of the CFRP sheet from the left side of the joint in a tearing manner. In the initial stage, the separation occurred at the edge of the metal plate and the CFRP sheet, which was attributed to the failure of the cured resin, namely the failure of hydrogen bonding. With the increase in applied force, this crack would further propagate inward along the SPCC surface. Until Step 3, as shown in Fig. 7-7, the root of the micro-protrusions could gradually be observed, and with the force applied, the complete separation of the SPCC and CFRP sheet was achieved following the contour of the outer profile. Unlike the results in Section 5.5, this method completely separated the metal

and CFRP sheet.

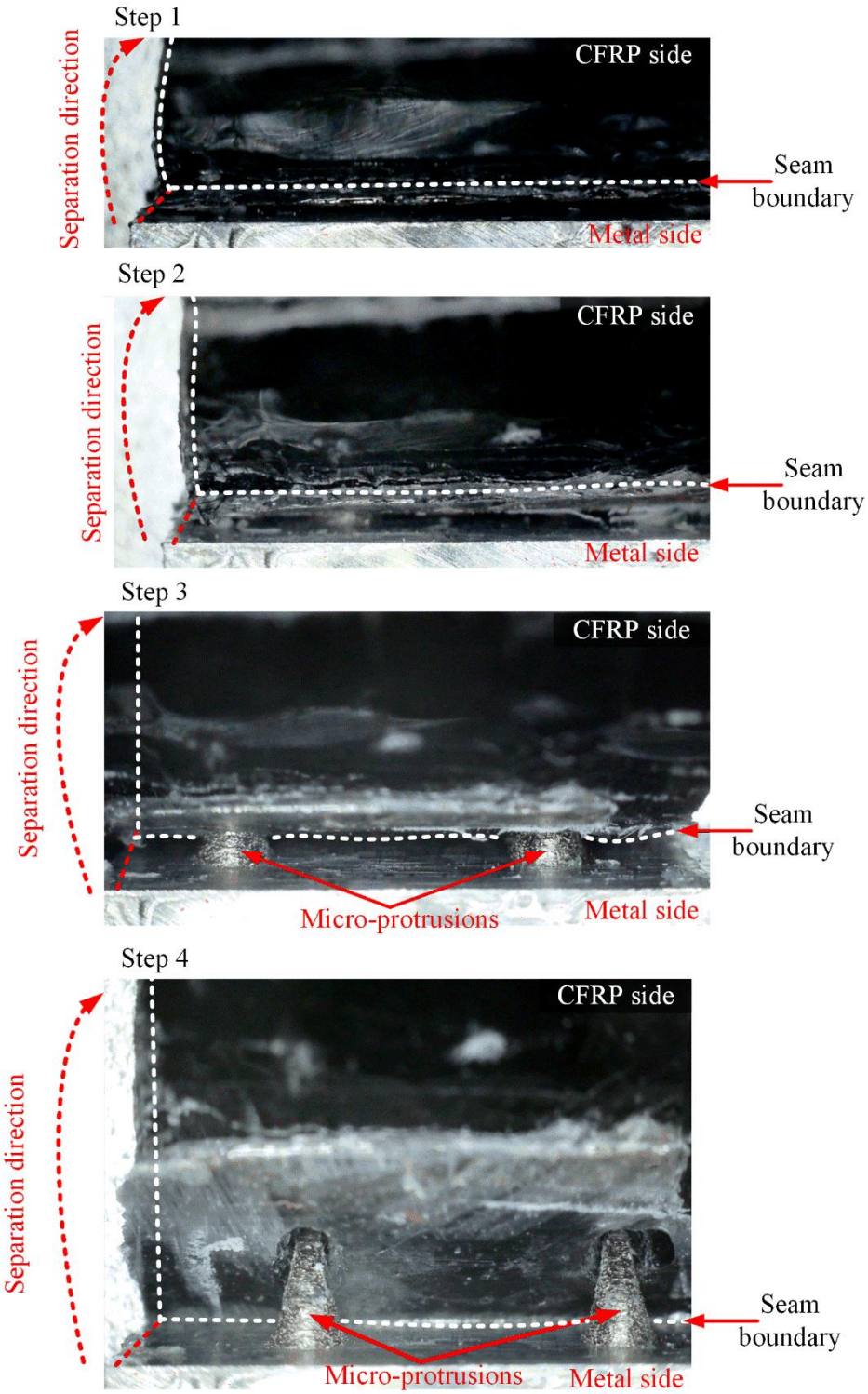

Fig. 7-7 Disassembly steps of the CFRP-SPCC joint based on SLM-manufactured micro-protrusions.

After the disassembly process finished, the disassembled components were been observed. Firstly, the CFRP sheet side and no macroscopic damage was found. Subsequently, the focus was on the areas where the micro-protrusions were embedded, and observations were conducted using SEM. The observation results are shown in Fig. 7-8. Fig. 7-8(a) displays the surface morphology of the CFRP sheet after disassembly. Due to the complete penetration of the CFRP plate by the micro-protrusions during the joining process, small holes were left on the CFRP sheet surface. These holes have irregular shapes but exhibit different sizes in the length and width directions, with a length of approximately 1.4 mm and a width of approximately 0.4 mm. These regular features are consistent with the elliptical cross-section of the micro-protrusions.

Fig. 7-8(b) shows the morphology of the underside of the CFRP sheet in contact with the metal after disassembly. Due to the micro-protrusions' continuous expansion from the tip to the base, the holes beneath the CFRP sheet also expand accordingly. However, the shape is uniform at this point, appearing elliptical, with a major axis of approximately 2.7 mm and a minor axis of approximately 1.4 mm. This design maintains nearly consistent dimensions at the micro-protrusions' base, and no carbon fiber damage was observed around the holes. Since the CFRP sheet surface has solidified, it presents a smooth surface under SEM.

Fig. 7-8(c) presents an enlarged view of the interior of the cavity beneath the CFRP sheet. The small holes left by the disassembled micro-protrusions on the CFRP sheet did not cause any damage. Although the hole walls are not entirely smooth, no significant defects were observed. This lack of smoothness may be related to the surface rough of the micro-protrusions manufactured by the SLM method.

On the macro scale, no damage was observed on the metal side after disassembly, including the SPCC matrix and the micro-protrusions. However, SEM observations were still conducted on the surface of the disassembled micro-protrusions. The results are shown in Fig. 7-9. The presence of carbon fibers can be observed in regions b, c, and d of Fig. 7-9(a). This indicates that a small amount of carbon fiber filaments remained on the micro-protrusion’s surface during disassembly. This phenomenon depends on two factors. First, we used chopped CFRP, characterized by carbon fiber filaments being exposed on the outermost surface. Therefore, during the joining process, carbon fiber filaments inevitably come into contact with the surface of the micro-protrusions. Secondly, the surface of the micro-protrusions may not be entirely smooth, which may lead to a small amount of carbon fiber filaments remaining on the surface of the micro-protrusions during

disassembly. However, this situation will not cause any damage to the performance of the carbon fiber plate.

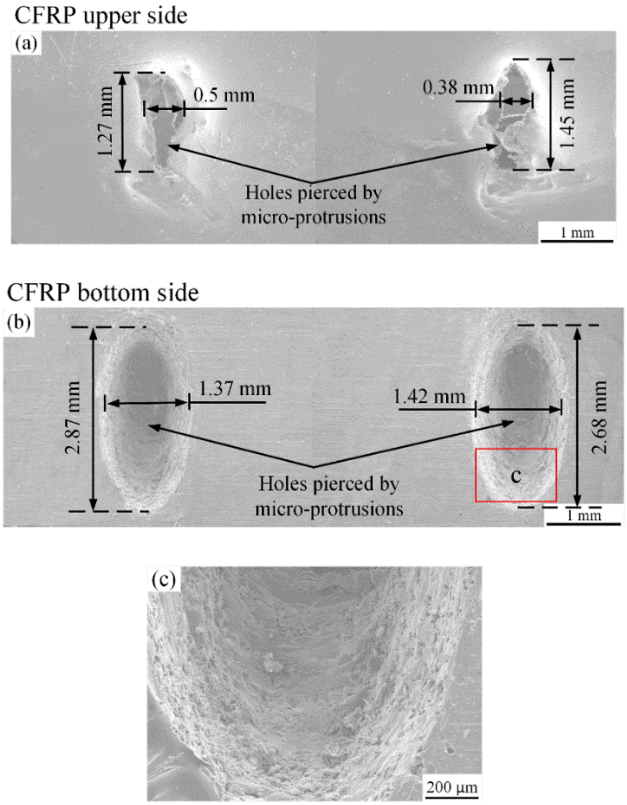

Fig. 7-8 The disassembled CFRP morphology under SEM: (a) CFRP top side; (b) CFRP bottom side; (c) fractural morphology of the c zone in Fig. 7-8(b).

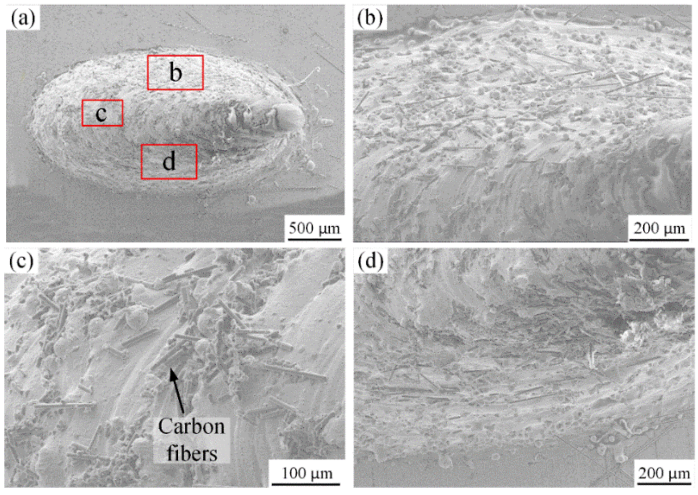

Fig. 7-9 The disassembled micro-protrusion morphology under SEM: (a) from top view; (b) magnification of the zone b in Fig. 7-9(a); (c) magnification of the zone c in Fig. 7-9(a); (d) magnification of the zone d in Fig. 7-9(a).

7.6 Conclusions

This chapter focuses on the fabricated micro-protrusions on the SPCC surfaces through the SLM technique and joining them with the epoxy resin-fused chopped CFRP sheet. A comprehensive analysis and characterization of the joint performance and disassembly process were conducted. Based on the research findings, the following key conclusions were drawn:

1、The rose thorn biomimetic micro-protrusion manufactured using the SLM method does not cause any damage to the carbon fibers when joining with the CFRP sheet. Its fine tip can first penetrate the gaps between carbon fibers and then gradually expand to achieve full adhesion of the metal surface with the CFRP sheet. The entire process does not cause any damage to the carbon fibers.

2、Tensile test results show that the fracture occurs in the epoxy resin fused chopped CFRP substrate area, indicating that the rose thorn structure made using the SLM technique can effectively enhance the joint's tensile strength.

3、The disassembly test demonstrates that the rose thorn biomimetic structure manufactured by the SLM method can achieve complete separation between metal and CFRP sheets. No apparent defects were found on the disassembled CFRP sheet.

4、The rose thorn biomimetic micro-protrusion created on metal surfaces using the SLM technique facilitates easy disassembly joining between metal and CFRP.

Chapter 8: Conclusions and Future Work

8.1 Summary

This study delved into the new concept of "easily disassemblable joining" between SPCC and CFRP, focusing on creating high-strength joints and facilitating the disassembly and recycling of end-of-life vehicles. Inspired by the structure and performances of rose thorns in nature, I developed a biomimetic design. I utilized cutting-edge manufacturing techniques such as fused deposition modeling (FDM) and selective laser melting (SLM) to investigate the joining and disassembly performance of CFRP and metal interfaces. The key conclusions drawn from this pioneering study are as follows:

1、Rose Thorn Biomimetic Structures Design

A geometrical model inspired by rose thorns was successfully established for the metal surface structuring, leading to a novel design approach for joining metals with CFRP. The shape and design of the biomimetic micro-protrusions, a key element in this study, played a critical role in stress distribution and joint strength. Properly optimized shapes can reduce stress concentration and enhance joint reliability.

2、Manufacturing Techniques: FDM and SLM

This study employed two manufacturing techniques, Fused Deposition Modeling (FDM) and Selective Laser Melting (SLM), to fabricate the rose thorn biomimetic micro-protrusions on metal surfaces for joining with CFRP. Both techniques, crucial in this research, were evaluated for their effectiveness in creating robust and precise joining structures, leading to different insights.

3、Fused Deposition Modeling (FDM)

FDM is a widely used additive manufacturing method known for its flexibility and accessibility. However, in this study, FDM exhibited limitations in manufacturing millimeter-scale biomimetic micro-protrusions. The primary issues observed included lower accuracy at the tips of the micro-protrusions, resulting in damage to CFRP during penetration. The layered "staircase" effect caused significant resistance during joining, leading to incomplete adhesion with the SPCC substrate. Additionally, tensile tests revealed fractures at the micro-protrusions, indicating that the mechanical performance deficiencies associated with FDM manufacturing may negatively affect joint strength. These findings highlight the necessity for more precise manufacturing techniques to ensure high-quality joining when utilizing rose thorn biomimetic structures in SPCC-CFRP joining processes.

4、Selective Laser Melting (SLM)

SLM, a more advanced additive manufacturing technique, uses a laser to melt metal powder to create precise and detailed structures. In this study, SLM demonstrated more significant success in fabricating biomimetic micro-protrusions on metal surfaces. The SLM-manufactured micro-protrusions exhibited lower surface roughness, reducing the risk of carbon fiber damage when joining with CFRP. The enhanced precision and reduced surface defects resulted in stronger joints, as confirmed by tensile tests showing fractures occurring within the CFRP substrate rather than the joint interface. Additionally, the SLM process allowed for easier disassembly, demonstrating the potential for achieving high-strength joints while facilitating end-of-life recycling and reusability. These results suggest that SLM is a more suitable manufacturing technique for producing biomimetic micro-protrusions, contributing to improved joint strength and disassembly efficiency.

This research establishes a robust framework for achieving high-strength joints while enabling easy disassembly between metal and CFRP. It presents opportunities for broader applications in lightweight and environmentally conscious manufacturing. The implications for future studies are significant, opening new pathways to sustainable design, improved recycling, and efficient resource utilization.

8.2 Future Work

8.2.1 Optimize the Design Process of the Biomimetic Structure Shape

The current study primarily focused on the structural design of the rose thorn biomimetic patterns without extensive consideration of the various environmental conditions in which the joints might operate. Future work should include detailed studies on how different environmental factors, such as temperature fluctuations, humidity, corrosive environments, and long-term mechanical exposure, affect the performance and durability of the joints. This will provide a better understanding of the practical applicability of biomimetic structures in real-world scenarios. Additionally, future research should explore advanced computational techniques, such as finite element analysis and machine learning algorithms, to optimize the shape and distribution of micro-protrusions. This will ensure that stress concentrations are minimized and joint reliability is maximized under various loading conditions.

8.2.2 Improve the FDM Manufacturing Process

The parameters related to debinding and sintering during the FDM process significantly impact the final product performance, affecting the joints' performance. Due to time constraints and limitations in experimental equipment, this study did not systematically investigate these factors. Therefore, further research on the debinding and sintering processes in FDM is necessary to optimize manufacturing parameters and improve joint quality. Future studies should focus on a detailed analysis of these parameters, including the effects of varying debinding and sintering conditions on the mechanical properties of the printed parts. By systematically exploring these aspects, enhancing the overall performance and reliability of joints formed using FDM-manufactured components will be possible.

8.2.3 Broden the Appliable Materiales Range and Application Scenarios

The primary objective of this research has been to establish the concept of “easily disassemblable joining” between metal and polymer materials. The current study focused on SPCC as the metal and self-processed CFRP as the polymer to demonstrate this concept. Moving forward, it should extend this easily disassemblable joining concept to a broader range of materials. Future work needs to explore various metal substrates and commercially available CFRP materials to validate and enhance the applicability of the disassembly joining technique. This will broaden the scope of materials that can benefit from this joining method and provide valuable insights into optimizing the process for different material combinations, ensuring its effectiveness and versatility in diverse industrial applications.

Publications and Conferences

Publications

[1] **Wang T,** Yasuda K, Nishikawa H. Design of rose thorn biomimetic micro-protrusion for metals and CFRTP easily disassembled joining [J]. Engineering Research Express, 2024, 6(2):025512. doi.10.1088/2631-8695/ad3c10

[2] **Wang T,** Yasuda K, Nishikawa H. Study on the SPCC and CFRTP hybrid joint performance produced with additional Nylon-6 interlayer by ultrasonic plastic welding [J]. *Polymers.* 2022, 14(23):5235. doi.org/10.3390/polym14235235

[3] **Tai Wang,** Kiyokazu Yasuda, Hiroshi Nishikawa. Fabrication of micron-sized protrusions on metal surface for metal/polymer easy-disassembly joining by selective laser melting technology [J]. Materials & Design. 2022, 220:110873. doi.org/10.1016/j.matdes.2022.110873

Conferences

[1] **Tai WANG**, Fabrication of micro-sized protrusions on metal surface for metal/polymer easy disassembly joining by selective laser melting technology. International Institute of Welding (IIW), 2022.07, Conference. (Oral)

[2] **Tai WANG**, Dissimilar materials joining of SPCC and CFRTP based on surface structuring. Japan Welding Society (JWS), 2021.09, Conference. (Oral)

[3] **Tai WANG**, International Institute of Welding (IIW), 2021.07, Conference.

Acknowledgments

First and foremost, I would like to extend my most sincere gratitude to my advisors, Professor Yasuda and Professor Nishikawa. Throughout this academic journey, they have provided immense support not only in the realm of scientific research but also in imparting the right attitude and ways of thinking essential for conducting research. Professor Yasuda's meticulous and rigorous research methods and Professor Nishikawa's profound academic insights have continually inspired me to strive for excellence. Whether it was in experimental design, data analysis, or thesis writing, they have offered me selfless guidance and support. Additionally, they provided me with valuable opportunities and advice during various academic exchange activities, helping me broaden my academic horizons and enhance my scholarly abilities.I would also like to thank my family. Their selfless help and support have been a crucial driving force in my perseverance. Whether it was moral encouragement or support in daily life, they have always been my steadfast support. Without their understanding and companionship, I would not have been able to successfully complete this doctoral dissertation.

The completion of this doctoral dissertation does not signify the end of my research and learning journey. On the contrary, it marks a new beginning. In the days to come, I will continue to maintain a dedicated attitude, working tirelessly in my future positions, striving to shine in both my academic and professional career. I believe that with the knowledge and experience gained during my doctoral studies, I will be able to overcome various challenges and achieve greater accomplishments in the future.

Lastly, I would like to thank everyone who has provided help and support during this journey once again. Your care and support have given me the courage and strength to complete this challenging task. I will cherish this experience and use it as motivation to keep moving forward.

In addition, I acknowledge that this research is supported by JST SPRING [Grant Number JPMJSP2138], and The Amada Foundation [AF-2019227-B3]. I appreciate the funding.

July 2024

Tai WANG

Departure of Materials and Manufacturing Science

Osaka University

References

[1] S. Niu, Y. Ding, Y. Niu, Y. Li, and G. Luo, "Economic growth, energy conservation and emissions reduction: A comparative analysis based on panel data for 8 Asian-Pacific countries," *Energy Policy,* vol. 39, no. 4, pp. 2121-2131, 2011, doi: 10.1016/j.enpol.2011.02.003.

[2] H. Huang, H. Wang, Y.-J. Hu, C. Li, and X. Wang, "The development trends of existing building energy conservation and emission reduction—A comprehensive review," *Energy Reports,* vol. 8, pp. 13170-13188, 2022, doi: 10.1016/j.egyr.2022.10.023.

[3] Y. Zhou, "Worldwide carbon neutrality transition? Energy efficiency, renewable, carbon trading and advanced energy policies," *Energy Reviews,* vol. 2, no. 2, 2023, doi: 10.1016/j.enrev.2023.100026.

[4] N. Kleanthis *et al.*, "Eliciting knowledge from stakeholders to identify critical issues of the transition to climate neutrality in Greece, the Nordic Region, and the European Union," *Energy Research & Social Science,* vol. 93, 2022, doi: 10.1016/j.erss.2022.102836.

[5] A. Ozawa, T. Tsani, and Y. Kudoh, "Japan's pathways to achieve carbon neutrality by 2050 – Scenario analysis using an energy modeling methodology," *Renewable and Sustainable Energy Reviews,* vol. 169, 2022, doi: 10.1016/j.rser.2022.112943.

[6] Z. Wu, X. Huang, R. Chen, X. Mao, and X. Qi, "The United States and China on the paths and policies to carbon neutrality," *J Environ Manage,* vol. 320, p. 115785, Oct 15 2022, doi: 10.1016/j.jenvman.2022.115785.

[7] J. Fan, J. Wang, M. Liu, W. Sun, and Z. Lan, "Scenario simulations of China's natural gas consumption under the dual-carbon target," *Energy,* vol. 252, 2022, doi: 10.1016/j.energy.2022.124106.

[8] J. Fu *et al.*, "Fight for carbon neutrality with state-of-the-art negative carbon emission technologies," *Eco Environ Health,* vol. 1, no. 4, pp. 259-279, Dec 2022, doi: 10.1016/j.eehl.2022.11.005.

[9] Y.-M. Wei, K. Chen, J.-N. Kang, W. Chen, X.-Y. Wang, and X. Zhang, "Policy and Management of Carbon Peaking and Carbon Neutrality: A Literature Review," *Engineering,* vol. 14, pp. 52-63, 2022, doi: 10.1016/j.eng.2021.12.018.

[10] M. A. Muflikhun, T. Yokozeki, and T. Aoki, "The strain performance of thin CFRP-SPCC hybrid laminates for automobile structures," *Composite Structures,* vol. 220, pp. 11-18,

2019, doi: 10.1016/j.compstruct.2019.03.094.

[11] P. Galvez, A. Quesada, M. A. Martinez, J. Abenojar, M. J. L. Boada, and V. Diaz, "Study of the behaviour of adhesive joints of steel with CFRP for its application in bus structures," *Composites Part B: Engineering,* vol. 129, pp. 41-46, 2017, doi: 10.1016/j.compositesb.2017.07.018.

[12] K. Martinsen, S. J. Hu, and B. E. Carlson, "Joining of dissimilar materials," *CIRP Annals,* vol. 64, no. 2, pp. 679-699, 2015, doi: 10.1016/j.cirp.2015.05.006.

[13] B. Watson, Y. Nandwani, M. J. Worswick, and D. S. Cronin, "Metallic multi-material adhesive joint testing and modeling for vehicle lightweighting," *International Journal of Adhesion and Adhesives,* vol. 95, 2019, doi: 10.1016/j.ijadhadh.2019.102421.

[14] A. Peppas, K. Kollias, D. A. Dragatogiannis, and C. A. Charitidis, "Sustainability analysis of aluminium hot forming and quenching technology for lightweight vehicles manufacturing," *International Journal of Thermofluids,* vol. 10, 2021, doi: 10.1016/j.ijft.2021.100082.

[15] F. E. K. Sato and T. Nakata, "Analysis of the impact of vehicle lightweighting on recycling benefits considering life cycle energy reductions," *Resources, Conservation and Recycling,* vol. 164, 2021, doi: 10.1016/j.resconrec.2020.105118.

[16] B. M. Al-Alawi and T. H. Bradley, "Analysis of corporate average fuel economy regulation compliance scenarios inclusive of plug in hybrid vehicles," *Applied Energy,* vol. 113, pp. 1323-1337, 2014, doi: 10.1016/j.apenergy.2013.08.081.

[17] H. Martins, C. O. Henriques, J. R. Figueira, C. S. Silva, and A. S. Costa, "Assessing policy interventions to stimulate the transition of electric vehicle technology in the European Union," *Socio-Economic Planning Sciences,* vol. 87, 2023, doi: 10.1016/j.seps.2022.101505.

[18] R. Peng, J. H. C. G. Tang, X. Yang, M. Meng, J. Zhang, and C. Zhuge, "Investigating the factors influencing the electric vehicle market share: A comparative study of the European Union and United States," *Applied Energy,* vol. 355, 2024, doi: 10.1016/j.apenergy.2023.122327.

[19] J. M. Luk, H. C. Kim, R. D. De Kleine, T. J. Wallington, and H. L. MacLean, "Greenhouse gas emission benefits of vehicle lightweighting: Monte Carlo probabalistic analysis of the multi material lightweight vehicle glider," *Transportation Research Part D: Transport and Environment,* vol. 62, pp. 1-10, 2018, doi: 10.1016/j.trd.2018.02.006.

[20] P. Di Trolio, P. Di Giorgio, M. Genovese, E. Frasci, and M. Minutillo, "A hybrid power-unit based on a passive fuel cell/battery system for lightweight vehicles," *Applied Energy,* vol. 279, 2020, doi: 10.1016/j.apenergy.2020.115734.

[21] W. Zhang and J. Xu, "Advanced lightweight materials for Automobiles: A review," *Mater Design,* vol. 221, 2022, doi: 10.1016/j.matdes.2022.110994.

[22] N. Shanmugavel, R. Rajendran, and M. Micheal, "An exploration on the influence of altruistic factors on voluntary vehicle scrapping to promote sustainable environment," *Cleaner Materials,* vol. 4, 2022, doi: 10.1016/j.clema.2022.100081.

[23] J. Balaguer, J. C. Pernías, and J. Ripollés, "Is vehicle scrapping affected by low-emission zones? The case of Madrid," *Transportation Research Part A: Policy and Practice,* vol. 172, 2023, doi: 10.1016/j.tra.2023.103668.

[24] S. Siengchin, "A review on lightweight materials for defence applications: Present and future developments," *Defence Technology,* vol. 24, pp. 1-17, 2023, doi: 10.1016/j.dt.2023.02.025.

[25] H. Hatayama, I. Daigo, Y. Matsuno, and Y. Adachi, "Evolution of aluminum recycling initiated by the introduction of next-generation vehicles and scrap sorting technology," *Resources, Conservation and Recycling,* vol. 66, pp. 8-14, 2012, doi: 10.1016/j.resconrec.2012.06.006.

[26] H. Ohno, K. Matsubae, K. Nakajima, Y. Kondo, S. Nakamura, and T. Nagasaka, "Toward the efficient recycling of alloying elements from end of life vehicle steel scrap," *Resources, Conservation and Recycling,* vol. 100, pp. 11-20, 2015, doi: 10.1016/j.resconrec.2015.04.001.

[27] Y. Zhu *et al.*, "The coming wave of aluminum sheet scrap from vehicle recycling in the United States," *Resources, Conservation and Recycling,* vol. 164, 2021, doi: 10.1016/j.resconrec.2020.105208.

[28] Z. Li *et al.*, "A circular economy approach for recycling Electric Motors in the end-of-life Vehicles: A literature review," *Resources, Conservation and Recycling,* vol. 205, 2024, doi: 10.1016/j.resconrec.2024.107582.

[29] Q. Hoarau and E. Lorang, "An assessment of the European regulation on battery recycling for electric vehicles," *Energy Policy,* vol. 162, 2022, doi: 10.1016/j.enpol.2021.112770.

[30] H. Buchner, D. Laner, H. Rechberger, and J. Fellner, "Potential recycling constraints due to future supply and demand of wrought and cast Al scrap—A closed system perspective

on Austria," *Resources, Conservation and Recycling,* vol. 122, pp. 135-142, 2017, doi: 10.1016/j.resconrec.2017.01.014.

[31] V. K. Soo, M. Doolan, P. Compston, J. R. Duflou, J. Peeters, and Y. Umeda, "The influence of end-of-life regulation on vehicle material circularity: A comparison of Europe, Japan, Australia and the US," *Resources, Conservation and Recycling,* vol. 168, 2021, doi: 10.1016/j.resconrec.2020.105294.

[32] "Life Cycle Primary Energy Demand and Greenhouse Gas Emission benefits of vehicle lightweighting with recycled carbon fibre."

[33] M. K. Gupta and V. Singhal, "Review on materials for making lightweight vehicles," *Materials Today: Proceedings,* vol. 56, pp. 868-872, 2022, doi: 10.1016/j.matpr.2022.02.517.

[34] K. Kawajiri, M. Kobayashi, and K. Sakamoto, "Lightweight materials equal lightweight greenhouse gas emissions?: A historical analysis of greenhouse gases of vehicle material substitution," *J Clean Prod,* vol. 253, 2020, doi: 10.1016/j.jclepro.2019.119805.

[35] M. Raugei, D. Morrey, A. Hutchinson, and P. Winfield, "A coherent life cycle assessment of a range of lightweighting strategies for compact vehicles," *J Clean Prod,* vol. 108, pp. 1168-1176, 2015, doi: 10.1016/j.jclepro.2015.05.100.

[36] H. Monteiro, R. Alonso, M. Gonçalves, M. Iten, and N. S. Caetano, "Life cycle energy of vehicles on lightweighting and alternative powertrain strategies—A review," *Energy Reports,* vol. 8, pp. 241-247, 2022, doi: 10.1016/j.egyr.2022.01.037.

[37] K. Iwata, A. Suzuki, S.-G. Kim, N. Takata, and M. Kobashi, "Enhancing the solid-state joinability of A5052 and CFRTP via an additively manufactured micro-structure," *J Mater Process Tech,* vol. 306, 2022, doi: 10.1016/j.jmatprotec.2022.117629.

[38] D. W. Zhang, Q. Zhang, X. G. Fan, and S. D. Zhao, "Review on Joining Process of Carbon Fiber-reinforced Polymer and Metal: Applications and Outlook," (in English), *Rare Metal Mat Eng,* vol. 48, no. 1, pp. 44-54, Jan 2019. [Online]. Available: <Go to ISI>://WOS:000457815200007.

[39] A. A. Abdulrazaq, S. R. Ahmed, and F. M. Mahdi, "Agricultural waste and natural dolomite for green production of aluminum composites," *Cleaner Engineering and Technology,* vol. 11, 2022, doi: 10.1016/j.clet.2022.100565.

[40] F. Xiao, J. Hu, Z. Lin, and R. Luo, "Optimization of vehicle structural parameters considering stability improvement," *Applied Mathematical Modelling,* vol. 117, pp. 42-62,

2023, doi: 10.1016/j.apm.2022.12.019.

[41] G. Corrado *et al.*, "Recent progress, challenges and outlook for multidisciplinary structural optimization of aircraft and aerial vehicles," *Progress in Aerospace Sciences,* vol. 135, 2022, doi: 10.1016/j.paerosci.2022.100861.

[42] S. Li and X. Feng, "Study of structural optimization design on a certain vehicle body-in-white based on static performance and modal analysis," *Mechanical Systems and Signal Processing,* vol. 135, 2020, doi: 10.1016/j.ymssp.2019.106405.

[43] A. N. Pratomo, S. P. Santosa, L. Gunawan, D. Widagdo, and I. S. Putra, "Design optimization and structural integrity simulation of aluminum foam sandwich construction for armored vehicle protection," *Composite Structures,* vol. 276, 2021, doi: 10.1016/j.compstruct.2021.114461.

[44] W. Cui, Y. Yang, and L. Di, "Modeling and optimization for static-dynamic routing of a vehicle with additive manufacturing equipment," *International Journal of Production Economics,* vol. 257, 2023, doi: 10.1016/j.ijpe.2022.108756.

[45] E. Duriez, C. Azzaro-Pantel, J. Morlier, and M. Charlotte, "A fast method of material, design and process eco-selection via topology optimization, for additive manufactured structures," *Cleaner Environmental Systems,* vol. 9, 2023, doi: 10.1016/j.cesys.2023.100114.

[46] "A study on the process design of prepreg compression forming using rapid heating and cooling system," 2017.

[47] F. Lambiase, S. I. Scipioni, C. J. Lee, D. C. Ko, and F. Liu, "A State-of-the-Art Review on Advanced Joining Processes for Metal-Composite and Metal-Polymer Hybrid Structures," *Materials (Basel),* vol. 14, no. 8, Apr 10 2021, doi: 10.3390/ma14081890.

[48] F. Bañon, A. Sambruno, M. Batista, B. Simonet, and J. Salguero, "Evaluation of geometrical defects in AWJM process of a hybrid CFRTP/Steel structure," *International Journal of Mechanical Sciences,* vol. 210, 2021, doi: 10.1016/j.ijmecsci.2021.106748.

[49] J. Zhang and J. Yanagimoto, "Design and fabrication of formable CFRTP core sandwich sheets," *CIRP Annals,* vol. 68, no. 1, pp. 281-284, 2019, doi: 10.1016/j.cirp.2019.04.060.

[50] H. Ota *et al.*, "Effect of the interfacial nanostructure on the interlaminar fracture toughness and damage mechanisms of directly bonded carbon fiber reinforced thermoplastics and aluminum," *Composites Part A: Applied Science and Manufacturing,* vol. 139, 2020, doi: 10.1016/j.compositesa.2020.106101.

[51] E. Ota *et al.*, "Friction stir spot welding of aluminum and carbon fiber reinforced thermoplastic using hybrid surface treatment improving interfacial properties," *Mater Design,* vol. 212, 2021, doi: 10.1016/j.matdes.2021.110221.

[52] G. D. Goh, W. Toh, Y. L. Yap, T. Y. Ng, and W. Y. Yeong, "Additively manufactured continuous carbon fiber-reinforced thermoplastic for topology optimized unmanned aerial vehicle structures," *Composites Part B: Engineering,* vol. 216, 2021, doi: 10.1016/j.compositesb.2021.108840.

[53] K. Kira, S. Kim, T. Yamamoto, K. Kato, and M. Nomura, "Structural design to enhance mechanical properties of carbon-fiber-reinforced thermoplastics using colloidal particles and soft and hard resins," *Composites Part C: Open Access,* vol. 6, 2021, doi: 10.1016/j.jcomc.2021.100211.

[54] A. Wazeer, A. Das, C. Abeykoon, A. Sinha, and A. Karmakar, "Composites for electric vehicles and automotive sector: A review," *Green Energy and Intelligent Transportation,* vol. 2, no. 1, 2023, doi: 10.1016/j.geits.2022.100043.

[55] "Evaluation of a concept out-of-autoclave process for manufacturing carbon fibre reinforced polymer automotive parts."

[56] T. Yamamoto and Y. Ota, "Creating a laminated carbon fiber-reinforced thermoplastic using polypropylene and nylon with a polypropylene colloid," *Composite Structures,* vol. 255, 2021, doi: 10.1016/j.compstruct.2020.113038.

[57] C. Gómez, D. Tobalina-Baldeon, F. Cavas, and F. Sanz-Adan, "Geometrical optimization of thermoforming continuous fibers reinforced thermoplastics with Finite Element Models: A case study," *Composites Part B: Engineering,* vol. 239, 2022, doi: 10.1016/j.compositesb.2022.109950.

[58] Z. Liu, Y. Li, Y. Wang, B. I. Epureanu, and M. Banu, "Nonlinear friction behavior in ultrasonic welding of aluminum alloy to carbon fiber reinforced PA6 composite," *J Mater Process Tech,* vol. 296, 2021, doi: 10.1016/j.jmatprotec.2021.117230.

[59] F. Staab and F. Balle, "Ultrasonic torsion welding of ageing-resistant Al/CFRP joints: Properties, microstructure and joint formation," *Ultrasonics,* vol. 93, pp. 139-144, Mar 2019, doi: 10.1016/j.ultras.2018.11.006.

[60] "New metals remanufacturing business models in automotive industry," 2022.

[61] E. Suzanne, N. Absi, and V. Borodin, "Towards circular economy in production planning: Challenges and opportunities," *European Journal of Operational Research,* vol. 287, no.

1, pp. 168-190, 2020, doi: 10.1016/j.ejor.2020.04.043.

[62] T. Irisawa, "The development toward the realization of sustainable carbon fiber-reinforced thermoplastics," *Carbon,* vol. 175, pp. 612-613, 2021, doi: 10.1016/j.carbon.2021.01.080.

[63] T. Irisawa, R. Iwamura, Y. Kozawa, S. Kobayashi, and Y. Tanabe, "Recycling methods for thermoplastic-matrix composites having high thermal stability in focusing on reuse of the carbon fibers," *Carbon,* vol. 175, 2021, doi: 10.1016/j.carbon.2021.01.042.

[64] E. Asmatulu, J. Twomey, and M. Overcash, "Evaluation of recycling efforts of aircraft companies in Wichita," *Resources, Conservation and Recycling,* vol. 80, pp. 36-45, 2013, doi: 10.1016/j.resconrec.2013.08.002.

[65] C. Favi, M. Marconi, M. Germani, and M. Mandolini, "A design for disassembly tool oriented to mechatronic product de-manufacturing and recycling," *Advanced Engineering Informatics,* vol. 39, pp. 62-79, 2019, doi: 10.1016/j.aei.2018.11.008.

[66] "Review on Joining Process of Carbon Fiber-reinforced Polymer and Metal Applications and Outlook," 2019.

[67] "Overview of joining dissimilar materials metals and polymers " 2017.

[68] Y.-G. Lee and D.-O. Lee, "Manufacturing technique and verification for the mechanical fastening section of carbon fiber reinforced anisogrid composite structures," *Composite Structures,* vol. 268, 2021, doi: 10.1016/j.compstruct.2021.113895.

[69] Y. Bai, Z. He, N. Bao, H. Wang, and P. Zhang, "Research on the influence of loading frequency, material elasticity, and geometric parameters on mechanical characteristics of the new mesh-type high damping rail pad for fastening system," *Structures,* vol. 53, pp. 421-431, 2023, doi: 10.1016/j.istruc.2023.04.089.

[70] T. Gerhard and C. Friedrich, "Mechanical fastening of carbon composite tubes, numerical calculation of axial loading capacity and experimental verification," *Composites Part B: Engineering,* vol. 67, pp. 391-399, 2014, doi: 10.1016/j.compositesb.2014.07.024.

[71] M. Ueda, S. Miyake, H. Hasegawa, and Y. Hirano, "Instantaneous mechanical fastening of quasi-isotropic CFRP laminates by a self-piercing rivet," *Composite Structures,* vol. 94, no. 11, pp. 3388-3393, 2012, doi: 10.1016/j.compstruct.2012.04.027.

[72] J.-H. Kweon, J.-W. Jung, T.-H. Kim, J.-H. Choi, and D.-H. Kim, "Failure of carbon composite-to-aluminum joints with combined mechanical fastening and adhesive bonding," *Composite Structures,* vol. 75, no. 1-4, pp. 192-198, 2006, doi: 10.1016/j.compstruct.2006.04.013.

[73] C. Absi, N. Alsinani, and L. Laberge Lebel, "Carbon fiber reinforced poly(ether ether ketone) rivets for fastening composite structures," *Composite Structures,* vol. 280, 2022, doi: 10.1016/j.compstruct.2021.114877.

[74] F. Karaboğa, F. Göleç, D. E. Yunus, S. Toros, and Y. Öz, "Mechanical response of carbon fiber reinforced epoxy composite parts joined with varying bonding techniques for aerospace applications," *Composite Structures,* vol. 331, 2024, doi: 10.1016/j.compstruct.2024.117920.

[75] H. Gotoh, K. Kanno, T. Tani, Y. Akematsu, and N. Mohri, "Rivet Fastening Process for Carbon Fiber Reinforced Thermoplastics (CFRTP) under Ultrasonic Vibration. Micro Hole Machining of CFRTP with a Vibrated Needle Tool," *Procedia CIRP,* vol. 68, pp. 456-459, 2018, doi: 10.1016/j.procir.2017.12.078.

[76] L. Meng, Y. Wan, I. Ohsawa, and J. Takahashi, "Effects of geometric parameters on the failure behavior of mechanically fastened chopped carbon fiber tape reinforced thermoplastics," *Composite Structures,* vol. 229, 2019, doi: 10.1016/j.compstruct.2019.111475.

[77] Z. Feng, H. Zhao, C. Tan, X. Zhang, B. Chen, and X. Song, "Nanosecond laser ablation for improving the strength of CFRTP and aluminum alloy adhesively bonded joints," *Composite Structures,* vol. 274, 2021, doi: 10.1016/j.compstruct.2021.114369.

[78] J. Liu, Y. Li, M. Huang, Y. Lu, and Y. Yang, "The effect of transverse low-velocity pre-impact on the residual strength of Al/PEEK/CFRTP adhesive joints," *International Journal of Impact Engineering,* vol. 168, 2022, doi: 10.1016/j.ijimpeng.2022.104295.

[79] S. J. Lim, J. Cheon, and M. Kim, "Effect of laser surface treatments on a thermoplastic PA 6/carbon composite to enhance the bonding strength," *Composites Part A: Applied Science and Manufacturing,* vol. 137, 2020, doi: 10.1016/j.compositesa.2020.105989.

[80] Y. Qiao *et al.*, "Plasma treatment on both adhesive tape and adherends for significantly enhanced CFRTP-related adhesive joints," *Appl Surf Sci,* vol. 649, 2024, doi: 10.1016/j.apsusc.2023.159092.

[81] J. Zhao, H. Zhao, Y. Guo, Q. Li, and X. Chen, "Enhanced interfacial bonding strength of hot-pressed titanium Alloy/CFRTP joint via laser ablation and interfacial adhesive," *Composites Communications,* vol. 48, 2024, doi: 10.1016/j.coco.2024.101901.

[82] G.-P. Zhang, J.-C. Li, Z.-X. Liu, and P.-C. Wang, "Application of ultrasonic welding to repair adhesively bonded short carbon fiber reinforced Nylon 6 composites," *International*

Journal of Adhesion and Adhesives, vol. 100, 2020, doi: 10.1016/j.ijadhadh.2020.102603.

[83] S. Simaafrookhteh, P. Tsokanas, T. Loutas, S. V. Lomov, and J. Ivens, "Measuring the interlaminar fracture toughness of thin carbon fiber/polyamide6 composites using adhesively bonded stiffeners," *Composites Part A: Applied Science and Manufacturing,* vol. 176, 2024, doi: 10.1016/j.compositesa.2023.107841.

[84] S.-F. Tseng and Y.-S. Chen, "Surface microtexturing of Ti-6Al-4V and SS316L alloys using high pulsed fiber lasers for improving the adhesive bonded performance," *Optics & Laser Technology,* vol. 143, 2021, doi: 10.1016/j.optlastec.2021.107349.

[85] H. D. Roh *et al.*, "Analysis of energy release rate of laser-induced cohesive bonding of carbon fiber-reinforced polyetherketoneketone thermoplastic composites," *Polymer Testing,* vol. 129, 2023, doi: 10.1016/j.polymertesting.2023.108271.

[86] T. Ishikawa *et al.*, "Overview of automotive structural composites technology developments in Japan," *Composites Science and Technology,* vol. 155, pp. 221-246, 2018, doi: 10.1016/j.compscitech.2017.09.015.

[87] Y. Guo, Y. Li, S. Wang, Z.-X. Liu, B. Cai, and P.-C. Wang, "Effect of silane treatment on adhesion of adhesive-bonded carbon fiber reinforced nylon 6 composite," *International Journal of Adhesion and Adhesives,* vol. 91, pp. 102-115, 2019, doi: 10.1016/j.ijadhadh.2019.03.008.

[88] C. Chen, C. Sun, X. Han, D. Hu, J. Zhou, and Z. Guan, "The structural response of the thermoplastic composite joint subjected to out-of-plane loading," *International Journal of Impact Engineering,* vol. 145, 2020, doi: 10.1016/j.ijimpeng.2020.103691.

[89] A. Suzuki, K. Noritake, N. Takata, and M. Kobashi, "Joint strength of Fe/epoxy resin hybrid structure via porous Fe/TiB2 composite layer synthesized by in-situ reaction process," *J Mater Process Tech,* vol. 288, 2021, doi: 10.1016/j.jmatprotec.2020.116843.

[90] Y. Ma, D. Bridges, Y. Yu, J. Han, H. Li, and A. Hu, "Joining of Carbon Fiber Reinforced Plastic to Aluminum Alloy by Reactive Multilayer Films and Low Power Semiconductor Laser Heating," *Applied Sciences,* vol. 9, no. 2, 2019, doi: 10.3390/app9020319.

[91] Q. Wang, Z.-y. Jia, B.-y. Zhang, D.-l. Gao, Y. Ma, and J.-y. Liu, "Influence of processing parameters on joint shear performance in laser direct joining of CFRTP and aluminum alloy," *Mater Design,* vol. 209, 2021, doi: 10.1016/j.matdes.2021.109996.

[92] Z. Zhang, J.-G. Shan, X.-H. Tan, and J. Zhang, "Effect of anodizing pretreatment on laser joining CFRP to aluminum alloy A6061," *International Journal of Adhesion and Adhesives,*

vol. 70, pp. 142-151, 2016, doi: 10.1016/j.ijadhadh.2016.06.007.

[93] C. Tan *et al.*, "Enhanced interfacial bonding strength of laser bonded titanium alloy/CFRTP joint via hydrogen bonds interaction," *Composites Part B: Engineering,* vol. 239, 2022, doi: 10.1016/j.compositesb.2022.109966.

[94] J. Jiao, Q. Wang, F. Wang, S. Zan, and W. Zhang, "Numerical and experimental investigation on joining CFRTP and stainless steel using fiber lasers," *J Mater Process Tech,* vol. 240, pp. 362-369, 2017, doi: 10.1016/j.jmatprotec.2016.10.013.

[95] Z. Feng *et al.*, "Influence of process parameters on the joint characteristics during laser joining of aluminium alloy and CFRTP," *J Manuf Process,* vol. 64, pp. 1493-1506, 2021, doi: 10.1016/j.jmapro.2021.03.006.

[96] Y. Zhang *et al.*, "Microstructure and joining mechanism of Al/CFRTP resistance element welded joints," *J Manuf Process,* vol. 84, pp. 251-259, 2022, doi: 10.1016/j.jmapro.2022.10.014.

[97] M. O. Voltz, O. Zöllner, and P. Mitschang, "Effects of thermoforming parameters and layup on unidirectional reinforced amorphous thermoplastic composite surfaces," *Composites Part A: Applied Science and Manufacturing,* vol. 180, 2024, doi: 10.1016/j.compositesa.2024.108063.

[98] J. Jiao, J. Xu, C. Jing, L. Sheng, H. Ru, and H. Xia, "Laser welding process and strength enhancement of carbon fiber reinforced thermoplastic composites and metals dissimilar joint: A review," *Chinese Journal of Aeronautics,* vol. 36, no. 12, pp. 13-31, 2023, doi: 10.1016/j.cja.2023.02.025.

[99] A. Pramanik *et al.*, "Joining of carbon fibre reinforced polymer (CFRP) composites and aluminium alloys - A review," (in English), *Compos Part a-Appl S,* vol. 101, pp. 1-29, Oct 2017, doi: 10.1016/j.compositesa.2017.06.007.

[100] P. K. Penumakala, J. Santo, and A. Thomas, "A critical review on the fused deposition modeling of thermoplastic polymer composites," *Composites Part B: Engineering,* vol. 201, 2020, doi: 10.1016/j.compositesb.2020.108336.

[101] Y. Huang, X. Gao, Y. Zhang, and B. Ma, "Laser joining technology of polymer-metal hybrid structures - A review," *J Manuf Process,* vol. 79, pp. 934-961, 2022, doi: 10.1016/j.jmapro.2022.05.026.

[102] Y. Y. Jang *et al.*, "Dissimilar material bonding technology for lightweight future mobility: A review," *Polymer Testing,* vol. 129, 2023, doi: 10.1016/j.polymertesting.2023.108281.

[103] Z. Liu, Y. Li, Z. Liu, Y. Yang, Y. Li, and Z. Luo, "Ultrasonic welding of metal to fiber-reinforced thermoplastic composites: A review," *J Manuf Process,* vol. 85, pp. 702-712, 2023, doi: 10.1016/j.jmapro.2022.12.001.

[104] K. Goto, K. Imai, M. Arai, and T. Ishikawa, "Shear and tensile joint strengths of carbon fiber-reinforced thermoplastics using ultrasonic welding," *Composites Part A: Applied Science and Manufacturing,* vol. 116, pp. 126-137, 2019, doi: 10.1016/j.compositesa.2018.10.032.

[105] H. Li, C. Chen, R. Yi, Y. Li, and J. Wu, "Ultrasonic welding of fiber-reinforced thermoplastic composites: a review," *The International Journal of Advanced Manufacturing Technology,* vol. 120, no. 1-2, pp. 29-57, 2022, doi: 10.1007/s00170-022-08753-9.

[106] T. G. Unnikrishnan and P. Kavan, "A review study in ultrasonic-welding of similar and dissimilar thermoplastic polymers and its composites," *Materials Today: Proceedings,* 2021, doi: 10.1016/j.matpr.2021.09.540.

[107] Y. Li, B. Yu, B. Wang, T. H. Lee, and M. Banu, "Online quality inspection of ultrasonic composite welding by combining artificial intelligence technologies with welding process signatures," *Mater Design,* vol. 194, 2020, doi: 10.1016/j.matdes.2020.108912.

[108] S. Krüger, G. Wagner, and D. Eifler, "Ultrasonic Welding of Metal/Composite Joints," *Adv Eng Mater,* vol. 6, no. 3, pp. 157-159, 2004, doi: 10.1002/adem.200300539.

[109] F. Staab, M. Liesegang, and F. Balle, "Local shear strength distribution of ultrasonically welded hybrid Aluminium to CFRP joints," *Composite Structures,* vol. 248, 2020, doi: 10.1016/j.compstruct.2020.112481.

[110] "An artificial neural network model for predicting joint performance in ultrasonic welding of composites," 2018.

[111] "Comprehensive Evaluation method of Bond Strength in Ultrasonic Welding for CFRTP."

[112] Z. Liu, Y. Li, W. Liu, H. Zhou, S. Ao, and Z. Luo, "Enhancing the ultrasonic plastic welding strength of Al/CFRTP joint via coated metal surface and structured composite surface," *J Manuf Process,* vol. 108, pp. 227-237, 2023, doi: 10.1016/j.jmapro.2023.11.001.

[113] Y. Yang, Y. Li, Z. Liu, Y. Li, S. Ao, and Z. Luo, "Ultrasonic welding of short carbon fiber reinforced PEEK with spherical surface anvils," *Composites Part B: Engineering,* vol. 231, 2022, doi: 10.1016/j.compositesb.2021.109599.

[114] T. Wang *et al.*, "Effect of ultrasonic embossing and welding time on the joint performance

of ultrasonically welded short carbon fiber reinforced PEEK," *Journal of Materials Research and Technology,* vol. 28, pp. 3258-3266, 2024, doi: 10.1016/j.jmrt.2023.12.266.

[115] Y. Guo *et al.*, "Parameter optimization of friction stir spot welded Al 6061 and CFRTP PA6 with surface treatment and interfacial adhesion," *Thin-Walled Structures,* vol. 197, 2024, doi: 10.1016/j.tws.2024.111585.

[116] P. Geng *et al.*, "Improving bonding strength of Al/CFRTP hybrid joint through modifying friction spot joining tools," *Composites Part B: Engineering,* vol. 254, 2023, doi: 10.1016/j.compositesb.2023.110588.

[117] L. H. Wu, K. Nagatsuka, and K. Nakata, "Direct joining of oxygen-free copper and carbon-fiber-reinforced plastic by friction lap joining," *Journal of Materials Science & Technology,* vol. 34, no. 1, pp. 192-197, 2018, doi: 10.1016/j.jmst.2017.10.019.

[118] L. H. Wu, K. Nagatsuka, and K. Nakata, "Achieving superior mechanical properties in friction lap joints of copper to carbon-fiber-reinforced plastic by tool offsetting," *Journal of Materials Science & Technology,* vol. 34, no. 9, pp. 1628-1637, 2018, doi: 10.1016/j.jmst.2018.04.015.

[119] F. Lionetto, F. Balle, and A. Maffezzoli, "Hybrid ultrasonic spot welding of aluminum to carbon fiber reinforced epoxy composites," *J Mater Process Tech,* vol. 247, pp. 289-295, 2017, doi: 10.1016/j.jmatprotec.2017.05.002.

[120] E. I. Avgoulas and M. P. F. Sutcliffe, "A Review of Natural Joint Systems and Numerical Investigation of Bio-Inspired GFRP-to-Steel Joints," *Materials (Basel),* vol. 9, no. 7, Jul 12 2016, doi: 10.3390/ma9070566.

[121] "A Circular Economy based Decision Support System for the AssemblyDisassembly of Multi-Material Components," 2019.

[122] K. NAKATA, "Dissimilar materials joining of CFRP and metal by friction lap joining process."

[123] N. M. André, S. M. Goushegir, J. F. dos Santos, L. B. Canto, and S. T. Amancio-Filho, "Influence of the interlayer film thickness on the mechanical performance of AA2024-T3/CF-PPS hybrid joints produced by friction spot joining," *Welding International,* vol. 32, no. 1, pp. 1-10, 2017, doi: 10.1080/09507116.2017.1347319.

[124] N. M. André, S. M. Goushegir, J. F. dos Santos, L. B. Canto, and S. T. Amancio-Filho, "Friction Spot Joining of aluminum alloy 2024-T3 and carbon-fiber-reinforced poly(phenylene sulfide) laminate with additional PPS film interlayer: Microstructure,

mechanical strength and failure mechanisms," *Composites Part B: Engineering,* vol. 94, pp. 197-208, 2016, doi: 10.1016/j.compositesb.2016.03.011.

[125] F. Lionetto, C. Mele, P. Leo, S. D'Ostuni, F. Balle, and A. Maffezzoli, "Ultrasonic spot welding of carbon fiber reinforced epoxy composites to aluminum: mechanical and electrochemical characterization," *Composites Part B: Engineering,* vol. 144, pp. 134-142, 2018, doi: 10.1016/j.compositesb.2018.02.026.

[126] R. Kalyan Kumar and M. Omkumar, "Ultrasonic welding of GF/PA6T composites: Experimental investigation and process optimization," *Materials Today: Proceedings,* vol. 39, pp. 1180-1186, 2021, doi: 10.1016/j.matpr.2020.03.462.

[127] K. Anitha *et al.*, "Advancing cancer theranostics through biomimetics: A comprehensive review," *Heliyon,* vol. 10, no. 6, p. e27692, Mar 30 2024, doi: 10.1016/j.heliyon.2024.e27692.

[128] J. Li, M. Li, J. J. Koh, J. Wang, and Z. Lyu, "3D-printed biomimetic structures for energy and environmental applications," *DeCarbon,* vol. 3, 2024, doi: 10.1016/j.decarb.2023.100026.

[129] Z. Zhang, G. Liu, Z. Li, W. Zhang, and Q. Meng, "Flexible tactile sensors with biomimetic microstructures: Mechanisms, fabrication, and applications," *Adv Colloid Interface Sci,* vol. 320, p. 102988, Oct 2023, doi: 10.1016/j.cis.2023.102988.

[130] T. Gutsmann, T. Hassenkam, J. A. Cutroni, and P. K. Hansma, "Sacrificial bonds in polymer brushes from rat tail tendon functioning as nanoscale velcro," *Biophys J,* vol. 89, no. 1, pp. 536-42, Jul 2005, doi: 10.1529/biophysj.104.056747.

[131] F. Yang and Z. Guo, "Characterization of Micro-Morphology and Wettability of Lotus Leaf, Waterlily Leaf and Biomimetic ZnO Surface," *Journal of Bionic Engineering,* vol. 12, no. 1, pp. 88-97, 2015, doi: 10.1016/s1672-6529(14)60103-7.

[132] P. Dagenais, S. Hensman, V. Haechler, and M. C. Milinkovitch, "Elephants evolved strategies reducing the biomechanical complexity of their trunk," *Curr Biol,* vol. 31, no. 21, pp. 4727-4737 e4, Nov 8 2021, doi: 10.1016/j.cub.2021.08.029.

[133] B. Chen, J. Fan, J. Gou, and S. Lin, "Hole-pin joining structure with fiber-round-hole distribution of lobster cuticle and biomimetic study," *J Mech Behav Biomed Mater,* vol. 40, pp. 161-167, Dec 2014, doi: 10.1016/j.jmbbm.2014.09.001.

[134] V. K. Thummalapalli and S. L. Donaldson, "Biomimetic composite structural T-joints," *Journal of Bionic Engineering,* vol. 9, no. 3, pp. 377-384, 2012, doi: 10.1016/s1672-

6529(11)60130-3.

[135] T. Steinbrecher, E. Danninger, D. Harder, T. Speck, O. Kraft, and R. Schwaiger, "Quantifying the attachment strength of climbing plants: a new approach," *Acta Biomater,* vol. 6, no. 4, pp. 1497-504, Apr 2010, doi: 10.1016/j.actbio.2009.10.003.

[136] K. Koch, B. Bhushan, and W. Barthlott, "Multifunctional surface structures of plants: An inspiration for biomimetics," *Progress in Materials Science,* vol. 54, no. 2, pp. 137-178, 2009, doi: 10.1016/j.pmatsci.2008.07.003.

[137] H. Pei, Y. Wu, W. Wu, L. Lyu, and W. Li, "A review of the types, functions and regulatory mechanisms of plant spines," *Plant Sci,* vol. 341, p. 112010, Apr 2024, doi: 10.1016/j.plantsci.2024.112010.

[138] Y. Zhang, Z. Wang, Y. Zhang, S. Gomes, and A. Bernard, "Bio-inspired generative design for support structure generation and optimization in Additive Manufacturing (AM)," *CIRP Annals,* vol. 69, no. 1, pp. 117-120, 2020, doi: 10.1016/j.cirp.2020.04.091.

[139] Z. Jiang, Y. Ma, and Y. Xiong, "Bio-inspired generative design for engineering products: A case study for flapping wing shape exploration," *Advanced Engineering Informatics,* vol. 58, 2023, doi: 10.1016/j.aei.2023.102240.

[140] L. A. Burns, A. P. Mouritz, D. Pook, and S. Feih, "Bio-inspired design of aerospace composite joints for improved damage tolerance," *Composite Structures,* vol. 94, no. 3, pp. 995-1004, 2012, doi: 10.1016/j.compstruct.2011.11.005.

[141] E. I. Avgoulas and M. P. F. Sutcliffe, "Biomimetic-inspired CFRP to perforated steel joints," *Composite Structures,* vol. 152, pp. 929-938, 2016, doi: 10.1016/j.compstruct.2016.06.014.

[142] F. Gallenmuller, A. Feus, K. Fiedler, and T. Speck, "Rose Prickles and Asparagus Spines--Different Hook Structures as Attachment Devices in Climbing Plants," *PLoS One,* vol. 10, no. 12, p. e0143850, 2015, doi: 10.1371/journal.pone.0143850.

[143] T. Wang, K. Yasuda, and H. Nishikawa, "Study on the SPCC and CFRTP Hybrid Joint Performance Produced with Additional Nylon-6 Interlayer by Ultrasonic Plastic Welding," *Polymers (Basel),* vol. 14, no. 23, Dec 1 2022, doi: 10.3390/polym14235235.

[144] O. Sorgonà, N. P. Belfiore, O. Giannini, and M. Verotti, "Application of the ellipse of elasticity theory to the functional analysis of planar compliant mechanisms," *Mechanism and Machine Theory,* vol. 184, 2023, doi: 10.1016/j.mechmachtheory.2023.105308.

[145] M. E. Korkmaz, M. K. Gupta, G. Robak, K. Moj, G. M. Krolczyk, and M. Kuntoğlu, "Development of lattice structure with selective laser melting process: A state of the art on

properties, future trends and challenges," *J Manuf Process,* vol. 81, pp. 1040-1063, 2022, doi: 10.1016/j.jmapro.2022.07.051.

[146] R. Nandhakumar and K. Venkatesan, "A process parameters review on selective laser melting-based additive manufacturing of single and multi-material: Microstructure, physical properties, tribological, and surface roughness," *Materials Today Communications,* vol. 35, 2023, doi: 10.1016/j.mtcomm.2023.105538.

[147] M. A. Wagner *et al.*, "Filament extrusion-based additive manufacturing of 316L stainless steel: Effects of sintering conditions on the microstructure and mechanical properties," *Addit Manuf,* vol. 59, 2022, doi: 10.1016/j.addma.2022.103147.

[148] "Fabrication and characterization of 316L stainless steel components printed with material extrusion additive manufacturing."

[149] N. K. Bankapalli, V. Gupta, P. Saxena, A. Bajpai, C. Lahoda, and J. Polte, "Filament fabrication and subsequent additive manufacturing, debinding, and sintering for extrusion-based metal additive manufacturing and their applications: A review," *Composites Part B: Engineering,* vol. 264, 2023, doi: 10.1016/j.compositesb.2023.110915.

[150] Y. Thompson, J. Gonzalez-Gutierrez, C. Kukla, and P. Felfer, "Fused filament fabrication, debinding and sintering as a low cost additive manufacturing method of 316L stainless steel," *Addit Manuf,* vol. 30, 2019, doi: 10.1016/j.addma.2019.100861.

[151] J. Jansa *et al.*, "Corrosion and material properties of 316L stainless steel produced by material extrusion technology," *J Manuf Process,* vol. 88, pp. 232-245, 2023, doi: 10.1016/j.jmapro.2023.01.035.

[152] F. Wang, S. You, D. Jiang, and F. Ning, "Study on sintering mechanism for extrusion-based additive manufacturing of stainless steel through molecular dynamics simulation," *Addit Manuf,* vol. 58, 2022, doi: 10.1016/j.addma.2022.102991.

[153] M. A. Wagner *et al.*, "Fused filament fabrication of stainless steel structures - from binder development to sintered properties," *Addit Manuf,* vol. 49, 2022, doi: 10.1016/j.addma.2021.102472.

[154] A. Páez-Pavón, A. Jiménez-Morales, T. G. Santos, L. Quintino, and J. M. Torralba, "Influence of thermal debinding on the final properties of Fe–Si soft magnetic alloys for metal injection molding (MIM)," *Journal of Magnetism and Magnetic Materials,* vol. 416, pp. 342-347, 2016, doi: 10.1016/j.jmmm.2016.05.031.

[155] F. Wang, S. You, D. Jiang, X. Yuan, R. Fu, and F. Ning, "Microstructure evolution, phase

formation, corrosion, and mechanical properties of stainless steel fabricated by extrusion-based sintering-assisted additive manufacturing," *Addit Manuf,* vol. 75, 2023, doi: 10.1016/j.addma.2023.103746.

[156] A. Kasha, K. V. Srinivasan, S. O. Obadimu, and K. I. Kourousis, "Immersion corrosion of material extrusion steel 316 L: Influence of immersion time and surface roughness," *Materials Today Communications,* vol. 35, 2023, doi: 10.1016/j.mtcomm.2023.106394.

[157] "Mechanical behavior of Material Extrusion Additive Manufactured components-an overview

".

[158] Q. Zou *et al.*, "Effects of laser hybrid interfacial pretreatment on enhancing the carbon fiber reinforced thermosetting composites and TC4 alloy heterogeneous joint," *Materials Today Communications,* vol. 30, 2022, doi: 10.1016/j.mtcomm.2022.103142.

[159] F. Wilhelm, S. Strauß, and M. Kronseder, "Effect of power ultrasonic on the viscosity of anhydride epoxy resin system," *Results in Materials,* vol. 8, 2020, doi: 10.1016/j.rinma.2020.100129.

[160] L. Li *et al.*, "Effect of heat input on characteristics of TC4-CFRTP laser welding joints with PA6/epoxy resin interlayer," *Optics & Laser Technology,* vol. 174, 2024, doi: 10.1016/j.optlastec.2024.110560.

[161] K. Osakada and M. Shiomi, "Flexible manufacturing of metallic products by selective laser melting of powder," *International Journal of Machine Tools and Manufacture,* vol. 46, no. 11, pp. 1188-1193, 2006, doi: 10.1016/j.ijmachtools.2006.01.024.

[162] M. Badrossamay and T. H. C. Childs, "Further studies in selective laser melting of stainless and tool steel powders," *International Journal of Machine Tools and Manufacture,* vol. 47, no. 5, pp. 779-784, 2007, doi: 10.1016/j.ijmachtools.2006.09.013.